Models of Cerebral Blood Flow and their Evidence in Data

Chris Zheng

Submitted in total fulfilment of the requirements
of the degree of Master of Philosophy

August 2011

Department of Electrical Engineering

The University of Melbourne

Dedicated to everyone who has made this happen. Thank you.

Abstract

Arterial Spin Labelling (ASL) provides a direct measurement of Cerebral Blood Flow (CBF) and is known to correlate with changes in neuronal activation during fMRI paradigms. While the Blood-Oxygenated Level Dependent (BOLD) signal also correlates with neuronal activation, it results from indirect measurement of unobserved physiological variables. In this thesis, mathematical models of CBF were constructed to be profiled within a simulation framework and then used in the analysis of an experimental ASL dataset. The validity of each model was scrutinized through a model comparison framework. The findings of the thesis show that although higher-order models of CBF can be constructed, they may not offer any greater insight into ASL-fMRI data than a simple model and in fact, may be less accurate. It is concluded that the proposed model testing framework provides a useful first pass of data to establish the level of complexity used to model fMRI data. As signal acquisition methods improve, the models of fMRI signal change to hemodynamic responses will thus become verifiable and become a practical means of signal estimation. Until that time, complex multiparameter models of brain physiology during fMRI experimentation may be proposed, but as this thesis demonstrates, such models will be extremely difficult to verify experimentally.

Declaration

This is to certify that:

1. This thesis comprises only my original work towards the Masters of Research except where indicated in the Preface

2. Due acknowledgement has been made in the text to all other material used.

3. This thesis is less than 50,000 words in length, inclusive of footnotes, but exclusive of tables, maps, bibliographies and appendices of the thesis is 25,890 as approved by the Graduate School, Faculty or RHD Committee

Haohang (Chris) Zheng

Preface

Work contributed by others is duly acknowledged below:

- My supervisor, Dr Leigh Johnston contributed in the formation of the original idea for modelling of CBF data as well as being present through all aspects of planning, algorithmic design, experimental design, analysis of data and preparation of this thesis through much welcomed critique and correction.

- My supervisor, Professor Gary Egan for his guidance in setting major milestones and much needed critique of my delivary in both paper and presentation forms.

- My supervisor, Dr Maria Gavrilescu for her guidance and patience in understanding the intricacies of BOLD-fMRI and ASL-fMRI signal analysis and assisted in the first pass of the data

- Dr Michael Farrell and Dr Leonie Cole for supplying the ASL-fMRI data that was analysed as well as for their advice regarding data analysis methods and areas of the brain to focus upon.

Acknowledgements

I thank my supervisors Gary, Maria and especially Leigh for giving me this opportunity without any prior experience of neuroscience research on my part, for having patience with me whilst I became stuck on what to do next on many occasions, and lastly for your feedback and guidance throughout my thesis. I thank Leonie and Michael for providing me with the CBF data for analysis as well as giving me valuable advice about my thesis and the analysis. I thank my father Jeffrey for his encouragement and support. Talking to him at critical times inspired much creativity that allowed me to gain a broader perspective on my work. I thank my girlfriend Xing for her emotional strength as well as her unwavering faith in me. I thank our pets Marco and Madeline for making this incredibly long and enduring process so much fun. I thank John and Miriam for their support and guidance. I thank all the friends and acquaintances I have meet along the way who had made this incredible journey the incredible experience that it has been. Finally, I thank his holiness, Srila A.C. Bhaktivendanta Prabhupada for giving me the knowledge to do what was needed when I myself had already given up.

Contents

List of Symbols

Signals and Definitions	
NMR Signals	
$\mathbf{B}(t)$	External Magnetic Field
B_0	Static External Magnetic Field parallel to the z-axis
$\mathbf{M}(t)$	Bulk Magnetisation Vector
M_0	Equilibrium Bulk Magnetisation
fMRI Input Signals	
$u(t)$	Stimulus Input
$\eta(t)$	Neuronal Activity
$i(t)$	Inhibitory Input
BOLD Signal	
$b(t)$	BOLD Signal
b_0	Baseline BOLD Value
$b^{(i)}(t)$	BOLD Signal within Capillary
$b_0^{(i)}$	Baseline BOLD Signal within Capillary
$b^{(e)}(t)$	BOLD Signal outside of Capillary
$b_0^{(e)}$	Baseline BOLD Signal outside of Capillary
$b_0^{(h)}$	Baseline BOLD Signal of Homogeneous Tissue
$\Delta b_n(t)$	BOLD Signal Change (Normalized), $\Delta b_n(t) = \frac{b(t)-b_0}{b_0}$
CBV Response	
$v(t)$	CBV Response
v_0	Baseline CBV Response
$v_n(t)$	CBV Response (Normalized), $v_n(t) = \frac{v(t)}{v_0}$
$\lambda(t)$	Fractional Volume Partition - Baseline
λ_0	Baseline Fractional Volume Partition

Signals and Definitions Continued	
Oxygenation Response	
$q(t)$	Deoxyhemoglobin Content
q_0	Baseline Deoxyhemoglobin Content
$q_n(t)$	Deoxyhemoglobin Content (Normalized), $q_n(t) = \frac{q(t)}{q_0}$
$c(t)$	$CMRO_2$ Response
c_0	$CMRO_2$ Response
$c_n(t)$	$CMRO_2$ Response (Normalized)
c_{max}	Maximum $CMRO_2$ Response (Normalized)
$\rho(t)$	Fractional Oxygenation
$E(t)$	Oxygen Extraction Fraction, $E(t) = 1 - \rho(t)$
E_0	Baseline Oxygen Extraction Fraction
CBF Response	
$f(t)$	CBF Response
f_0	Baseline CBF Response
$f_n(t)$	CBF Response (Normalized), $f_n(t) = \frac{f(t)}{f_0}$
$f_n(t)$	Measured CBF Response (Normalized)
f_{max}	Maximum CBF Response (Normalized)

Parameters and Definitions	
NMR Model of BOLD	
T_1	Time Constant of Relaxation (Spin-Lattice),
T_2	Time Constant of Relaxation (Spin-Spin), $R_2 = \frac{1}{T_2}$
T_2'	Time Constant of Relaxation (Field Inhomogeneity)
T_2^D	Time Constant of Relaxation (Diffusion)
T_2^*	Time Constant of Relaxation (Observable)
R_1	Inverse of T_1,$R_1 = \frac{1}{T_1}$
R_2	Inverse of T_2, $R_2 = \frac{1}{T_2}$
R_2^*	Inverse of T_2^*, $R_2^* = \frac{1}{T_2^*}$
$R_2^{(Hb)}$	Additional Relaxation Rate due to Deoxyhemoglobin
$R_2^{(i)}$	Relaxation Rate within Capillary
$\Delta R_2^{(i)}$	Change in Relaxation Rate within Capillary
$R_2^{(e)}$	Relaxation Rate outside of Capillary
$\Delta R_2^{(e)}$	Change in Relaxation Rate outside of Capillary
γ	Gyro-Magnetic Ratio
$\zeta(t)$	Frequency Offset from Difference in Magnetic Susceptibility
ζ_0	Frequency Offset for Homogeneous Tissue
μ	Base Attenuation Factor
μ_0	Additional Attenuation Factor from Deoxyhemoglobin
$\mu^{(i)}$	Attenuation Factor within the capillary
$\mu^{(e)}$	Attenuation Factor outside the capillary
$CMRO_2$ Ratio	
$n(t)$	Normalized CBF Increase Compared to Normalized $CMRO_2$ Increase
n_{av}	Average measurement of $n(t)$
M	Coefficient of Signal for Hypercapnia Model
α	Power Relationship for Increase in CBF to Increase in CBV
β	Influence of 2% Deoxyhemoglobin Content on Magnetic Susceptibility
Balloon Model	
κ_i	Gain Factor of Inhibition
τ_i	Time Constant of Inhibition
$h(t)$	Gamma Function for Convolution with $\eta(t)$
CBF Model Parameters	
τ_f	Time Constant for Signal Feedback
τ_s	Time Constant for Signal Decay
ϵ_1, ϵ_4	Efficacy of Differential Stimulus Response
ϵ_2	Efficacy of Proportional Stimulus Response
ϵ_3	Efficacy of Integral Stimulus Response

List of Figures

List of Tables

Chapter 1

Introduction to fMRI

When we use our brains to think or initiate an action, an entire cascade of events occur. These events span biochemical interactions within the neuron, cell-to-cell interactions, physiological responses in the local brain tissue, networked cortical activation across the brain. Over the centuries, the lack of a tool that allowed one to look into the mind at work had limited neuroscience to either diagnosis through cognitive behaviour, investigation into physical debilitation (for example, lesions due to stroke and metastasis) or experimentation through anatomical dissection and lobotomies. Development of semi-invasive and non-invasive neuroimaging techniques such as position emission tomography (PET), electroencephalography (EEG), magnetoencephalography (MEG), functional near infrared imaging (fNIRS), and functional magnetic resonance imaging (fMRI) has allowed us to bridge the gap between the laboratory bench and the psychologist's couch and to observe the whole brain at work.

Bandettini (2007) describes fMRI as "being comprised of four interacting, co-evolving parts: hardware, methodology, signal interpretability and applications, each driving and feeding off the advances of the others" (Figure 1.1). This statement summarizes the dynamic and evolving nature of fMRI research; although it is a multidisciplinary field of science, techniques in fMRI are so interwoven that an advance in one part is likely to influence the direction of new research in other parts. FMRI has advantages over other forms of functional imaging such as EEG and PET due to its ability to measure multiple effects (Ogawa and Lee, 1990; Wong et al., 1997; Lu et al., 2003) and also provides the best combined spatial and temporal resolution over the entire brain (Toga and Mazziotta, 2002). However, there are definite limitations as to what can be done with fMRI. As Logothetis (2008) emphatically states, "fMRI is not and will never be a mind reader", he highlights the difficulties of obtaining accurate activation measurements using such a technique. Trade offs between spatial and temporal resolution at both local and global scales provide a soft ceiling for how far the technology can be pushed.

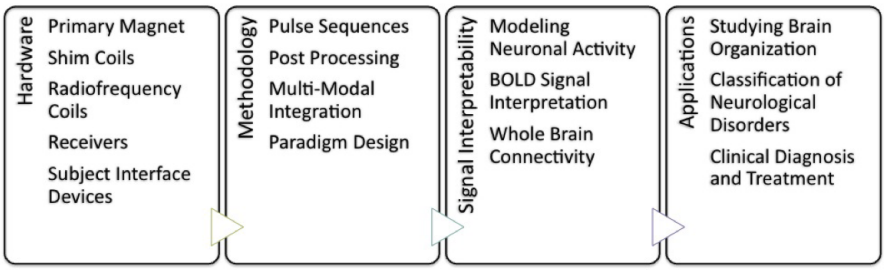

Figure 1.1: The four components of fMRI [according to Bandettini (2007)].

Nevertheless, despite its limits fMRI has played an unprecedented role in developing and expanding neuroscience.

FMRI like all neuroimaging techniques is grounded in physiology. As such, many MRI sequences for functional signal measurement have been developed to complement the earliest fMRI signal, the blood-oxygenation level dependent (BOLD) signal found by Ogawa and Lee (1990). Physiological signals that now can be measured include cerebral blood flow (CBF) using arterial spin labelling (ASL-fMRI) (Wong et al., 1997; Jahng et al., 2007), cerebral blood volume (CBV) using vascular space occupancy (VASO-fMRI) (Lu et al., 2003) and venous refocusing for volume estimation (VERVE-fMRI) (Stefanovic and Pike, 2005). Additionally, the BOLD-fMRI signal has been integrated with non-fMRI methods of signal acquisition such as micro-electrode measurements (Goense and Logothetis, 2008; Logothetis et al., 2001; Oeltermann et al., 2007) and EEG (Vulliemoz et al., 2009; Christmann et al., 2007). The micro-electrode experiments have allowed fMRI signals to be correlated with invasive studies that provide higher spatial and temporal resolution of brain physiology.

As more and more fMRI signals are developed and improved, theoretical models of physiology describing the biophysical origins of such signals enable better interpretation of information. Most of the modelling has concentrated on investigation into the BOLD-fMRI signal, as it is the earliest and most studied. Other fMRI sequences have not received the same amount of attention in theoretical modelling and most researchers have only used other sequences to add additional information to the BOLD-fMRI model such as the measurement of ASL-fMRI signal alongside the BOLD-fMRI signal for estimation of the cerebral metabolic rate of oxygen ($CMRO_2$) by Davis et al. (1998). However the ASL-fMRI signal may be analysed independently and is a closer representation of

physiology than the BOLD-fMRI signal.

The key question that arises is whether ASL-fMRI data can be modelled better than the existing methods through inclusion of physiologically grounded parameters. The thesis aims to investigate this question by providing a framework for model comparison and then using this framework to evaluate the effectiveness of current and proposed models of CBF data collected using ASL-fMRI. Chapter 2 gives an overview of the history of fMRI modelling, focusing on BOLD-fMRI and ASL-fMRI modelling. Chapter 3 outlines proposed ASL-fMRI models as well as mathematical tools and analysis frameworks that are used for model estimation and selection. Chapter 4 provides simulations using the modelling framework and tests for the sensitivity of various CBF models to noise, sampling time and other factors. Chapter 5 uses a subset of models determined to be robust enough for analysis to ascertain the best model for use in analysis of experimental CBF data.

Chapter 2

Modelling of fMRI Signals

In reading any work regarding fMRI signal modelling, it is useful to keep in mind that all fMRI signals have their origins in neuronal activation. The challenge motivating current research is to find the most direct correlate to neuronal activation using an array of fMRI techniques. The last section of this chapter presents evidence to support the hypothesis governing this thesis: that direct modelling ASL-fMRI data may offer a better estimate of neuronal activation than the current methods. However, understanding how this hypothesis was reached requires an understanding of BOLD-fMRI modelling signal and the research leading up to the work done during this thesis. This chapter primarily describes how fMRI signals came to be measured as well as how they have been interpreted through biophysical modelling. ASL-fMRI, BOLD-fMRI and other theoretical frameworks for modelling fMRI signal behaviour are introduced: first from a biophysical viewpoint of how the signal is obtained, and then from a hemodynamic viewpoint of how the signals interact with each other. Finally, experimental work is presented in order to support the hypothesis outlined earlier thus giving the motivation for conducting research in this area.

2.1 Biophysics of Functional Imaging

Italian scientist Angelo Mosso first described an alteration of regional brain circulation as a response to a mental activity (Mosso, 1884). This phenomena has been repeated in countless experiments using PET, fMRI and other techniques (Raichle, 1998). FMRI measurement depends on hemodynamic changes affecting the local magnetic susceptibility of an activated region of the brain. The two main changes are: substrate delivery (blood flow) and substrate consumption (metabolism). These changes play a key role in modulating signals observed using fMRI. Understanding the underlying mechanisms driving these physiological changes therefore becomes paramount. Consequently, re-

search has progressed from asking qualitative questions – "what is changing?" to asking quantitative questions – "how is it changing?". Much experimental evidence has been accumulated and used to propose theoretical models of brain oxygenation. Ultimately, all of the questions asked converge on the one goal: providing accurate measurement and modelling of brain behaviour in order to produce measured fMRI signal from stimulated neuronal activity.

It was the early work of Roy and Sherrington (1890) and their observations of neuro-vascular changes in various animal models under the effects of mechanical and electrical stimulation and drugs that formed an understanding of the neuro-vascular coupling mechanism. Three experiments gave remarkable insights into the dependence of brain volume on brain chemistry. The experiments recorded cerebral blood volume, arterial pressure and venous pressure in the brain whilst the animals were exposed to an assortment of exogenous conditions designed to provoke changes in brain physiology. The first experiment observed effects after various acids were introduced into the blood stream of a dog. The second experiment observed effects after controlled asphyxiation was induced in a dog. The third experiment observed effects in a dog after injection of tissue extracts from the oxygen deprived brain of another dog. All three induced rapid increases in the observed blood volume while not affecting blood pressure. These effects resulted in a hypothesis that the hemodynamic response induced by neuronal activity was chemically activated due to requirements of increased local metabolism. Roy and Sherrington (1890) concluded that,

> "The chemical products of cerebral metabolism...can cause variations of the calibre of the cerebral vessels. In this reaction the brain possesses an intrinsic mechanism by which its vascular supply can be varied locally in correspondence with local variations of functional activity."

After over a century of experimentation and technological advancement, the scientific community has expanded upon the principle hypothesis of Roy and Sherrington (1890). The idea that substrate delivery by blood flow increased due to the increased metabolic requirements of the signalling neuron has been proven to be oversimplified and inaccurate. The current body of research has undergone a conceptual shift in the modelling and understanding of the neuronal activation response (Attwell and Iadecola, 2002). It is now believed that mechanisms for regulation of blood flow and metabolism have quite separate mechanisms of activation. The contribution of all hemodynamic mechanisms to the final observed signal using fMRI is paramount in the understanding of brain dynamics. FMRI research has responded by using mathematical modelling to infer processes governing

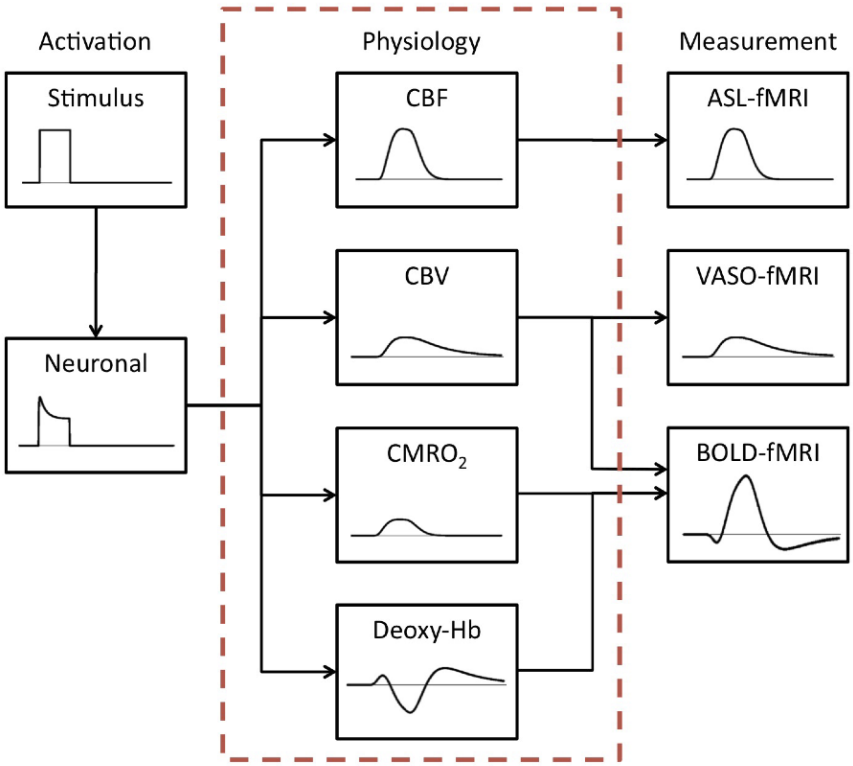

Figure 2.1: Hemodynamic processes involved in activation [adapted from Buxton et al. (2004)].

physiological dynamics of the brain. Figure 2.1 depicts the physiological effects that contribute to measurement of fMRI signals.

The two observed signals used most extensively in fMRI research are the BOLD-fMRI signal and the calibrated-BOLD signal, equivalent to the estimated $CMRO_2$ response. With multi-signal acquisition capabilities, physiological signals can be measured including ASL-fMRI (Wong et al., 1997; Jahng et al., 2007), VASO-fMRI (Lu et al., 2003), VERVE-fMRI (Stefanovic and Pike, 2005) as well as the more contentious neuronal current (Chen-Bee et al., 2007; Kraus et al., 2008). Understanding how the brain operates requires many levels of conceptual modelling that interface with all associated functions of the brain, for instance: the psychology; the anatomy; the physiology; and the biochemistry. Therefore, equipment and methods that can clearly identify physiological changes on all such levels are very important to understanding how the brain operates. The next section details how the physiological components are observed whilst Section 2.3 examines individual dynamics of components seen in Figure 2.1.

2.2 Observations of Biophysical Signals

This section examines the biophysical basis of MRI signals (Section 2.2.1), how they are used in the models and presents the mathematical derivations of ASL-fMRI (Section 2.2.2) and BOLD-fMRI (Section 2.2.3) signals.

2.2.1 MRI Basics and the Theory of NMR

Nuclear magnetic resonance (NMR) was discovered in 1946 by two independent research groups, one led by Edward Purcell and the other by Felix Bloch. The two leading researchers' work in radar during World War II and their subsequent development of radiofrequency techniques allowed them to apply the same techniques to investigate nuclear magnetism (Purcell et al., 1946; Bloch et al., 1946). The NMR effect is found in atoms with odd numbered nuclei that therefore possess a nuclear magnetic moment, causing them to precess around the axis of an externally directed magnetic field (B_0) at a frequency (ω_0) proportional to the strength of the magnetic field. This frequency is known as the Larmor frequency, named after Joseph Larmor, an Irish mathematician who first explained a similar electromagnetic effect for electrons (Larmor, 1896). The Larmor equation of nuclear magnetic resonance is:

$$\omega_0 = \gamma B_0 \tag{2.1}$$

The gyro-magnetic constant, γ, is unique for every atomic nuclei. Purcell and Bloch conducted experiments that looked at two different aspects of the same phenomenon. Purcell et al. (1946) showed that energy was absorbed by a homogeneous material when an electromagnetic stimulus was applied at the Larmor frequency, whilst Bloch et al. (1946) showed that oscillations produced by applying an external magnetic field could in fact be measured using a coiled solenoid. These experiments demonstrated that magnetic properties of materials were able to be quantitatively measured with high precision.

Magnetic Resonance Imaging takes advantage of the resonance property of hydrogen nuclei in the body – abundantly found in the body allowing for a strong detectable signal. γ of hydrogen is 42.58 MHz/T. This is used to tune the resonant frequency for hydrogen nuclei. MRI measures the NMR signals arising from the interactions between the tissue and an external magnetic field after electromagnetic stimulation. Lauterbur (1973) first demonstrated the principles of MRI, applying additional encoding gradients to localize space in a systematic manner such that a 2D or 3D reconstruction of an object could be obtained efficiently.

The Bloch Equation Tissues within the body can be differentiated through behaviour of their bulk magnetisation under excitation, done using MRI. This phenomena is modelled using the Bloch equation - a set of differential equations proposed by Bloch based upon empirical observation describing the dynamics of $\mathbf{M}(t)$ within an external magnetic field $\mathbf{B}(t)$:

$$\frac{d\mathbf{M}(t)}{dt} = \mathbf{M}(t) \times \gamma\mathbf{B}(t) - \mathbf{R}\left(\mathbf{M}(t) - \begin{bmatrix} 0 \\ 0 \\ M_0 \end{bmatrix}\right) \text{ where } \mathbf{M}(t) = \begin{bmatrix} M_x(t) \\ M_y(t) \\ M_z(t) \end{bmatrix} \tag{2.2}$$

$$\mathbf{R} = \begin{bmatrix} \frac{1}{T_2} & 0 & 0 \\ 0 & \frac{1}{T_2} & 0 \\ 0 & 0 & \frac{1}{T_1} \end{bmatrix} \tag{2.3}$$

$\mathbf{R}$ is known as the 'relaxation matrix' and is related to how quickly each component of $\mathbf{M}(t)$ returns to the equilibrium state. Equation (2.2) can be separated into its axial components:

$$\begin{aligned} \frac{dM_x(t)}{dt} &= \gamma[M_y(t)B_z(t) - M_z(t)B_y(t)] - \frac{M_x(t)}{T_2} \\ \frac{dM_y(t)}{dt} &= \gamma[M_z(t)B_x(t) - M_x(t)B_z(t)] - \frac{M_y(t)}{T_2} \\ \frac{dM_z(t)}{dt} &= \gamma[M_x(t)B_y(t) - M_y(t)B_x(t)] - \frac{M_z(t) - M_0}{T_1} \end{aligned} \tag{2.4}$$

The two constants T_1 and T_2 describe relaxation rates. T_1 and T_2 are only applicable to tissues (bulk nuclei) and describes a group relaxation effect. T_1 arises from spin-lattice interactions and measures the half-life of longitudinal recovery due to energy transfer between nuclei and the homogeneous lattice. T_2 arises from spin-spin interactions and measures the half-life of transverse decay. Different tissues have different values of T_1 and T_2 which are utilized by MRI to provide contrast.

2.2.2 Observed Model of the ASL-fMRI Signal

Perfusion imaging or measurement of whole brain CBF was first achieved using positron emission tomography (PET) through an injection of a radioactive tracer into the bloodstream (Phelps et al., 1975; Ter-Pogossian et al., 1975). A technique for perfusion measurement was developed for MRI known as Arterial Spin Labelling or ASL-fMRI, the advantage being that CBF images could be obtained without the need for an extrogenous

contrast agent (Detre et al., 1992; Dixon et al., 1986; Williams et al., 1992). ASL uses an endogenous tracer created through magnetically 'tagging' or exciting arterial blood just below the head; the tagged blood can then be imaged as blood flows into the brain.

Modelling the ASL-fMRI signal requires modification of the Bloch Equations (2.4) so that the model includes magnetization effects in the presence of flow of blood into and out of the voxel. The theory presented is based on derivations by Williams et al. (1992) and Alsop and Detre (1996). In their model, only the z-component of Equation (2.4) is considered because the inverting magnetic pulse is applied in the z-direction. Assuming contributions from $B_x(t)$ and $B_y(t)$ are zero and assuming that there is a flow of blood $f(t)$ into the brain with magnetization $M_a(t)$, the z-component seen in Equation (2.4) with inclusion of flow can be rewritten as:

$$\frac{dM_z(t)}{dt} = -\frac{M_z(t) - M_0}{T_1} + f(t)M_a(t) - \lambda(t)f(t)M_z(t) \tag{2.5}$$

The first additional component, $f(t)M_a(t)$, represents the magnetisation of the water entering the brain. The theory then assumes that the spins are continuously inverted such that the magnetisation is constant ($M_a(t) = -M_{a0}$). The other additional component, $f(t)\lambda(t)M_z(t)$, is the magnetisation of the water leaving the brain. $\lambda(t)$ is the fractional volume partition of the ratio between the total water content per volume of blood compared to the total water content per volume of brain tissue. In the model, $\lambda(t)$ is assumed to be a constant ($\lambda(t) = \lambda_0$). Note that in most formulations of ASL citing Alsop and Detre (1996), Wang et al. (2002) and Williams et al. (1992), the convention is to define another fractional volume partition where they use the inverse of the current definition, i.e. $\lambda = \frac{1}{\lambda_0}$. Using the current definition of λ_0 results in more tractable mathematics and is used throughout.

Continuous CBF Steady-State Model The the simplest model of CBF measurement using ASL-fMRI assumes that the magnetisation is continuously applied to the arterial blood flowing into the head. The blood is assumed to be a constant $f(t) = f^{(m)}$. Furthermore, it is also assumed by the ASL-fMRI model that under fully relaxed conditions for the water in both the brain and blood flowing into the brain, the in-flowing magnetization is equal to the out-flowing magnetization:

$$f(t)M_a(t) = f^{(m)}M_{a0} = \lambda_0 f^{(m)}M_0 \tag{2.6}$$

$\lambda_0 f^{(m)}M_0$ is substituted for $f(t)M_a(t)$ in Equation (2.5) and the solution of the differ-

ential equation is:

$$M_z(t) = \frac{M_0}{1+\lambda_0 f^{(m)} T_1}\left[(1-\lambda_0 f^{(m)} T_1) + 2\lambda_0 f^{(m)} T_1 e^{-t(1/T_1+\lambda_0 f^{(m)})}\right] \tag{2.7}$$

It can be seen that for continuous inversion of arterial spins results in an exponential decrease in $M_z(t)$ with time constant T_{1A} where:

$$\frac{1}{T_{1A}} = \frac{1}{T_1} + \lambda_0 f^{(m)} \tag{2.8}$$

Assuming that the change in blood flow $f^{(m)}$ over time remains too small to significantly affect the value of T_{1A}, the steady state magnetisation, $M_z^{(ss)} = M_z(t=\infty)$ can be determined to be:

$$M_z^{(ss)} = M_z(t=\infty) = M_0 \frac{1-\lambda_0 f^{(m)} T_1}{1+\lambda_0 f^{(m)} T_1} \tag{2.9}$$

Equation (2.8) can be rearranged with T_1 as the subject:

$$T_1 = \frac{T_{1A}}{1-\lambda_0 f^{(m)} T_{1A}} \tag{2.10}$$

The expression for T_1 is substituted into Equation (2.9):

$$M_z^{(ss)} = M_0 \frac{1-\frac{\lambda_0 f^{(m)} T_{1A}}{1-\lambda_0 f^{(m)} T_{1A}}}{1+\frac{\lambda_0 f^{(m)} T_{1A}}{1-\lambda_0 f^{(m)} T_{1A}}} \tag{2.11}$$

Let $\chi = \lambda_0 f^{(m)} T_{1A}$:

$$\begin{aligned} M_z^{(ss)} &= M_0 \frac{1-\frac{\chi}{1-\chi}}{1+\frac{\chi}{1-\chi}} \\ &= M_0 \frac{1-\chi-\chi}{1-\chi+\chi} = M_0(1-2\chi) \\ &= M_0(1-2\lambda_0 f^{(m)} T_{1A}) \end{aligned} \tag{2.12}$$

So the flow $f^{(m)}$ can be determined by making it the subject:

$$f^{(m)} = \frac{1}{2\lambda_0 T_{1A}}\left(1 - \frac{M_z^{(ss)}}{M_0}\right) \tag{2.13}$$

Since T_{1A}, M_0, $M_z^{(ss)}$ are all measurable quantities of MRI, $f^{(m)}$ can be determined using Equation (2.13).

Continuous CBF Model for Varying TR The equations of the behaviour of steady-state model can be extended for discretely sampled CBF images in time. The most common method is for the continuous inversion of spins during the recovery period (TR) in a conventional imaging sequence. Two images are obtained - a control image, $M_z^{(ctr)}(t = TR)$, and an inverted image, $M_z^{(inv)}(t = TR)$, that has its spin inverted with respect to the control. By solving the equations, the flow $f^{(m)}$ can be obtained. The following derivation belongs to Williams et al. (1992). The model assumes that arterial spins for detection are replenished with inverted spins much quicker than recovery time so $M_a(t) = -M_{a0}$ (just like the previous model). Equation (2.5) is solved for a slice selection pulse with tip angle ϕ and $t = TR$. When the inversion pulse is on during the TR period, the intensity $M_z^{(inv)}(t = TR)$ can be written as:

$$M_z^{(inv)}(t = TR) = M_0 \frac{1 - \lambda_0 f^{(m)} T_1}{1 + \lambda_0 f^{(m)} T_1} \frac{1 - e^{-(1/T_1 + \lambda_0 f^{(m)})TR}}{1 - \cos(\phi) e^{-(1/T_1 + \lambda_0 f^{(m)})TR}} \tag{2.14}$$

The control image $M_z^{(ctr)}(t = TR)$ can be written as:

$$M_z^{(ctr)}(t = TR) = M_0 \frac{1 - e^{-(1/T_1 + \lambda_0 f^{(m)})TR}}{1 - \cos(\phi) e^{-(1/T_1 + \lambda_0 f^{(m)})TR}} \tag{2.15}$$

Similarly to Equation (2.13), the two equations can be solved by substituting Equation (2.8) into both and then rearranging for $f^{(m)}$ as the subject:

$$f^{(m)} = \frac{1}{2\lambda_0 T_{1A}} \left(1 - \frac{M_z^{(inv)}(TR)}{M_z^{(ctr)}(TR)} \right) \tag{2.16}$$

The CBF value, $f^{(m)}$, can then be found using the two images. With fMRI imaging, alternate control and inverted images are sampled and a discretely sampled time series of $f^{(m)}$ values can be generated.

2.2.3 Observed Model of the BOLD-fMRI Signal

Being the earliest detected signal for functional imaging studies (Ogawa et al., 1990), the BOLD-fMRI signal has been widely used for functional magnetic resonance imaging. It takes advantage of the fact that the T_2 decay is faster than the T_1 recovery. The theoretical T_2 signal is obscured by two additional effects – field inhomogeneity, T_2', and diffusion, T_2^D. Effects of field inhomogeneity occur at the atomic level. Diffusion effects are significant in cavities and vessels where water is free to diffuse. The addition of these

two terms serves to shorten the decay time, termed T_2^*:

$$\frac{1}{T_2^*} = \frac{1}{T_2} + \frac{1}{T_2'} + \frac{1}{T_2^D} \tag{2.17}$$

T_2^* is also an effective measure of magnetic susceptibility (due to the T_2' component's sensitivity to susceptibility changes). Experimental work by Ogawa and Lee (1990) revealed that measurement of the T_2^* would be able to show contrast attributed to the magnetic susceptibility effect induced by paramagnetic deoxyhemoglobin in red blood cells. This initiated the beginnings of fMRI and research turned to discovering the cause of this effect, coined by Ogawa et al. (1990) as the blood-oxygenation level dependent or BOLD signal.

The BOLD contrast occurs through the differences in magnetic susceptibility of oxyhemoglobin and deoxyhemoglobin. When there is a change in the relative concentration of oxygenated and deoxygenated blood, there are also correlated changes in the BOLD signal. Oxyhemoglobin and the surrounding tissues are diamagnetic whilst deoxyhemoglobin is paramagnetic (Pauling and Coryell, 1936). Although findings for the paramagnetic properties of deoxyhemoglobin in blood were published in 1936, an application of the property had not been considered until more than 50 years later. Brooks and Chiro (1987) reviewed the MRI appearance of blood and concluded that "the field inhomogeneity created by the concentration of paramagnetism in the red blood cells lowers the effective T_2". Ogawa et al. (1990) used these findings and performed the first experiment showing such a contrast could be seen in brain MRI scans.

Models of the BOLD-fMRI signal stem from the theory of NMR signal behaviour in biological tissues in the presence of static magnetic field inhomogeneities. This was pioneered from modelling work done by Ogawa et al. (1993) and the extension of this theory by Yablonskiy and Haacke (1994) and Boxerman et al. (1995). The more recent versions of the NMR model of BOLD-fMRI by Buxton et al. (1998) and corrected by Obata et al. (2004) has used the basic framework provided by the pioneers.

The basic assumption of the BOLD-fMRI model is that the blood vasculature network of the brain has one value of magnetic susceptibility, whilst the tissue surround the network has another value. Furthermore, the voxel is also idealized: by Ogawa et al. (1993) as a three-dimensional matrix of cubes (tissues) containing a cylindrical blood vessel of random orientation (Figure 2.2), and by Yablonskiy and Haacke (1994) as an interconnecting, randomly distributed network of cylinders within a cube of tissue (Figure 2.3). Consequently, the symmetrical properties of cylinders simplified both models to identical mathematical equations.

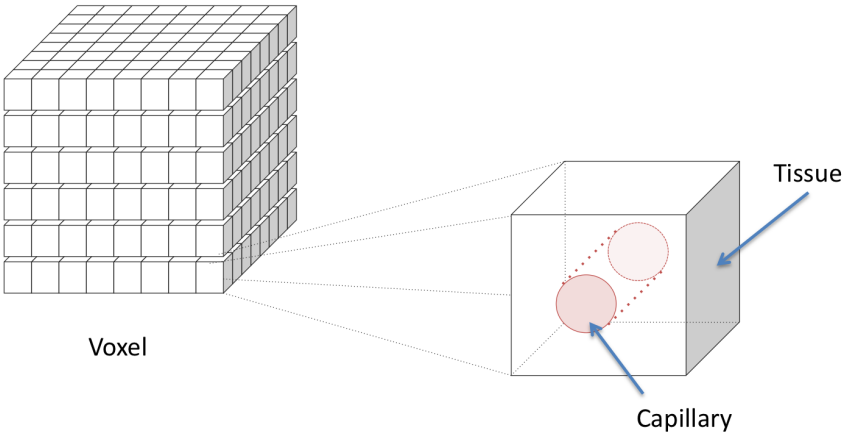

Figure 2.2: Model of the Voxel [adapted from Ogawa et al. (1993)].

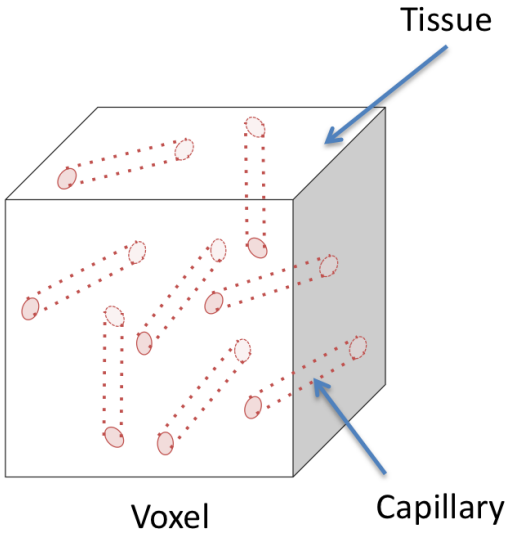

Figure 2.3: Model of the Voxel [adapted from Yablonskiy and Haacke (1994)].

Signal Changes within the Voxel Buxton et al. (1998) and Obata et al. (2004) used results of the Ogawa et al. (1993) model for signal modelling purposes in their integrative model of the hemodynamic origins of the BOLD signal. Their model is presented as follows. T_2^* is sensitive to magnetic susceptibility changes within the tissue, T_2'. Equation (2.17) can be rewritten by using relaxation rates (R) instead of time constants (T), substituting $R_2^* = \frac{1}{T_2^*}$, $R_2^0 = \frac{1}{T_2}$, $R_2^{(Hb)} = \frac{1}{T_2'}$ and $R_2^D = \frac{1}{T_2^D}$:

$$R_2^* = R_2^0 + R_2^{Hb} + R_2^D \tag{2.18}$$

In the formulation for the BOLD-signal the diffusion term, R_2^D, is assumed to be very small: the main effects being R_2^0 and R_2^{Hb}. The change in BOLD signal from the voxel can then modelled due to a difference in the amount of deoxy-hemoglobin to its baseline, $q(t) - q_0$, and the difference in the fraction volume to its baseline, $\lambda(t) - \lambda_0$. The overall BOLD signal, $b(t)$, is composed of the weighted average of signals from the blood within the capillary, $b^{(i)}(t)$, and the tissue outside of the capillary, $b^{(e)}(t)$.

First, the baseline signals are calculated. The signal, $b_0^{(h)}$, is the signal emitted by a homogeneous voxel of tissue. The baseline fractional volume occupied by the capillary is λ_0 and the baseline BOLD signal, b_0, is expressed as a combination of baseline intervascular $b_0^{(i)}$ and extravascular $b_0^{(e)}$ signals :

$$\begin{aligned} b_0 &= (1-\lambda_0)b_0^{(e)} + \lambda_0 b_0^{(i)} \\ b_0^{(e)} &= b_0^{(h)} e^{-TR \times R_2^0} \\ b_0^{(i)} &= b_0^{(h)} e^{-TR \times (R_2^0 + R_2^{Hb})} \end{aligned} \tag{2.19}$$

It is possible to define some more relationships be help with the definition. Let μ_0 be the base signal attenuation factor and μ be the additional attenuation factor from deoxyhemoglobin:

$$\begin{aligned} \mu_0 &= \frac{b_0^{(e)}}{b_0^{(h)}} = e^{-TR \times R_2^0} \\ \mu &= \frac{b_0^{(i)}}{b_0^{(e)}} = e^{-TR \times R_2^{Hb}} \end{aligned} \tag{2.20}$$

This allows the re-expression of $b_0^{(e)}$, $b_0^{(i)}$ and b_0:

$$\begin{aligned} b_0^{(e)} &= b_0^{(h)}\mu_0 \quad b_0^{(i)} = b_0^{(h)}\mu_0\mu \\ b_0 &= b_0^{(h)}\mu_0[(1-\lambda_0) + \mu\lambda_0] \end{aligned} \tag{2.21}$$

Activation of the brain induces further change and brings about the modulation of the baseline values $b_0^{(e)}$ and $b_0^{(i)}$. This allows the values to be expressed as time varying parameters. These intra- and extra-vascular signals are modified by the additional change in relaxation rates ($\Delta R_2^{(e)}$ and $\Delta R_2^{(i)}$) causes attenuation inside and outside the capillary ($\mu^{(i)}$ and $\mu^{(e)}$ respectively). Relationships are defined as:

$$\begin{aligned} \mu^{(e)} &= e^{-TR\times\Delta R_2^{(e)}} \\ \mu^{(i)} &= e^{-TR\times\Delta R_2^{(i)}} \end{aligned} \tag{2.22}$$

The BOLD signal is also modulated from baseline. It is also changed into a parameterize value and can be written as:

$$b(t) = b_0^{(h)}\mu_0\left[(1-\lambda(t))\mu^{(e)} + \lambda(t)\mu^{(i)}\right] \tag{2.23}$$

The normalized BOLD signal change ($\Delta b_n(t)$) can then be written as a function of baseline CBF flow (v_0) and the CBF response ($v(t)$) as opposed to $_0$ and $\lambda(t)$:

$$\begin{aligned} \Delta b_n(t) = \frac{b(t)-b_0}{b_0} &= \frac{b_0^{(h)}\mu_0\left[(1-\lambda(t))\mu^{(e)} + \lambda(t)\mu^{(i)}\right] - b_0\mu_0[(1-\lambda_0)+\mu\lambda_0]}{b_0\mu_0[(1-\lambda_0)+\mu\lambda_0]} \\ &= \frac{[(1-v(t))\mu^{(e)} + v(t)\mu\mu^{(i)}] - [(1-v_0)+v_0\mu]}{(1-v_0)+v_0\mu} \\ &= \frac{(1-v(t))e^{-TR\times\Delta R_2^{(e)}} + v(t)\mu e^{-TR\times\Delta R_2^{(i)}} - 1 + v_0 - v_0\mu}{1-v_0+v_0\mu} \end{aligned} \tag{2.24}$$

This equation provides an exact expression for modelling changes in signal. For small changes in relaxation rates $\Delta R_2^{(e)}$ and $\Delta R_2^{(i)}$, the exponential terms can be linearized using the well-known approximation:

$$e^{-x} \approx 1 - x \quad \forall\ [x : 0 < x \ll 1] \tag{2.25}$$

Furthermore, for small blood volumes as in the case of capillaries, the divisor $1-v_0+v_0\mu$ can be approximated to one and therefore the signal change can be simplified in order to give a linear relationship for ease of modelling:

$$\begin{aligned} \Delta b_n(t) = \frac{b(t)-b_0}{b_0} &\approx [1-v(t)](1-TR\times\Delta R_2^{(e)}) + v(t)\mu(1-TR\times\Delta R_2^{(i)}) - 1 + v_0 - v_0\mu \\ &\approx -TR\times\Delta R_2^{(e)} - \mu v(t)TR\times\Delta R_2^{(i)} - [v(t)-v_0](1-\mu) \end{aligned} \tag{2.26}$$

Expressions for μ, $\Delta R_2^{(e)}$ and $\Delta R_2^{(i)}$ can then be estimated and the equations will be shown in the following sections.

Extravascular Signal Changes Results of both Ogawa et al. (1993) and Yablonskiy and Haacke (1994) modelling susceptibility effects from randomly orientated cylinders showed that the transverse relaxation, R_2^*, for susceptibility differences between vessels and the surrounding tissues is:

$$R_2^* = 4.3\zeta(t)v(t) \text{ where } \zeta(t) = \zeta_0(1-\rho(t)) \tag{2.27}$$

$\zeta(t)$ is the frequency offset in Hz at the surface of the magnetized cylindrical vessel due to the difference in magnetic susceptibility. ζ_0 is the offset for fully deoxygenated blood ($40.3s^{-1}$ at 1.5T) and $\rho(t)$ is the fractional oxygen saturation. Note that if the blood is fully oxygenated ($\rho(t) = 1$), then the frequency offset, $\zeta(t)$, is zero and there is no susceptibility effect. Let $E(t) = 1 - \rho(t)$ be the oxygen extraction fractional or the ratio of deoxyhemoglobin to total hemoglobin and E_0 be its baseline value. Then it is possible to express $\Delta R_2^{(e)}$:

$$\begin{aligned}\Delta R_2^{(e)} &= 4.3\zeta_0 v(t)E(t) - 4.3\zeta_0 v_0 E_0 \\ &= 4.3\zeta_0[v(t)E(t) - v_0E_0] \\ &= 4.3\zeta_0[q(t) - q_0]\end{aligned} \tag{2.28}$$

Further analysis of the equation shows that if total deoxyhemoglobin content is defined as $q(t) = v(t)E(t)$ and baseline deoxyhemoglobin content is defined as $q_0 = v_0E_0$, then the change from baseline $q(t) - q_0 = v(t)E(t) - v_0E_0$ and so the extravascular signal change is only dependent upon the change in total deoxyhemoglobin content in the blood.

Intravascular Signal Changes Calculation of intravascular signal changes are determined by the sensitivity of the rate to the amount of deoxyhemoglobin in the blood. Li et al. (1998) acquired this data in a pig model and the results are placed in a linearized model about the range of oxygenation values from rest to strong activation ($\rho = 0.6-0.8$) or ($E = 0.2 - 0.4$). The change in relaxation rate, $R_2^{(i)}$, over this range is approximated to be:

$$\begin{aligned}\Delta R_2^{(i)} &= r_0E(t) - r_0E_0 \\ &= r_0[E(t) - E_0] \text{ with } r_0 = 25s^{-1} \text{ (Result of Li et al. (1998))}\end{aligned} \tag{2.29}$$

It can be interpreted from the equation that the intravascular signal change is only dependent upon the change in fractional deoxyhemoglobin content of blood.

Overall BOLD Signal Change from Voxel With both $\Delta R_2^{(e)}$ and $\Delta R_2^{(i)}$ defined, it then remains to describe the change in the BOLD signal:

$$\begin{aligned}\Delta b_n(t) &\approx -T \times \Delta R_2^{(e)} - \mu v(t) T \times \Delta R_2^{(i)} - [v(t) - v_0](1-\mu) \\ &\approx -4.3\zeta_0 T[v(t)E(t) - v_0 E_0] - \mu v(t) T r_0 [E(t) - E_0] - [v(t) - v_0](1-\mu) \quad (2.30)\end{aligned}$$

Equations describing the observed model of BOLD-fMRI (2.30) show that a change in the BOLD-fMRI signal, $\Delta b_n(t)$, is an expression of fractional deoxygenation and volume. As described in Section 2.3, fractional deoxygenation depends upon the $CMRO_2$, $c_n(t)$, volume has been found to depend upon blood flow, $f_n(t)$. Therefore, the observed model allows researchers to explain changes in BOLD-fMRI through changes in these physiologically based signals.

2.2.4 Observations of Biophysical Signals: A Summary

The biophysical nature of how fMRI signals are produced and measured have been presented in this section. Derivations of signal models were outlined from the basic principles of MRI signal production in tissues to (Section 2.2.1) to that of ASL-fMRI (Section 2.2.2) and BOLD-fMRI (Section 2.2.3) signals. As can be seen from the biophysical model derivations, the models for BOLD-fMRI and ASL-fMRI are very different and so may capture complementary attributes of the process of neuronal activation. Once the signals have been acquired, researchers have to deal with the issue of how these signals are related to each other in the neuronal activation cascade. This issue will be explored next.

2.3 Physiological Dynamics of Functional Imaging

Although observed models of functional imaging enable the processing of fMRI-signals into quantitative 4D images, the actual link to the underlying physiology generating such signals require other modelling processes. As seen in Figure 2.1, there are many physiological processes occurring within the brain; these link together to produce the changes being recorded using fMRI. Current research has focused upon building mathematical models to describe the measured relationships between the physiological signals so that signalling can be better understood. Most researchers modelling physiological dynamics attempt to correlate physiological signals back to BOLD-fMRI. Sections 2.3.1 and 2.3.2 discuss the primary frameworks proposed for the BOLD-fMRI signal. Models of CBF have not been as common as BOLD-fMRI models, even less so for ASL-fMRI

measurements of CBF. Much of the work modelling CBF have been done at the cellular level or as part of the BOLD-fMRI model; these models are discussed in Section 2.3.3.

2.3.1 Models of the $CMRO_2$ (Calibrated BOLD) Response

The $CMRO_2$ measurement or the 'calibrated BOLD' response as it is more commonly termed was a technique presented in seminal study by Davis et al. (1998) that is increasingly popular today (Leontiev and Buxton, 2007; Chiarelli et al., 2007; Perthen et al., 2008; Ances et al., 2009).

A large collection of experimental evidence supports the view that the $CMRO_2$ measurement is a better predictor of neuronal activity than the BOLD-fMRI signal. From an energetic perspective, it has been shown that the main energy costs of neuronal signalling comes from post-synaptic excitation, which consumes up to six times the energy (in the form of ATP) needed for pre-synaptic activity preceding it (Attwell and Iadecola, 2002). In the first step of the post-synaptic mechanism, a neuron is depolarised resulting in an influx of Na^+ ions into the cell that creates the action potential that propagates through to its neighbouring neurons. Secondly, the ionic balance of the cell has to be reset and the metabolism of glucose and oxygen under oxidative phosphorylation is required in order to generate the ATP that is needed to drive the Na^+/K^+ pump (Ames, 2000; Attwell and Laughlin, 2001; Erecińska and Silver, 1989). Experimental results from rats (Caesar et al., 2003; Offenhauser et al., 2005) as well as primates (Rauch et al., 2008a,b) indicate that post-synaptic excitation is indeed responsible for the consumption of cerebral oxygen. This is opposed to the BOLD-fMRI measurement that has been found to be more correlated with pre-synaptic activity as the work by Logothetis (2003) in motor unit action potentials was shown to be correlated with spiking (Raichle and Mintun, 2006).

The observed model for BOLD-fMRI derived in Section 2.2.3 predict that the changes in BOLD-fMRI signal depend upon changes in volume of the blood vasculature network in tissue, $v(t) - v_0$, as well as the change in fractional deoxygenation, $E(t) - E_0$. Fractional deoxygenation depends upon CBF, $f_n(t)$, and $CMRO_2$, $c_n(t)$. Therefore, an expression for the BOLD-fMRI signal can be expressed as a function of CBV, CBF and $CMRO_2$. Since CBF can be simultaneously measured using the ASL-fMRI technique and CBV can be expressed as a function of CBF, the $CMRO_2$ signal can be directly estimated and used.

CBF changes had originally been thought to have a linear coupling to the metabolic requirements of the tissue (Siesjö, 1978; Yarowsky and Ingvar, 1981). Regional correlation experiments of resting state data showed that areas with high blood flow tend to have high metabolic rates whilst areas with low flow have lower metabolic rates, showing re-

gional correlation between blood flow and metabolism (Raichle et al., 1976; Baron et al., 1984). However, Fox and Raichle (1986) demonstrated that the linear coupling does not hold true during activation. It was found that neuronal activation due to somatosensory stimulation resulted in CBF increases (29% above baseline) that far exceeded the increase in $CMRO_2$ (5% above baseline). As such, Fox and Raichle (1986) measured the ratio between the normalized increase CBF, $f_n(t)$, above baseline as compared to that of $CMRO_2$, $c_n(t)$, defined as:

$$n(t) = \frac{f_n(t) - 1}{c_n(t) - 1} \tag{2.31}$$

The time varying average of $n(t)$ within a local brain region is known as the coupling ratio, n_{av}. The earliest calculation of the ratio was determined by Fox and Raichle (1986) to be almost 6. Other earlier studies (Fox et al., 1988; Kuwabara et al., 1992) found such a significant increase in CBF with little or no $CMRO_2$ change that the term 'uncoupling' was used to describe the activation induced response. Later experiments using PET (Roland et al., 1987; Marrett and Gjedde, 1997) and fMRI (Davis et al., 1998; Hoge et al., 1999a; Kastrup et al., 2002; Stefanovic et al., 2004) all measured n_{av} to be between 2 and 3.

In creating the 'calibrated BOLD' model, Davis et al. (1998) assumed that the coupling ratio ($n(t)$) was constant throughout the experiment. They also used results two integral simulations: the first using results of Ogawa et al. (1993) which showed a linear relationship between the BOLD-fMRI signal and changes in CBV ; the second using results of Boxerman et al. (1995) which determined a power relationship between blood deoxyhemoglobin and magnetic susceptibility. Their construct of the measured BOLD-fMRI signal, $\Delta b_n(t)$, using CBF, $f_n(t)$, and $CMRO_2$, $c_n(t)$, is:

$$\Delta b_n(t) = M\left[1 - c_n(t)^{\beta} f - M(t)^{\alpha-\beta}\right] \tag{2.32}$$

The parameter α was previously empirically determined by Grubb et al. (1974). Using PET scans of anesthetized rhesus monkeys, Grubb et al. (1974) measured both CBF and CBV and used a line of best fit to map out the trend – fitting the data to a power relationship between CBF and CBV increases. Although this relationship has been used by many studies to set the value of α as 0.4, the link should be understood more as a correlation rather than a tight coupling may mistakenly be inferred from the equation

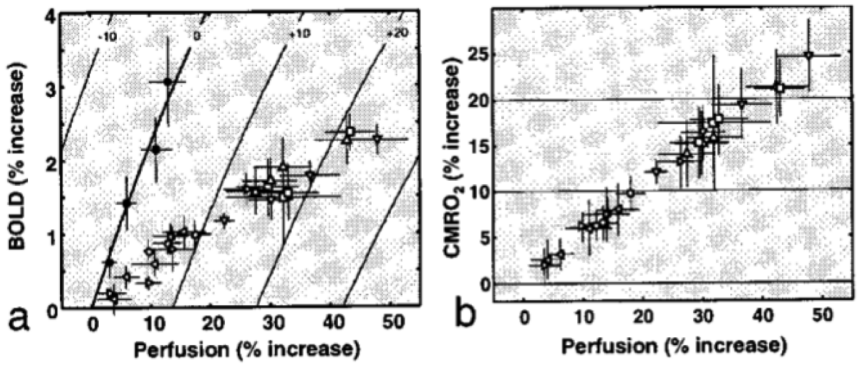

Figure 2.4: Calculation of M coupling constant between $CMRO_2$ and CBF [from Hoge et al. (1999b)]. a) shows the plot of BOLD vs CBF increases under induced hypercapnia. b) shows the estimation of $CMRO_2$ data using the calculated M value.

of the Grubb et al. (1974) study:

$$v(t) = 0.8f(t)^{\alpha}, \quad v_n(t) = \frac{v(t)}{v_0} = \left(\frac{f(t)}{f_0}\right)^{\alpha} = f_n(t)^{\alpha} \text{ where } \alpha = 0.38 \tag{2.33}$$

The parameter $\beta = 1.5$ in Equation (2.32) was determined through simulations of the influence of deoxyhemoglobin on magnetic susceptibility at 2% blood volume (Boxerman et al., 1995). The coefficient M is a resulting parameter that can be constructed using the simulations done by Ogawa et al. (1993) that produced a linear relationship between signal and volume changes. It is dependent upon magnetic field strength, acquisition time, the baseline CBV and the composition of the scanned tissue. M represents the hypothetical maximal change in BOLD signal, which may occur if CBF increases in a sufficiently short time so that there is no change in oxygen extraction (Chiarelli et al., 2007).

This proposed relationship allows estimation of $CMRO_2$ changes from combined, interleaved measurements of BOLD and CBF. The primary breakthrough of the Davis et al. (1998) study was its exploitation of results by Yang et al. (1994) showing that breathing a gas mixture with elevated concentration of CO_2 (hypercapnia) induced significant changes in CBF but not $CMRO_2$. By acquiring both BOLD and CBF signals as the subject responds to hypercapnia, a plot of BOLD and CBF values are obtained. An example of this is shown in Figure 2.4:

Assuming that the $CMRO_2$ level stays constant ($c_n(t) = 1$) throughout the calibration sequence, the BOLD signal is can be plotted against known changes in CBF and M can subsequently be determined (Hoge et al., 1999a,b). By doing this immediately before a cognitive task and assuming that the relationship holds, changes in $CMRO_2$ in latter

scans can then be estimated using the relationship:

$$c_n(t) = \left(1 - \frac{1}{M}\Delta b_n(t)\right)^{1/\beta} f_n(t)^{1-\alpha/\beta} \tag{2.34}$$

It should be noted that the Davis et al. (1998) formulation is a simplification of the NMR model for BOLD-fMRI (2.30). Davis et al. (1998) only considered the extra-vascular component of signal changes (2.28) which where computed through simulations by Ogawa et al. (1993) and Boxerman et al. (1995). It has been subsequently shown that the intra-vascular (2.29) contribution to the fMRI signal is negligible at high (7T) magnetic fields (Duong et al., 2003) but can be significant in low field (1.5T) scanners (Fujita, 2001).

Additional Improvements The Davis et al. (1998) model of BOLD-fMRI is limited by the simplifications that it assumes between variables within the model. The most debated variable is that of M. Estimation of M directly impacts upon estimation of n_{av}. Overestimation of M leads to under estimation of n_{av} and therefore incorrect estimation of n_{av} results in large systematic biasing when used in BOLD signal interpretation (Leontiev et al., 2007). Recent experiments have been conducted to understand the variability in n_{av}. Ances et al. (2008) showed that the ratio is not constant throughout the brain and found significant variation in n_{av} between the cortical ($n_{av} = 2.21$ in visual cortex) and sub-cortical ($n_{av} = 1.58$ in lentiform nuclei) regions. Furthermore, Liau and Liu (2009) found that both calibrated and experimental BOLD and CBF responses all showed a significant inverse dependence on baseline CBF, affecting inter-subject variability of the signal. Leontiev et al. (2007) found that variability of n_{av} across subjects improved significantly when a fixed M equal to the average M measurement across subjects was used for the calculation. The authors propose that assessment of the calibrated BOLD framework is needed to 'establish whether reported differences in n_{av} are due to physiological differences, population variability of intrinsic biases in the methods used'. Leontiev et al. (2007)'s conclusions suggest that the true variability of n_{av} is much smaller across individuals and has been raised artificially due to the variability in measurement of M. All of these errors greatly affect the measurement of the $CMRO_2$ signal and must be accounted for when using this framework for prediction.

Another source of error lies in the robustness of the parameters α and β. Although Hoge et al. (1999b) and Uludağ et al. (2004) showed that the model was robust to variability in parameters α and β, more recent evidence from Lin et al. (2008) refutes their claims. Furthermore Kida et al. (2007) found evidence of systematic bias of α under conditions of varying in stimulus frequency and duration. Experiments by Lu et al. (2003) has worked to rectify these shortcomings.

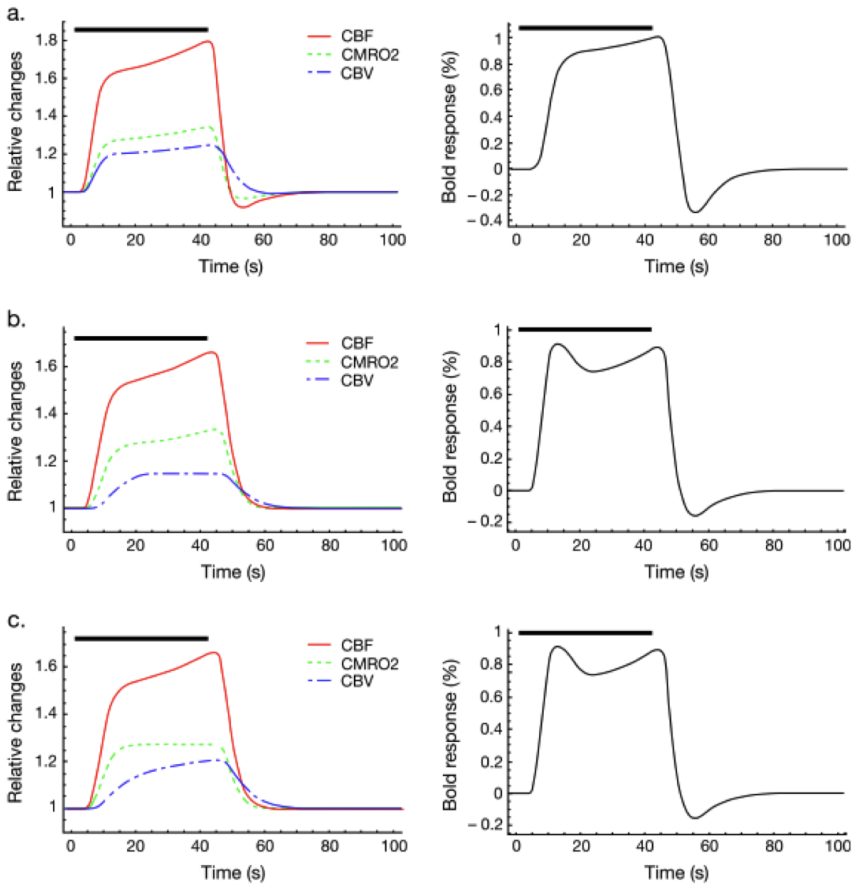

Figure 2.5: Modelling of M1 and SMA fMRI Data [from Obata et al. (2004)].

Simulations of BOLD-fMRI signal by Obata et al. (2004) modelling the motor (M1) and supplementary motor (SMA) areas show that tight coupling of CBF and $CMRO_2$ can generate BOLD-fMRI signals effects occuring in the M1, (Figure 2.5a). However shapes of signal found in the SMA could be generated both ways: firstly with tight coupling of CBF and $CMRO_2$ whilst CBV plateaus (Figure 2.5b) and secondly, without coupling and having CBV increase (Figure 2.5c). Note that the BOLD-fMRI signal generated by Figures 2.5b and 2.5c are virtually identical but the underlying physiology changes are very different. The simulations by Obata et al. (2004) show that estimation of $CMRO_2$ signal significantly improves when the BOLD, CBV, and CBF signals are all measured.

With the development of direct measurement of the CBV signal by Lu et al. (2003) using a technique known as VASO-fMRI, better accuracy is able to be obtained for estimation can be obtained. Although the problem of estimation of M is still present, the systematic bias of α is eliminated due to direct measurement of the CBV signal. Direct measurement of CBV $v_n(t)$ removes the error present in Grubb et al. (1974)'s

CBF/CBV power relationship (see Equation (2.33)) The equation is shown as follows:

$$\Delta b_n(t) = M\left[1 - c_n(t)^{\beta} f_n(t)^{-\beta} v_n(t)\right] \tag{2.35}$$

The $CMRO_2$ response is estimated by rearranging Equation (2.35):

$$c_n(t) = \left(1 - \frac{1}{M}\Delta b_n(t)\right)^{1/\beta} f_n(t)^{-1/\beta} v_n(t)^{-1} \tag{2.36}$$

This extended model, like Davis et al. (1998) model, only accounted for the extra-vascular component of signal changes (see Equation (2.28)). However, a systematic test of the $CMRO_2$ models by Lin et al. (2008) showed that when a separate model which took into account of the intra-vascular component was compared to the extra-vascular component only, there was minimal difference in estimation and Lin et al. (2008) concluded that they were effectively equivalent models. However, both models introduced the CBV measurement, $v_n(t)$, into the estimation of $CMRO_2$ and the experimental evidence show that the $v_n(t)$ values greatly affected estimations of $CMRO_2$ compared to the Davis et al. (1998) model.

The 'calibrated BOLD' framework relies on multiple signals ($b_n(t)$, $f_n(t)$ and $v_n(t)$) to be collected in order to determine the value of $c_n(t)$, thought to be a closer indicator for neuronal activity. The collection of multiple signals also has its disadvantages: firstly, the time for scanning becomes slower compared to if only the BOLD-fMRI signal was collected; secondly, the framework has to deal with measurement errors in all signals and there may be problems at lower temporal resolutions. Other groups have approached physiological modelling from a theoretical perspective and this is outlined in the next section.

2.3.2 Hemodynamic Models of the BOLD-fMRI Response

Although the BOLD-fMRI signal has been empirically found to be a sensitive tool for whole brain mapping of neuronal activation, it does not directly measure neuronal activation. The signal is sensitive to changes in physiology - CBV, CBF and $CMRO_2$ - that are collectively referred to as the hemodynamic response to neuronal activation. A example of the signal can be seen in Figure 2.6. Nonlinear features of the BOLD-signal that have physiological significance are:

- **Nonlinearity of increase to CBF compared to increase in $CMRO_2$:** The primary cause of the BOLD effect is due to an increase in CBF compared to an increase in $CMRO_2$. The increases in both signals were initially assumed to be lin-

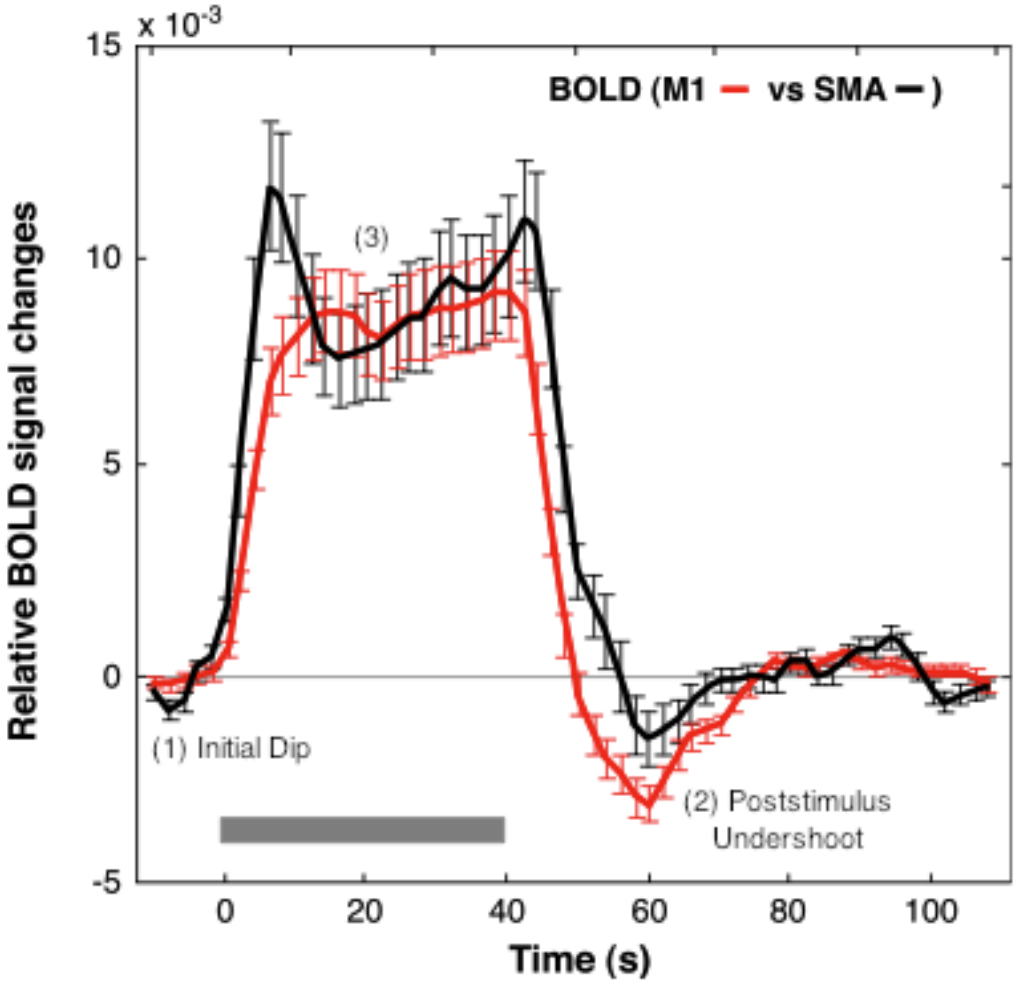

Figure 2.6: An example of a typical BOLD signal [from Obata et al. (2004)].

early coupled (Baron et al., 1984; Raichle et al., 1976). However, experiments (Kida et al., 2007; Lin et al., 2008) have shown that temporal and spatial aspect of the increases can vary depending upon the features of the stimulus (duration, frequency) and also depending upon the region of the brain that is stimulated (Ances et al., 2008). In addition to CBV changes, the combined behaviour of all three physiological signals produce the nonlinear features observed in BOLD-fMRI.

- **Initial Dip:** Experiments using BOLD-fMRI (Ernst and Hennig, 1994; Yacoub et al., 2001), as well as optical imaging (Malonek and Grinvald, 1996) has reported an initial dip of the BOLD signal, thought to be due to a rapid increase in $CMRO_2$ before the increase in CBF. Researchers have also thought that this initial dip could potentially better localize the area of activation (as indicated by increased metabolism) as the increase in CBF was found to cover a wider area in the brain (Malonek and Grinvald, 1996). The initial dip is a transitory response and is highly nonlinear. Evidence of the initial dip is not present in every experiment and it has been shown that both the magnitude and the temporal fluctuates with stimuli (Luo et al., 2009; Yeşilyurt et al., 2008; Perthen et al., 2008).

- **Post Stimulus Undershoot:** A post-stimulus undershoot of the signal is common in BOLD-fMRI experiments, thought to be the recovery of cells in the area to the applied stimulus. The undershoot lasts for 30 seconds or longer and is more pronounced when the stimulus has been applied for a longer period of time. Evidence of the CBF response having a shorter undershoot than the BOLD-fMRI signal suggests that recovery of signalling cells causes an increase in $CMRO_2$ (Lu et al., 2004).

- **Temporal Nonlinearity:** Comparing responses of the BOLD signal for brief and extended stimuli show that a linear translation of the brief response over predicts the true response to an extended stimulus. Studies have confirmed that responses to short-duration stimuli cannot be used to predict responses to long-duration stimuli in the visual (Vazquez and Noll, 1998; Yeşilyurt et al., 2008), auditory (Glover, 1999) and motor cortices (Glover, 1999). Furthermore, when two identical stimuli are presented close together, the total response is less than twice the response of single presentation (Huettel and McCarthy, 2001). These effects raise the possibility of habituation or energy conservation by the signalling neurons.

- **Negative BOLD:** Evidence of inhibition detection through BOLD was first reported by Shmuel et al. (2002) who found that a decrease in BOLD corresponded

to a decrease in spiking and thus could be a marker of neuronal deactivation. The study represented a major shift in interpretation of the 'negative' BOLD signal as it was originally thought that neuronal deactivation required the same energy needs as neuronal activation (Logothetis et al., 2001).

- **Other Exogenous Features:** Various other features have been found in the BOLD data to present more nonlinearity within the BOLD-fMRI signal. Phenomena include: ramping features (Harms and Melcher, 2003), stimulus offset spiking (Duff et al., 2007) and noise autocorrelation (Casanova et al., 2008).

Model-driven nonlinear estimation of the BOLD-fMRI signal began with the balloon-windkessel approach of Buxton et al. (1998) and Mandeville et al. (1999). The balloon model proposed by Buxton et al. (1998) used the observation that a volume of tissue can be modelled as an elastic compartment whose change in volume depends upon the rate of blood flow. The balloon model takes into account many features of the BOLD that cannot be modelled flexibly with traditional methods. Nonlinear behaviour such as the initial dip (2), the post-stimulus undershoot (3), and temporal shifting of the signal (4) can be simulated using this approach. However, other phenomena seen in the BOLD-fMRI signal such as the negative BOLD response (5) as well as extrogenous features such as task offset spikes and ramping (6) cannot be explained using this model.

Buxton et al. (1998)'s Balloon Model has been developed by many groups for BOLD-fMRI hemodynamics. The latest refinement extended by the same group (Buxton et al., 2004) and represents the state-of-the-art model in this field.

The basic premise of the Balloon model is that an increase in flow leads to a vaso-dilation of the capillary volume. Figure 2.7 shows the framework of the model. The balloon model expresses the causal relationships of the underlying physiology governing the BOLD-fMRI signal as a set of mathematical equations. In doing so, the model introduces variables that are not actually observed such as CBV, $v(t)$, CBF, $f(t)$, deoxyhemoglobin content, $q(t)$, and $CMRO_2$, $c(t)$. These variables are referred to as the hidden states of the model. The actual BOLD-fMRI signal, $b(t)$, can be predicted by investigating changes occurring in these states.

Figure 2.7 models the physiology through a set of mathematical relationships between the hidden states. They are marked as steps A to E in the figure. The responses are explained in detail.

The Neuronal Response (Step A) The model for stepping from the stimulus, $u(t)$, to neuronal activity, $\eta(t)$, was based upon observations of the response observed in

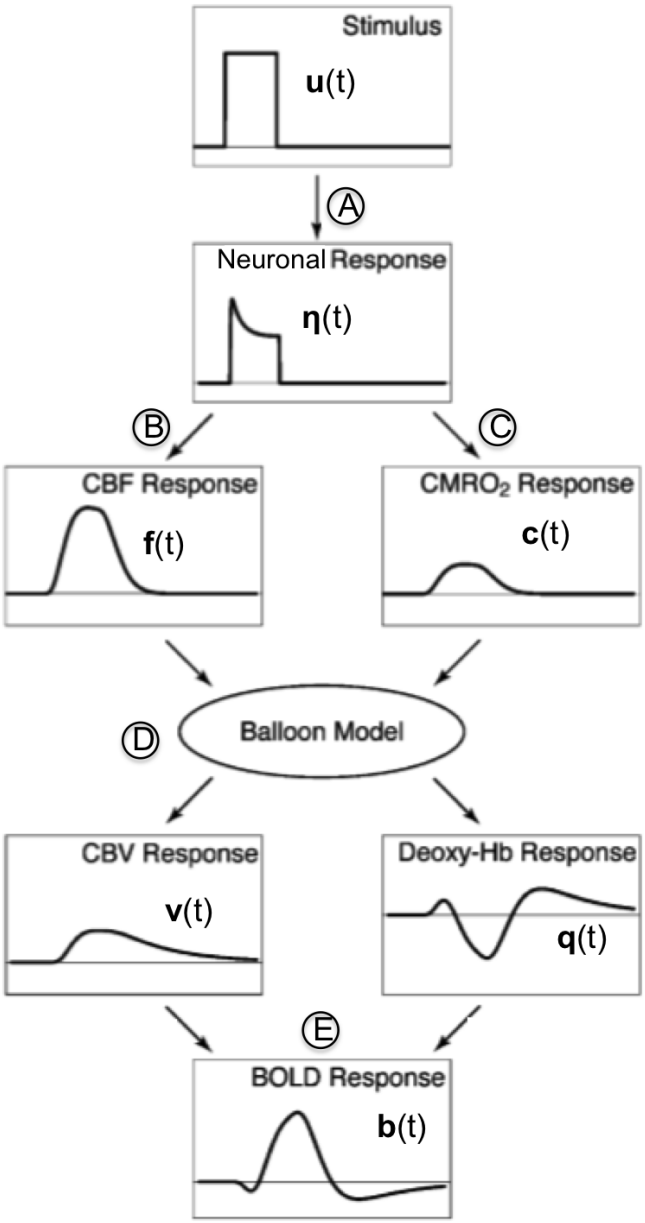

Figure 2.7: Overview of the Balloon Model [from Buxton et al. (2004)].

electrophysiology experiments (Logothetis, 2003). An inhibitory feedback system was chosen in which the neuronal response, $\eta(t)$, was treated as the difference between the stimulus input, $u(t)$, and an inhibitory response, $i(t)$. The inhibitory response is an exponential decay response with gain-factor of κ_i and time-constant τ_i. The set of equations are:

$$\begin{aligned} \eta(t) &= u(t) - i(t) \\ \frac{di(t)}{dt} &= \frac{\kappa_i \eta(t) - i(t)}{\tau_i} \end{aligned} \tag{2.37}$$

The Neurovascular Coupling Responses (Steps B and C) The models offers a linear model for the coupling of neuronal activity, $\eta(t)$, to both CBF, $f_n(t)$, and $CMRO_2$, $c_n(t)$. Although more substantial modelling of the coupling has been proposed, Buxton et al. (2004) used a simple assumption that the nonlinearity of signal changes found in previous experiments were as a result of the conversion between the stimulus, $u(t)$, to neuronal activity, $\eta(t)$, modelled in Step A and a simpler model could be therefore be introduced. The group assumed that both CBF and $CMRO_2$ are formed with linear convolutions of a gamma-variate function, $h(t)$. The form of the function is:

$$h(t) = \frac{1}{k\tau_h(k-1)!}\left(\frac{t}{\tau_h}\right)^k e^{-t/\tau_h} \tag{2.38}$$

with $k = 3$ and $\tau_h = 0.968$. The value of the parameters are used to set the shape of $h(t)$ to resemble experimental data. The responses for CBF, $f_n(t)$, and $CMRO_2$, $c_n(t)$, are then:

$$f_n(t) = 1 + (f_{max} - 1)h(t - \delta t_f) * \eta(t) \tag{2.39}$$

$$c_n(t) = 1 + (c_{max} - 1)h(t - \delta t_c) * \eta(t) \tag{2.40}$$

f_{max} and c_{max} are the maximum sustained values of $f_n(t)$ and $c_n(t)$ respectively and are assumed to follow a relationship given by $(f_{max} - 1) = (c_{max} - 1)n_{av}$ where n_av is the coupling ratio, explained in Section 2.3.1. δt_f and δt_c are introduced delays in activation for both responses. δt_f was assumed to be 1.0 seconds longer than δt_c, modelling the behaviour of the initial dip.

The Balloon Model (Step D) First proposed by Buxton et al. (1998) and Mandeville et al. (1999), this step is the central feature of the Buxton et al. (2004) model. It uses a biomechanical model, following the observation that CBV returned to baseline more slowly than CBF after the end of the stimulus. The equations have been revised by a

number of groups (Friston et al., 2000; Riera et al., 2004; Vakorin et al., 2007), however, the main idea of the mechanism remains the same; the venous compartment of the brain capillary network can be treated as a balloon having and input and output; blood flowing, $f_n(t)$, into the balloon affects the volume of the balloon, $v_n(t)$, which governs the blood flowing out of the balloon, f_{out}. The outputs of the model are normalized values of total deoxyhemoglobin, $q_n(t)$, and blood volume, $v_n(t)$. The equations are:

$$\begin{aligned} \frac{dq_n(t)}{dt} &= \frac{1}{\tau_{TT}}\left[f_n(t)\frac{E(t)}{E_0} - \frac{q_n(t)}{v_n(t)}f_{out}(v_n,t)\right] \\ \frac{dv_n(t)}{dt} &= \frac{1}{\tau_{TT}}\left[f_n(t) - f_{out}(v_n,t)\right] \\ f_{out}(v_n,t) &= v_n(t)^{\frac{1}{\alpha}} + \tau_v\frac{dv_n(t)}{dt} \end{aligned} \tag{2.41}$$

Parameters of the model are: τ_{TT}, the mean transit time through the balloon and is assumed by the model to be 3 seconds; τ_v, the time constant governing the initial resistance of a change in volume to the blood flow. The model proposed by Buxton et al. (2004) differs slightly from the original equation (Buxton et al., 1998) where the output $f_{out}(v_n,t)$ was modelled as a direct function of $v_n(t)$ without the resistance component. The addition of $\tau_v\frac{dv_n(t)}{dt}$ allows more flexibility in the shape of responses by changing the parameter τ_v.

The BOLD-fMRI Signal (Step E) The last step of the model uses results in Equation 2.30 to express BOLD-fMRI changes as a function of physiological changes. This step combines outputs of Step D deoxyhemoglobin $q_n(t)$, and blood volume $v_n(t)$ to form the BOLD-fMRI signal. Buxton et al. (2004) writes a more concise form of Equation (2.30):

$$\Delta b_n(t) \approx V_0[\nu_1(1-q_n(t)) - \nu_2(1-v_n(t))] \tag{2.42}$$

ν_1 and ν_2 combine the parameters of the fMRI scanner. The values of the parameters are determined to be $\nu_1 = 3.4$ and $\nu_2 = 1.0$ for a magnetic field of 1.5T with TE= 20ms and $E_0 = 0.4$, .

Extensions and Limitations to the Buxton et al. (1998) Model Modelling by Zheng et al. (2002, 2005); Zheng and Mayhew (2009) have extended the Buxton et al. (1998) model to include more features of the biomechanical mechanism of the relationship between CBF $f_n(t)$ and CBV $v_n(t)$. Zheng et al. (2002) included an additional capillary compartment to decouple the neurovascular response ($f_n(t)$ and $v_n(t)$) and the

cellular metabolic response, $q_n(t)$. The capillary model includes additional features: the modelling of dynamics in oxygen transport from the capillary; the modulatory effects of changes in tissue oxygen concentration; and the transient calculation of $CMRO_2$ as part of oxygen transport to tissue. Zheng et al. (2005) extends Zheng et al. (2002) to use a three-compartment model (arterial, venous and capillary compartments) for greater flexibility. Zheng and Mayhew (2009) modified the windkessel model to include characteristics typical of visco-elastic materials such as hysteresis, creep and stress relaxation. Such modelling adds more physiologically plausible characteristics to the original windkessel model.

Riera et al. (2006) also extended the Buxton et al. (1998) model by incorporating the model equations into a biophysical model of electrical and vascular dynamics within a cortical unit to explain both fMRI and EEG dynamics observed in experiments. Recent merging of optimization techniques (Vakorin et al., 2007) and comparison frameworks (Deneux and Faugeras, 2006) for imaging can determine whether these additional features are relevant to the analysis of actual data. Deneux and Faugeras (2006) compared different variations of the Balloon Model and found that the models were able to give better inferences of BOLD-fMRI signal than the GLM in most conditions. However, the group found that the Balloon Model was sensitive to signal noise; both the GLM and the Balloon models gave similar predictions when noise was increased.

A criticism of the Balloon Model has been the limited range of signal behaviour that the equations have been able to model. Typical outputs of the model can be seen in Figure 2.8a where the model is able to model both the initial dip, the post-stimulus undershoot as well as capture some nonlinear dynamics of the system. Actual BOLD-fMRI data have more variety as can be seen in Figure 2.8b. The major limitation of the Balloon Model lies in its inability to model onset and offset spiking behaviour (Figure 2.8b in Left M1, Right SMA, Right Thalamus, Left Temporal Cortex) as well as ramping behaviour (Figure 2.8b in Right SMA and Right Dentate Nucleus)

Current equations governing the Balloon Model are able to model ramping by changing the shape of $f_n(t)$ to also include a ramping term. However, sharp spiking behaviour at both onset and offset times cannot be modelled due to the smoothing effect of the windkessel compartment (Step D). As such, researchers have delved further into study of each individual hemodynamic signal (for example CBF and CBV) by modelling the biochemistry involved in producing such responses as well as the relationships between them. Focusing on the behaviour dynamics of an individual response allow the neuronal coupling of the response to be studied in full. The next section focuses on models of coupling between neuronal activation and CBF.

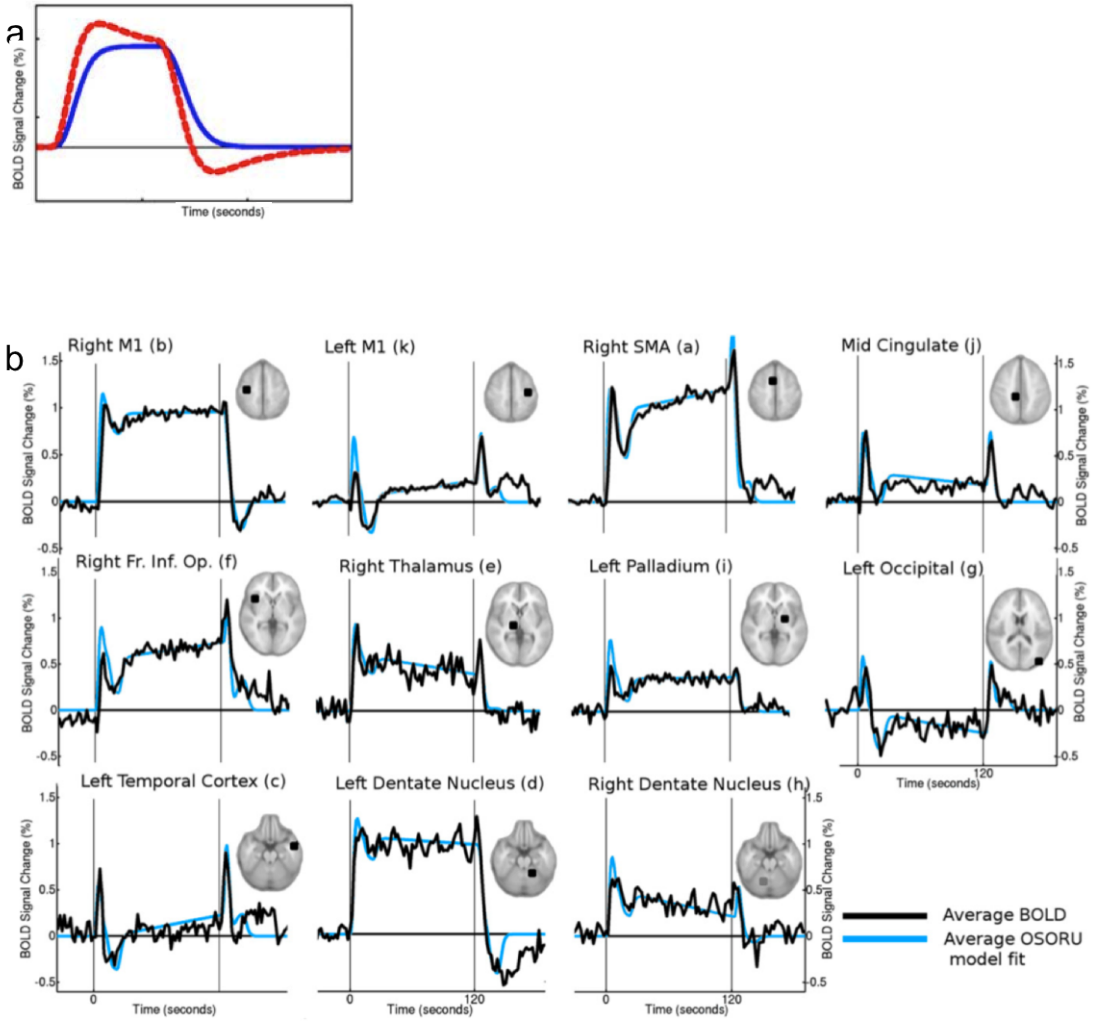

Figure 2.8: Predicted and Actual Responses of BOLD-fMRI Signal. a) Predicted Responses from Balloon Model [from Buxton et al. (2004)]. b) Actual BOLD-fMRI Signals Observed During Finger Tapping Task [from Duff et al. (2007)].

2.3.3 Models of the CBF Response

One stream of the research into the hemodynamic response has focused upon being able to understand the biological behaviour causing changes in brain physiology. The response most actively being pursued is the neurovascular response, or the mechanism driving regional CBF changes to a neuronal stimulus. Although the Roy and Sherrington (1890) experiment brought about the observation that the neurovascular response mechanism exists, quantifiable investigation into the mechanism has only been possible due to recent development of experimental techniques. Such a broad spectrum of experimental observations include data from *in vivo* studies of cellular changes in tissue slices or cell cultures, data from animal studies using fMRI (Logothetis, 2002), electrophysiology (Logothetis, 2003), optical imaging spectroscopy (OIS) (Jones et al., 2001) and laser doppler flowmetry (LDP) (Kennerley et al., 2005), and functional neuroimaging data from human experiments (Ances et al., 2009; Luo et al., 2009). Developing a coherent theoretical framework for describing the experimental observations has been the focus for groups attempting to understand the regulation of blood flow at the cellular and molecular level (Bennett et al., 2008a,b).

Most of the experimental work on modelling the biophysical aspects of neurovascular activity center around two models, the astrocyte-to-neuron transfer of lactate (ANLS) model (Aubert and Costalat, 2005; Aubert et al., 2007; Pellerin et al., 2007) and the neuron-to-astrocyte transfer of lactate (NALS) model (Simpson et al., 2007). Although they both agree that lactate is transferred from the one type of cell to another, they disagree on the direction of transfer. In both models, astrocyte activity plays a crucial role in the regulation of metabolic pathways on a cellular basis. The role of astrocytes, their connections to both the neurons and the capillaries and their role as the cellular inducer of neurovascular behaviour have been studied and modelled extensively (Jolivet et al., 2010).

Physiological models of CBF dynamics have not received as much attention. Theoretical modelling of the CBF response has generally been studied as part of the hemodynamic model of the BOLD-fMRI signal. An example of this can be seen in Equation (2.39), where the Buxton et al. (1998) model has incorporated an equation of $f_n(t)$ in its framework. Models describing CBF, $f_n(t)$, response to a stimulus, $u(t)$, have been described as either a 0th, 1st, or 2nd order differential system.

A 0th-order system is of the form:

$$f_n(t) - 1 = \epsilon u(t) \tag{2.43}$$

The change in CBF from baseline $(f_n(t)-1)$ is modelled as being a direct coupling of the stimulus. This coupling is used in the most basic analysis of CBF data, although $u(t)$ may have an affine transformation applied such as convolution with a gamma function. In terms of modelling dynamics of the CBF, the output of the system $(f_n(t)-1)$ would only follow features on the input, $u(t)$, and is limited in what it can do.

A 1st-order system is of the form:

$$\dot{f}_n(t) + k[f_n(t) - 1] = \epsilon u(t) \tag{2.44}$$

This system adds an extra parameter k which determines the rate at which the change $f_n(t) - 1$ proceeds. Instead of instantaneous coupling experienced in the 0th-order system, there is a transient time that is governed by k: When k is small, the coupling occurs slower, whilst larger k means faster coupling. The Buxton et al. (2004) model uses this system for modelling the CBF response to neuronal stimuli with an additional convolution with a gamma function.

From observation of nonlinear features in BOLD-fMRI signal, current researchers interpret the 'initial dip' as the CBF response lagging behind the $CMRO_2$ response. The delay factor is most easily modelled by viewing the CBF response having a spring/mass/damping mechanism typical of a 2nd-order differential system. Friston et al. (2000) incorporated this second order system into his solution of the Balloon model. The system was used by many subsequent groups including Johnston et al. (2008); Riera et al. (2004); Zheng et al. (2002). The 2nd-order system is of the form;

$$\ddot{f}_n(t) + k_1\dot{f}_n(t) + k_2[f_n(t) - 1] = \epsilon u(t) \tag{2.45}$$

2.3.4 CBF Modelling using Laser Doppler Flowmetry (LDF)

Although ASL-fMRI is a direct measurement of CBF, it is a non-invasive technique. The data can be better interpreted when underlying physiology governing is understood. Therefore better understanding of the relationship between neural activity and CBF are achieved when results from invasive studies are included in the modelling process. Techniques include OIS, measuring blood volume, LDF, measuring blood flow, and electrophysiology, measuring neuronal activation. All above signals provide much better temporal resolution than fMRI and so more features of the CBF response can be seen and modelled using these techniques.

A recent study by Zheng et al. (2010) used concurrent LDF and electrophysiology for modelling of the neurovascular coupling as a linear third-order dynamic system. The

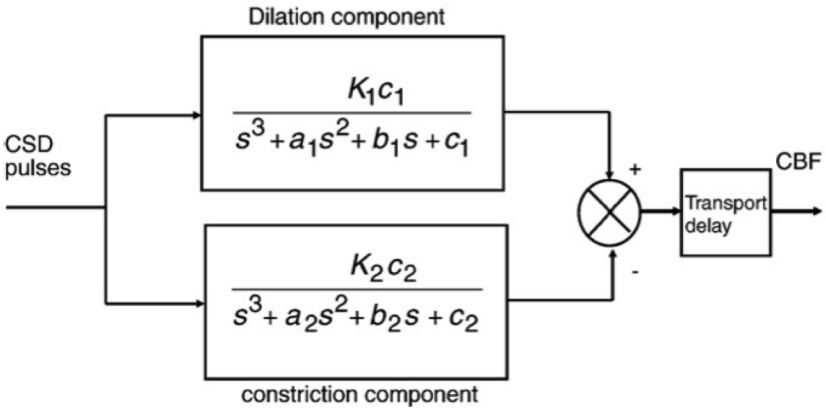

Figure 2.9: The Dilation/Constriction Model of Zheng et al. (2010).

study used electrical whisker stimulation of rats and measured both neuronal activity (using electrophysiology) and CBF (using LDF) in layer IV of the cortical surface. Their model used the idea that CBF changes induced by neuronal stimuli, $u(t)$, have a dilation component ($f_d(t)$ for modelling increases CBF) and a constriction component ($f_c(t)$ for modelling decrease in CBF) that is delayed by T_{delay} (the delay for initiation signal to propagate). Each of the components are represented as a separate third order system. The overall relationship can be written as a set of ordinary differential equations:

$$\begin{aligned}
&\dddot{f}_d(t) + a_1 \ddot{f}_d(t) + b_1 \dot{f}_d(t) + c_1 = K_1 c_1 u(t), && f_d(t) = \dot{f}_d(0) = \ddot{f}_d(t) = 0 \\
&\dddot{f}_c(t) + a_2 \ddot{f}_c(t) + b_2 \dot{f}_c(t) + c_2 = K_2 c_2 u(t), && f_c(t) = \dot{f}_c(0) = \ddot{f}_c(t) = 0 \\
&f_n(t + T_{delay}) = f_d(t) - f_c(t) && \qquad (2.46)
\end{aligned}$$

The system is visualized in Figure 2.9. Zheng et al. (2010)'s model represents the most recent model of CBF signal although it is for LDF instead of ASL-fMRI. Due to the high temporal resolution of LDF data, use of third order differential dynamics were required. It is a more complex model than the simple dynamics seen in Equations (2.43) to (2.45). Having more terms than Equations (2.43) to (2.45),Zheng et al. (2010)'s model can predict onset spiking due to the introduction of the difference terms $f_d(t) - f_c(t)$. Although ASL-fMRI data has traditionally been modelled using simpler dynamics, Zheng et al. (2010)'s work showed that there are more complicated dynamics in the data that can be utilized. As such, it is hypothesised that including higher-order dynamics for ASL-fMRI may allow for better interpretation of the CBF signal.

2.4 Chapter Summary

The motivating factors for modelling ASL-fMRI data were established in this chapter. Models of fMRI signals and the physiology governing these were explained in detail. As this chapter has shown, there are many signals and methods that can be used for evidence of neuronal activation each having their own unique biophysical signal model. However, if the most widely cited hemodynamic model (Buxton et al., 1998) is accepted, the corollary of the model is that the CBF signal is closer in physiology to neuronal activation than the BOLD signal. Our motivation to concentrate solely upon modelling CBF data was largely based on the corollary of the Buxton et al. (1998) model.

The final section of this chapter presented CBF models of various complexity. Models range from simple coupling of stimuli and CBF to third-order dynamics, introduced by Zheng et al. (2010) for analysis of LDF measurements. Although the ASL-fMRI signal has less temporal resolution than LDF, it too may include higher order dynamics. It is envisaged that experimental results can be used to construct a more meaningful model of CBF behaviour for ASL-fMRI datasets. Thus, a model governing direct correlation between neuronal activity and ASL-fMRI data may be constructed. This will be explored in more detail in the latter chapters.

Chapter 3

Outline of Investigation and Methods

As outlined in the introduction, the key research question is whether ASL-fMRI data can be modelled better than the existing methods through inclusion of physiologically grounded parameters. In order to begin addressing this issue, two further questions arise: (1) What type of dynamics are suitable for the modelling of ASL-fMRI data? and (2) Can transient features such as spiking and ramping, measured for CBF using other techniques also be found in ASL-fMRI data? Chapter 2 showed that CBF signal dynamics has been one of the major areas of research as part of the investigation into the underlying physiology of the BOLD-fMRI signal. Although many experiments have used a variety of correlations and models of CBF, they have not focused on modelling ASL-fMRI data by itself. The main concern for researchers using ASL-fMRI data for modelling is its low temporal resolution compared to invasive methods such as LDP. However if such a model exists and can be verified, the advantage provided by fMRI in measuring simultaneous whole brain dynamics enables a much broader picture of interactions across the brain.

In this chapter, a novel framework of CBF models is described; the models are inspired from physiological responses observed in CBF experiments. The framework attempts to address the two questions presented in the previous paragraph The questions are investigated through analysis of simulated and experimental CBF data. The next section presents an overview of CBF models proposed using the novel framework. All the methods and algorithms used in the framework such as the process for selecting the best models for ASL-fMRI and the theory of numerical methods used in such an analysis are presented. This chapter will introduce all the necessary theory that will be used in the two following chapters in order to address our key question: Can ASL-fMRI data can be modelled better than the existing methods through inclusion of physiologically grounded

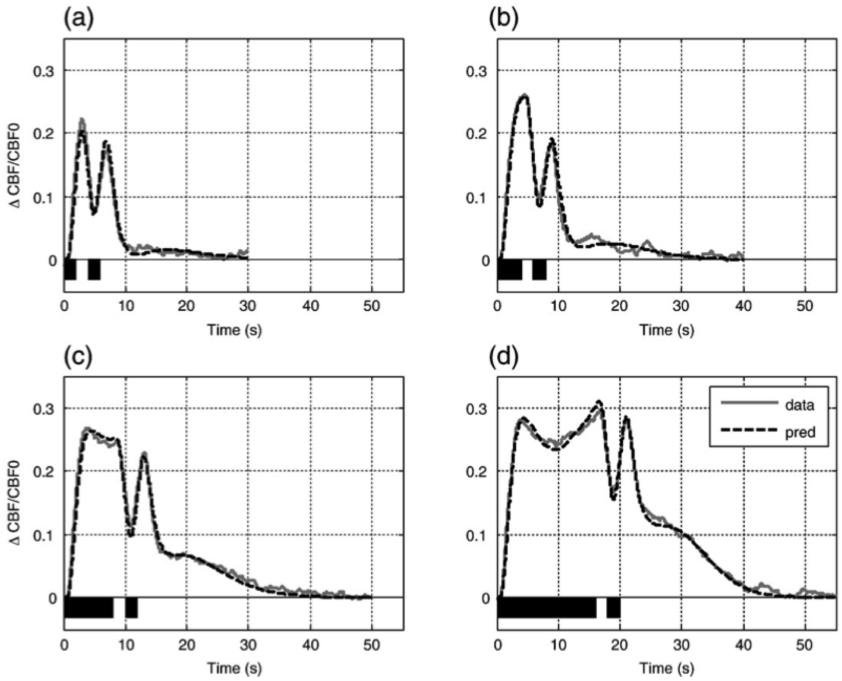

Figure 3.1: Prediction of actual data using the Dilation-Constriction Model [from Zheng et al. (2010)]. The graph shows predicted and measured changes in $f(t)$ using average data for 5 subjects. The fits are for block stimulus of a) 2, b) 4, c) 8, and d) 16 seconds.

parameters?

3.1 CBF Features to be Modelled

Many theoretical models of CBF were introduced in Chapter 2 ranging from simple linear coupling with the stimulus (0th-order dynamics) to much complicated systems such as the 3rd-order system introduced by Zheng et al. (2010). CBF data obtained using LDF requires more complex dynamics were needed the data had a much higher temporal resolution than data collected using ASL-fMRI. The model was used to estimate changes in CBF (Figure 3.1) in rats using whisker stimuli for blocks of various length (2, 4, 8 and 16 seconds). It can be seen that the predictions generated by the model are a very close fit to that of the actual measured data. Data collected by Zheng et al. (2010) showed that the CBF response has features that may affect the shape of the BOLD-fMRI response. Figure 3.2 shows typical fits of the model.

Transient features observed in Figure 3.1 were modelled very accurately using the Zheng et al. (2010) model; the equations providing very accurate fits for CBF over 16 seconds. However, other features in the CBF signal encountered in other experiments such as ramping over long periods of time (seen in Figure 3.3) cannot be accounted using the

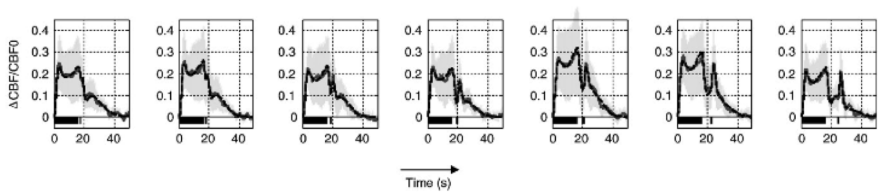

Figure 3.2: Prediction of 16 second stimuli using the Dilation-Constriction Model [from Zheng et al. (2010)].

Dilation/Constriction model.

A further limitation of the Zheng et al. (2010) model is that offset spiking cannot be modelled for longer stimulations. The equations are not flexible enough to accommodate such features. As such, models of CBF have to include these additional features in the signal in order to truly encompass all the possible signals that can be seen in CBF data. Development of a CBF model that includes offset spiking and ramping can have definite advantages for modelling of CBF data. Such models will be introduced in the next section.

3.2 Framework for Modelling CBF

Although many models have been proposed for CBF (Section 2.3.3), the models are limited in the amount of features that can be described. The 2nd-order system proposed by Friston et al. (2000) has been the most widely-used model of CBF. However the model has a few short-comings; the system does not describe certain characteristics of CBF data acquired using LDF (spikes and ramping seen in Figure 3.2) as well as ASL-fMRI (ramping seen in Figure 3.3).

New models for describing these transient behaviors are now proposed. A new term ϵ_1 governing brain activity changes that come about from instantaneous changes in stimulus is proposed as the coefficient of $\frac{d}{dt}u(t)$. Offset spiking is introduced as ϵ_4. Since ϵ_4 is the offset equivalent of ϵ_1, the two terms are collectively known as 'spiking' coefficients. The original ϵ coefficient coined by Friston et al. (2000), a term that measures changes proportional to the stimulus becomes ϵ_2. A term related to the integration of stimulus (ϵ_3) is introduced as a coefficient of $\int u(t)\,dt$. Furthermore, transient dynamics are scaled in proportion to the input stimulus $u(t)$. The complete equation for the extended system

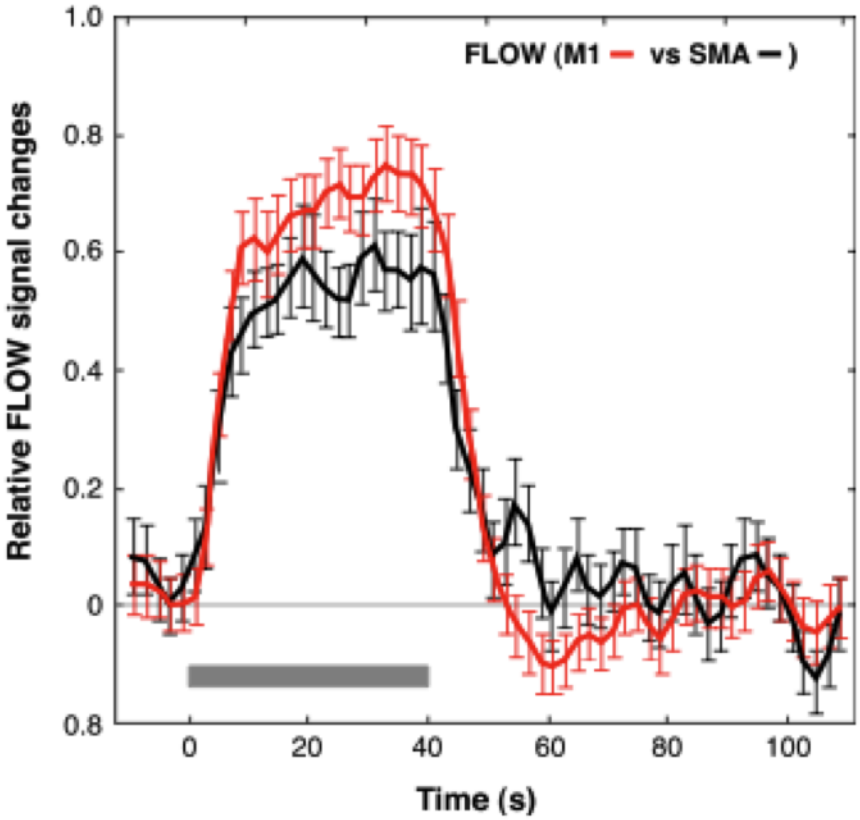

Figure 3.3: CBF data acquired using ASL showing ramping response [from Obata et al. (2004)].

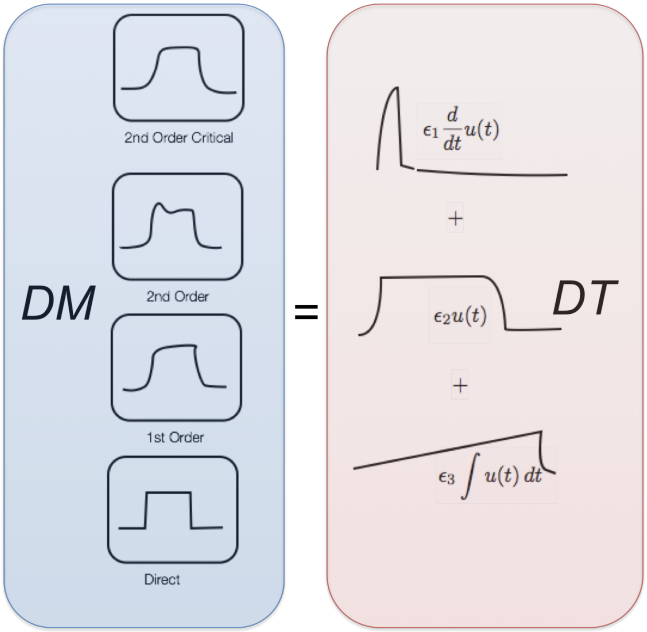

Figure 3.4: Dynamic Models and Driving Terms.

using 2nd-order dynamics is written as:

$$\begin{aligned}\frac{1}{k_2}\ddot{f}_n(t) + \frac{k_1}{k_2}\dot{f}_n(t) + [f_n(t) - 1] &= \epsilon_1 \frac{d}{dt}u(t) + \epsilon_2 u(t) + \epsilon_3 \int u(t)\,dt, \quad 0 < t < T_{ON} \\ \frac{1}{k_2}\ddot{f}_n(t) + \frac{k_1}{k_2}\dot{f}_n(t) + [f_n(t) - 1] &= \epsilon_4 \frac{d}{dt}u(t), \qquad\qquad\qquad\qquad\quad t \geq T_{ON}\end{aligned} \tag{3.1}$$

The onset response is from $0 < t < T_{ON}$ and the offset response is from $t \geq T_{ON}$ where T_{ON} is the time in which the stimulus is applied. This represents the most general of all system for modelling CBF that are proposed. Subsequently, additional systems can be derived. Equation (3.1) can be broken up into two parts:

A Dynamic Model (DM) Equation:

$$DM = \frac{1}{k_2}\ddot{f}_n(t) + \frac{k_1}{k_2}\dot{f}_n(t) + [f_n(t) - 1] \tag{3.2}$$

And a Driving Term (DT) Equation:

$$DT = \begin{array}{ll} \epsilon_1 \frac{d}{dt}u(t) + \epsilon_2 u(t) + \epsilon_3 \int u(t)\,dt, & 0 < t < T_{ON} \\ \epsilon_4 \frac{d}{dt}u(t), & t \geq T_{ON} \end{array} \tag{3.3}$$

By incorporating combinations of DM and DT, different CBF models can be produced. This is depicted in Figure 3.4. DM determines the shape of the response $f_n(t)$. Not only are 2nd-order systems modelled but 1st and 0th order systems can also be included. The DT selects features that are to be included in the model (ie. ϵ_1 and ϵ_4 determines spiking, ϵ_2 determines linear coupling and ϵ_3 determines ramping).

The Dynamic Model Equations incorporate the main CBF models proposed in Chapter 2.3.3 and are shown in order beginning with the 0th-Order model, taken from the LHS of Equation (2.43):

$$DM_0 = f_n(t) - 1 \tag{3.4}$$

1st-Order, taken from the LHS of Equation (2.44):

$$DM_1 = \frac{1}{k}\dot{f}_n(t) + [f_n(t) - 1] \tag{3.5}$$

2nd-Order Critical, taken from the LHS of Equation (2.45), but further simplified by assuming that the 2nd-order behaviour was critically damped and so $k_2 = \frac{k_1^2}{4}$, yielding

a critically damped model:

$$DM_{2a} = \frac{4}{k_1^2}\ddot{f}_n(t) + \frac{4}{k_1}\dot{f}_n(t) + [f_n(t) - 1] \tag{3.6}$$

2nd-Order Non-Critical, taken from the LHS of Equation (2.45):

$$DM_{2b} = \frac{1}{k_2}\ddot{f}_n(t) + \frac{k_1}{k_2}\dot{f}_n(t) + [f_n(t) - 1] \tag{3.7}$$

The Dynamic Model Equations are coupled with Driving Term equations, which are formulated using the selection of combinations of Spikes, Linear Coupling and Ramping features:

CBF Model Driving Terms						
Models		*Spiking*		*Coupling*		*Ramping*
DT_1	=	$\epsilon_1 \frac{d}{dt}u(t)$				
DT_2	=			$\epsilon_2 u(t)$		
DT_3	=	$\epsilon_1 \frac{d}{dt}u(t)$	+	$\epsilon_2 u(t)$		
DT_4	=					$\epsilon_3 \int u(t)\,dt$
DT_5	=	$\epsilon_1 \frac{d}{dt}u(t)$			+	$\epsilon_3 \int u(t)\,dt$
DT_6	=			$\epsilon_2 u(t)$	+	$\epsilon_3 \int u(t)\,dt$
DT_7	=	$\epsilon_1 \frac{d}{dt}u(t)$	+	$\epsilon_2 u(t)$	+	$\epsilon_3 \int u(t)\,dt$

Table 3.1: Driving Term Equations.

Note that only the onset equations are shown. ϵ_4 is also considered spiking behaviour and so becomes implemented in DT_1, DT_3, DT_5 and DT_7 along with ϵ_1. Therefore, a matrix of models can be generated using combinations of Dynamic Models and Driving Terms:

CBF Model Matrix				
	Dynamic Models			
Driving Terms	DM_0	DM_1	DM_{2a}	DM_{2b}
DT_1	$DM_0 = DT_1$	$DM_1 = DT_1$	$DM_{2a} = DT_1$	$DM_{2b} = DT_1$
DT_2	$DM_0 = DT_2$	$DM_1 = DT_2$	$DM_{2a} = DT_2$	$DM_{2b} = DT_2$
DT_3	$DM_0 = DT_3$	$DM_1 = DT_3$	$DM_{2a} = DT_3$	$DM_{2b} = DT_3$
DT_4	$DM_0 = DT_4$	$DM_1 = DT_4$	$DM_{2a} = DT_4$	$DM_{2b} = DT_4$
DT_5	$DM_0 = DT_5$	$DM_1 = DT_5$	$DM_{2a} = DT_5$	$DM_{2b} = DT_5$
DT_6	$DM_0 = DT_6$	$DM_1 = DT_6$	$DM_{2a} = DT_6$	$DM_{2b} = DT_6$
DT_7	$DM_0 = DT_7$	$DM_1 = DT_7$	$DM_{2a} = DT_7$	$DM_{2b} = DT_7$

Table 3.2: Matrix of Models from Combination of DM and DT Equations.

With four DM equations and seven DT equations, a total of twenty-eight different CBF models can be generated. In order to determine the best model for ASL-fMRI data, a

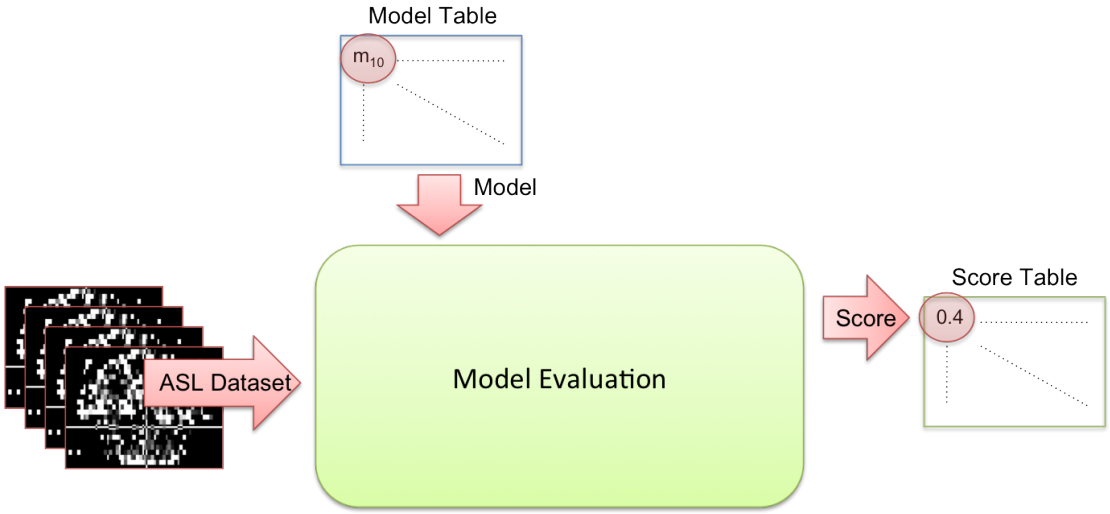

Figure 3.5: Workflow for Ranking Models.

method for evaluation of real data is required. This is presented next.

3.3 Model Evaluation Workflow

The proposed generalized CBF modelling framework allows flexibility to choose of models for a set of experimental data. Performance of the new models are evaluated for their accuracy in modelling ASL-fMRI data although the framework could potentially be modified so that other types of data could also be read in and analysed. Figure 3.5 shows the overview of what the evaluation workflow accomplishes. Individual CBF Models that have been proposed in Table 3.2 are used to evaluate an ASL-fMRI dataset. The end result of such an evaluation is a score given to the model. This score is based upon the accuracy of fit as well as the number of parameters in the model. The highest scoring model is deemed the best candidate for analysis of the ASL-fMRI dataset.

Figure 3.6 shows the actual process of model evaluation. The model is used to fit time-series data from each voxel of each scan within the dataset. The parameters governing the behaviour of the model are recorded for all voxels form 3 dimensional parameter maps, one for each scans. Furthermore, the variance in the estimation between the model generated value and the actual observed value are also recorded as 3 dimensional maps. The parameter maps and the variance maps are used in a group analysis to determine the accuracy of using such a model in estimation of ASL-fMRI signals dynamics and a score is given for the analysis to be compared with other models.

Group analysis of the scans involve transforming all the scans to a standard brain image, comparing the mean and variance of parameter estimates for voxels across the brain as

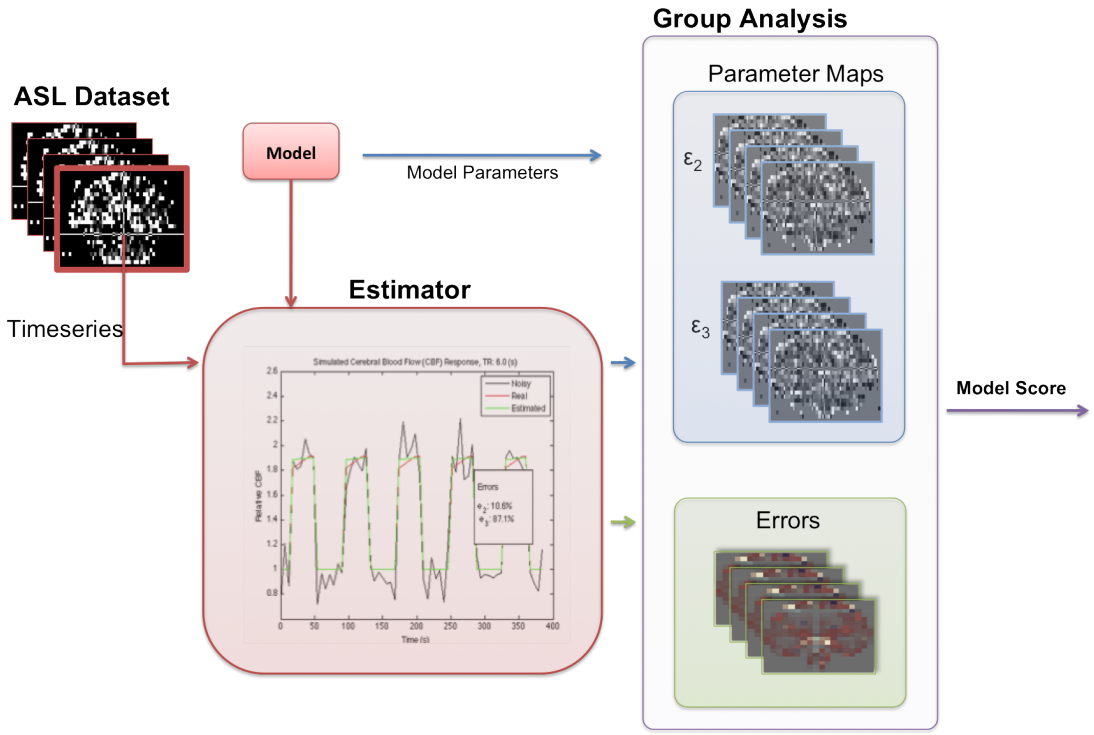

Figure 3.6: Workflow for Evaluation and Scoring of Models.

well as the overall error for the estimation across the brain. The statistic for model comparison is done using both the Akaike Information Criterion (AIC) and the Bayesian Information Criterion (BIC), that return a success of fit based upon the likelihood of fit as well as a penalty term based upon the number of observations made and the number of parameters in the model. This is more thoroughly explained in Section 3.7. Once model comparison is done on a voxel level for the group, the best estimate is found by calculating the percentage of total voxels each model is deemed to be the highest quality fit. The model with the highest total percentage of voxels is determined to be the best model for the ASL-fMRI dataset. Subsequent sections in this chapter explain the process in more detail.

3.4 Estimation of Model Parameters

The theoretical model for ASL-fMRI signal derived in Section 2.2.2 and Equation 2.16 shows the noise-free representation of the signal. Measurement of the signal, however is noisy.

Therefore, let $f_k^{(m)}$ be the actual CBF value at a time-point in the voxel time-series observed using ASL-fMRI having total time T_{total} and sampled every T seconds. The vector $\mathbf{y^{(f)}}$ is of total length N where $N = \frac{T_{total}}{T}$. The elements of $\mathbf{y^{(f)}}$ are y_k where

$k = 1 \dots N$ can be defined as:

$$y_k = f_k^{(m)} + e_k,\ k = 1 \dots N \tag{3.8}$$

$\mathbf{y^{(f)}}$ represents the measured CBF value of a system and because it is measured, there is always an error e_k associated with the measurement at any time-point k. The equation can be expressed in vector notation:

$$\mathbf{y^{(f)}} = \mathbf{f^{(m)}} + \mathbf{e} \tag{3.9}$$

Moreover, there is a theoretical model associated with $\mathbf{f^{(m)}}$ represented mathematically by $g(X, \beta)$ where the model parameters are defined as β, the independent variables or inputs are defined as X, and the relationship governing parameters and inputs of the model is defined as g. So a general model of CBF measurement can be represented in this form:

$$\mathbf{y^{(f)}} = g(X, \beta) + \mathbf{e} \tag{3.10}$$

Where:

$$\mathbf{y^{(f)}} = \begin{bmatrix} y_1 \\ y_2 \\ . \\ . \\ . \\ y_N \end{bmatrix} \quad X = \begin{bmatrix} x_{11} & \dots & x_{1p} \\ x_{21} & \dots & x_{2p} \\ . & \dots & . \\ . & \dots & . \\ . & \dots & . \\ x_{N1} & \dots & x_{Np} \end{bmatrix} \quad \beta = \begin{bmatrix} b_1 \\ . \\ . \\ b_p \end{bmatrix} \quad \mathbf{e} = \begin{bmatrix} e_1 \\ e_2 \\ . \\ . \\ . \\ e_N \end{bmatrix} \tag{3.11}$$

The error term $\mathbf{e}$ captures all other outside influences on the data unrelated to the blood flow model, $\mathbf{f^{(m)}} = g(X, \beta)$. Most estimation models assume the properties of the errors ($\mathbf{e}$) of the system are normally distributed.

Model estimation assumes that g, X and $\mathbf{y^{(f)}}$ are known or can be observed and β, the parameters of the model are unknown. The function g has to be specified and is based upon predetermined knowledge about the relationship between $\mathbf{y^{(f)}}$ and X. Regression analysis requires that there is enough information in the data to estimate a unique β ($N > p$) so that the model is always an over-determined system. In most cases, the least squares regression model is used so that a solution is found for β that minimizes the distance between the measured and predicted values of $\mathbf{y^{(f)}}$. This is done by minimizing the sum of error terms, $\mathbf{e}^T\mathbf{e}$ with relation to β. Let $\mathbf{x}_i$ be the i-th row of

X ($\mathbf{x}_i = [x_{i1}, ..., x_{ip}]$), the equation is:

$$\begin{aligned} S(\beta) &= \mathbf{e}^T\mathbf{e} \\ &= \sum_{i=1}^{n}[y_i - g(\mathbf{x}_i, \beta)]^2 \end{aligned} \tag{3.12}$$

This technique in estimation of β is called least squares estimation and includes two main types of estimation technique - nonlinear least squares estimation and least squares estimation based on whether g is linear or nonlinear. The techniques will be further elaborated in the following sections.

3.5 Nonlinear Least Squares Estimation

Nonlinear least squares estimation uses an iterative approach to obtain an estimate for β when g is nonlinear. There are many methods used for estimation and choice of method depends upon the preference of the user for robustness, accuracy, speed and other factors. Nonlinear least squares methods does not offer a global solution for the problem but finds a local minima based upon the initial point that the user chooses to begin interpolation.

Most software applications for generic curve-fitting problems use the Levenberg-Marquardt Algorithm (LMA). The algorithm was used in analysis for parameter estimation via the 'lsqnonlin' MATLAB function. A description of the method is provided as follows: Starting with the Equation (3.12), the aim is to minimize $S(\beta)$ by providing an initial guess for β (let $\beta = \beta_0$) and then using the algorithm to calculate a new value of β that would then replace the previous one at each iteration. β is replaced by $\beta + \delta$ where the value for δ is different depending upon the algorithm used. LMA is a variation of Newton's Method, where the new function can be approximated by the linearisation around β:

$$g([\mathbf{x}_i, \beta + \delta) \approx g(\mathbf{x}_i, \beta) + J_i\delta \text{ where } J_i = \frac{\partial g(\mathbf{x}_i, \beta)}{\partial \beta} \tag{3.13}$$

The sum of squares equation with the new value of β can be expressed as:

$$S(\beta + \delta) \approx \sum_{i=1}^{n}[y_i - g(\mathbf{x}_i, \beta) - J_i\delta]^2 \tag{3.14}$$

The sum of squares, $S(\beta + \delta)$, is a minimum if the gradient of S with respect to δ is

zero. $S(\beta+\delta)$ is expressed in vector form:

$$\begin{aligned} S(\beta+\delta) &\approx ||\mathbf{y}^{(\mathbf{f})} - g(X,\beta) - \mathbf{J}\delta||^2 \\ &\approx [\mathbf{y}^{(\mathbf{f})} - g(X,\beta) - \mathbf{J}\delta]^T[\mathbf{y} - g(X,\beta) - \mathbf{J}\delta] \\ &\approx \mathbf{y}^{(\mathbf{f})^T}\mathbf{y}^{(\mathbf{f})} - \mathbf{y}^{(\mathbf{f})^T}g(X,\beta) - \mathbf{y}^{(\mathbf{f})^T}\mathbf{J}\delta - g(X,\beta)^T\mathbf{y}^{(\mathbf{f})} + g(X,\beta)^Tg(X,\beta) \\ &\quad + g(X,\beta)^T\mathbf{J}\delta - \delta^T\mathbf{J}^T\mathbf{y}^{(\mathbf{f})} + \delta^T\mathbf{J}^Tg(X,\beta) + \delta^T\mathbf{J}^T\mathbf{J}\delta \end{aligned} \tag{3.15}$$

The derivative of $S(\beta+\delta)$ can be calculated with respect to δ and then setting the result to zero and solving for δ:

$$\begin{aligned} \frac{\partial S(\beta+\delta)}{\partial \delta^T} &= -\mathbf{J}^T\mathbf{y}^{(\mathbf{f})} + \mathbf{J}^Tg(X,\beta) + \mathbf{J}^T\mathbf{J}\delta \\ &= 0 \\ \therefore \quad \mathbf{J}^T\mathbf{J}\delta &= \mathbf{J}^T[\mathbf{y}^{(\mathbf{f})} - g(X,\beta)] \\ \therefore \quad \delta &= (\mathbf{J}^T\mathbf{J})^{-1}\mathbf{J}^T[\mathbf{y}^{(\mathbf{f})} - g(X,\beta)] \end{aligned} \tag{3.16}$$

The Levenberg's contribution to the LMA replaces the Newton Method by the addition of a damping term, $\theta\mathbf{I}$, where $\mathbf{I}$ is the identity matrix and θ is the damping factor:

$$\delta = (\mathbf{J}^T\mathbf{J} + \theta\mathbf{I})^{-1}J^T[\mathbf{y}^{(\mathbf{f})} - g(X,\beta)] \tag{3.17}$$

It can be seen that if θ is small, then the LMA would essentially be the Newton method, however, if θ is big, then the LMA would approximate the gradient descent method where the next step would be in the step of the biggest change in J. Marquardt's contribution to the LMA method is to replace $\mathbf{I}$ with $diag(\mathbf{J}^T\mathbf{J})$ in order to scale each component of the gradient according to the curvature of the function so that there is larger movement in the direction where the gradient is smaller:

$$\delta = [\mathbf{J}^T\mathbf{J} + \theta diag(\mathbf{J}^T\mathbf{J})]^{-1}J^T[\mathbf{y}^{(\mathbf{f})} - g(X,\beta)] \tag{3.18}$$

For each iteration, δ is solved and then added to β to be ready for the next iteration. When the value of δ becomes sufficiently small (as predetermined by the user), the method is deemed to have found a minimal solution. Although computationally intensive, nonlinear least squares can be used for parameter estimation in a broad range of nonlinear models.

3.6 Linear Least Squares Estimation

In the special case of Equation 3.10, when g is linearly dependent upon β, there is an exact solution using the linear least squares method. The relationship function g is linearly dependent upon the parameters $b_1 ... b_k$ and so the equation can then be rewritten in matrix form. The Linear Least Squares Method solves the matrix equation for the best β candidate that minimizes error ($\mathbf{e}$) between the observed value ($\mathbf{y^{(f)}}$) and the estimated value ($X\beta$). The least squares error is minimized as follows:

$$\begin{aligned}
\mathbf{e} &= \mathbf{y^{(f)}} - X\beta \\
\therefore \mathbf{e}^T\mathbf{e} &= (\mathbf{y^{(f)}} - X\beta)^T(\mathbf{y^{(f)}} - X\beta) \\
&= (\mathbf{y^{(f)}}^T - \beta^T X^T)(\mathbf{y^{(f)}} - X\beta) \\
&= \mathbf{y^{(f)}}^T(\mathbf{y^{(f)}} - X\beta) - \beta^T X^T(\mathbf{y^{(f)}} - X\beta) \\
&= \mathbf{y^{(f)}}^T\mathbf{y^{(f)}} - \mathbf{y^{(f)}}^T X\beta - \beta^T X^T\mathbf{y^{(f)}} + \beta^T X^T X\beta
\end{aligned} \tag{3.19}$$

The minimum error or least squares error occurs when $\frac{d\mathbf{e}^2}{d\beta^T} = 0$ and this is the value of β that is the most likely candidate for estimation. β is estimated as follows:

$$\frac{d\mathbf{e}^T\mathbf{e}}{d\beta^T} = -X^T\mathbf{y^{(f)}} + X^T X\beta = 0 \tag{3.20}$$

Moving $-X^T\mathbf{y^{(f)}}$ to the RHS:

$$\begin{aligned}
X^T X\beta &= X^T\mathbf{y^{(f)}} \\
\therefore\ \beta &= (X^T X)^{-1}X^T\mathbf{y^{(f)}}
\end{aligned} \tag{3.21}$$

As can been seen in Equation (3.21), the estimate for β using the linear least squares method has an exact solution and can be directly given from selected inputs (X) and the measured outputs ($\mathbf{y^{(f)}}$). Parameters (β) estimated using this method can be done on any input-output system, assuming system linearity. By expressing a system in the form given in Equation (3.11), the estimate is directly obtainable using Equation (3.21).

3.6.1 Linear Least Squares for fMRI (GLM)

Most analysis in fMRI and neuroimaging rely on linear least squares estimation. The most ubiquitous statistical model for analysis of neuroimaging data uses a linear model to test for region specific effects. This model is known as the General Linear Model or GLM. First proposed for function imaging studies by Friston et al. (1994), the GLM

is used to analyse every voxel using the linear least squares method so that effects of activation-inducing-stimuli on specific regions on the brain can be visualized as three-dimensional parameter maps instead of the raw four-dimensional signals.

The GLM is a statistical technique; physiological models of the data were, until recently largely ignored. However, the physiology-free analysis means that the GLM is very flexible and the technique can be applied to all fMRI-derived and PET-derived data. First developed for BOLD-fMRI, current analysis of ASL-fMRI data has also used this technique. X is known in GLM analysis as the 'design matrix' and is populated the designed stimulus/regressors to be tested. The number of columns of X determine the number of effects to be analysed and each column contains the input stimulus/regressors as a series in time. The GLM satisfies the simplest requirements of modelling: converting the observed signal into interpretable components such as effects of interest and measurement error, and then to make inferences for the significance of the anatomical region associated with the the components of interest.

The process for a GLM analysis can be seen in Figure 3.7. Once the design matrix (X) has been established, linear least squares estimation of time series data is done for each voxel of the image, solving for β across the entire image of the brain. A whole brain parameter map can be generated for each element $(b_1, ..., b_p)$ of β in order to determine areas of the brain that respond to the effects established using X. If for any region of the brain image showing $b_k, k \in \{1...p\}$ to be large, then it can be interpreted that a change in the column inputs $[u_i\ x_{ik}], k \in \{1...p-1\}, i \in 1...n)$ would result in a large change in the measured output ($\mathbf{y^{(f)}}$); the input greatly affects function in that particular region of the brain.

Before analysis, the stimulus patterns (columns of X) are usually convolved with a Gaussian, gamma or double gamma function that typifies a standard hemodynamic impulse response function (HRF) (Miller et al., 2001). Both BOLD-fMRI and ASL-fMRI use this convolution. Convolution with the HRF assumes that the output and input are coupled as a linear time-invariant system and the HRF is the output of the system when the dirac function (impulse) is fed into the input. The convolution process is not shown in Figure 3.7 but essentially provides smoother X inputs for the fit. The GLM is a statistical technique; it can be applied for use to generate parameter maps for any whole brain imaging study that has the form of Equation (3.11).

3.6.2 The OSORU Model

An extension of GLM was proposed by Harms and Melcher (2003) who implemented the GLM solution using a novel set of basis functions (OSORU or Onset Sustained

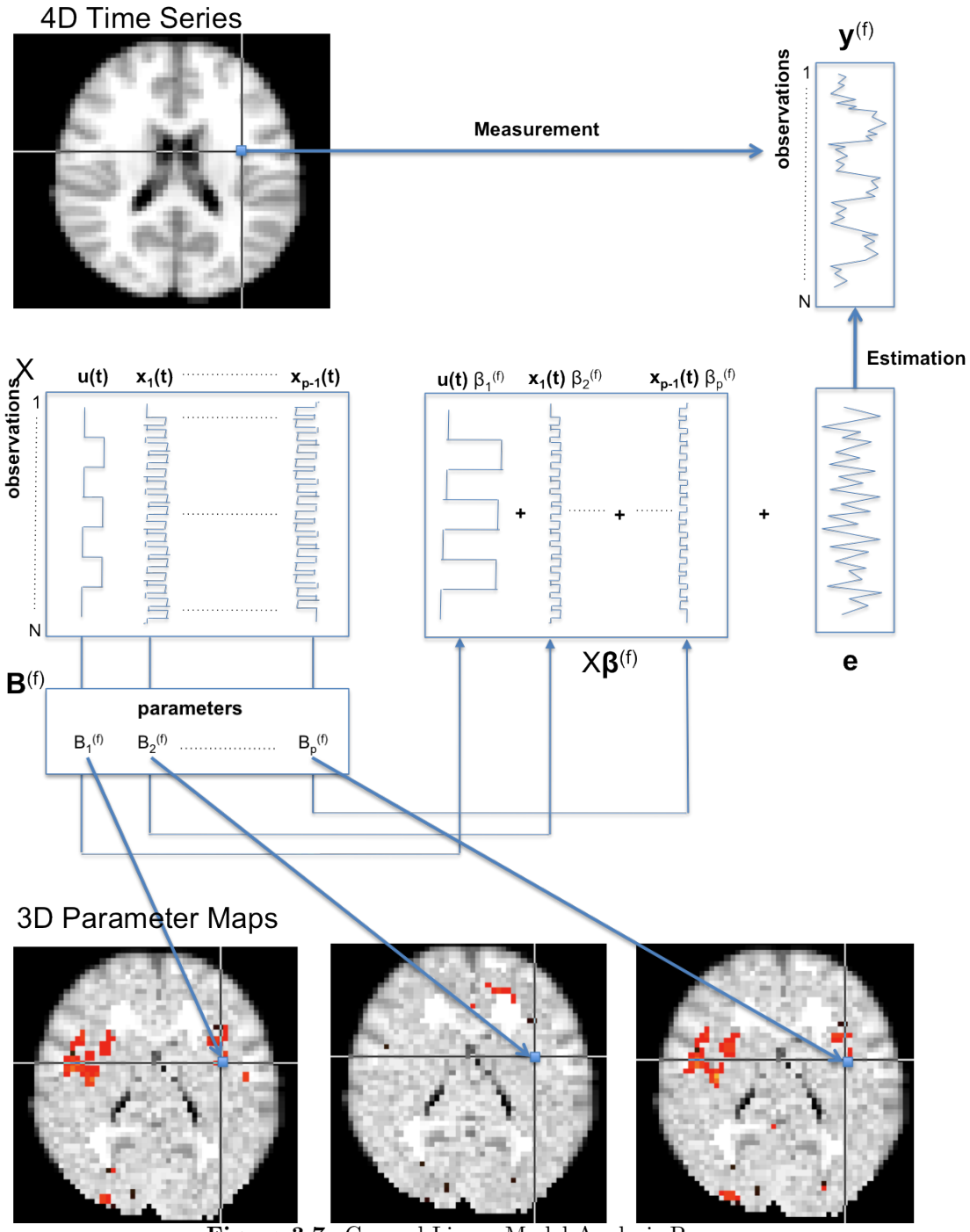

Figure 3.7: General Linear Model Analysis Process.

Offset Ramp Undershoot) chosen to reflect temporal features of cortical fMRI responses detected throughout the brain during an auditory task. Employing this model within the (GLM) framework, they quantified BOLD-fMRI response shapes across a number of tasks and subjects with more accuracy than the standard HRF response.

Recent studies investigating region- and task-specific signals have seen responses that cannot be fit by the standard HRF response model. Duff et al. (2007) employed the OSORU model for tracking signalling changes due to learning of a motor-sequence task as they found distinctive features in the BOLD-fMRI signal similar to those characterized by Harms and Melcher (2003). The OSORU model was extended with an additional undershoot component and the observed response shapes were characterized through whole-brain mapping of the OSORU components. Harms and Melcher (2003) and Duff et al. (2007) had the option to implement other methods that could be employed to map such dynamics including wavelet and harmonic decompositions, principle component analysis, and finite impulse response linear models. Both groups decided using the multi-component GLM approach as it is able to explicitly model specific waveform features. Furthermore, being a linear model, the GLM allows analysis procedures such as model-comparison and selection can be implemented and used for statistical interpretation. An example of the analysis can be seen in Figure 2.8 where each signal feature was analysed across the whole brain. The study indicates that GLM analysis with a standard HRF response may overlook important transient information that could potentially aid in analysis of more complex behaviour.

The GLM paradigm is very useful for determination of standard activation as a first order approximation of the response (Friston et al., 1998). However, being a linear time-invariant model, the GLM framework and expansions of GLM such as the OSORU method cannot model nonlinear coupling of hemodynamic responses. This limitation may ignore important behavioral aspects of the data that may be determined using nonlinear methods. Therefore, research has directed its attention into two major areas: 1) to find a better signal for the measurement of neuronal activity (presented in Section 2.3.1); and 2) to find ways to model the hemodynamic activity underlying the BOLD-fMRI signal (presented in Section 2.3.2). The severity of GLM's limitation is explored in the next chapter.

3.7 Model Selection Using AIC and BIC

When two or more models are proposed for the same set of data, the choice of model becomes very important. In choosing a statistical model, one has to make a choice

between simplicity and completeness. Simple models having fewer free parameters tend to be easier to understand and to calculate, but may not capture the conceptual picture of the system in which the data has been observed. Complicated models, with more parameters, tend to provide a richer knowledge of the underlying behaviour of the system and so may offer a better fit of the data, but they may be too complex, becoming difficult to calculate and overfit the data.

The Akaike Information Criterion (AIC) and the Bayesian Information Criterion (BIC) are two tools for model selection, offering a tradeoff between accuracy and complexity of a model (Akaike, 1974, 1979). Given any dataset, competing models maybe ranked according to their AIC/BIC score with the one having the lowest value being the best candidate model. In any model of reality, there is a discrepancy between the model and 'full reality' or the observations made of the system. This discrepancy can be quantified by the Kullback-Leiber Discrepancy (KLD), more generally used to determine the distance between two probability densities. Both AIC and BIC are applications for model evaluation based upon this measure.

In the case where $\mathbf{y}$ is generated from a source that has independent, normally distributed errors, the equations simplify to depend only on the number of samples n and the number of parameters p:

$$AIC(n,p) = n\log\left(\frac{S(\beta)}{n}\right) + 2p \tag{3.22}$$

$$BIC(n,p) = n\log\left(\frac{S(\beta)}{n}\right) + p\log(n) \tag{3.23}$$

$S(\beta)$ is the sum of squared error for the fitted model. It should be noted that the AIC or BIC scores of a single model are not important, nor are comparison of AIC and BIC scores of the same model. The scores have to be ranked between different models. AIC and BIC ultimately rate models given different penalty terms imposed. AIC imposes a strict $2p$ penalty for the number of parameters irrespective of the number of samples, whilst BIC imposes a $p\log(n)$ penalty that penalizes the number of parameters more with increasing number of samples.

3.8 Chapter Summary

This chapter presented the theory governing methods and algorithms used in investigation of the feasibility of using ASL-fMRI data as a better correlate for neuronal stimulus than BOLD-fMRI. Firstly, the general modelling and comparison framework was presented as well as a workflow of how models are compared to each other to determine

the best performing model. Secondly, model estimation and comparison was covered in more detail. The critical concept introduced was that of using least squares estimation to solve for model parmaters. Another concept was that of how to compare performance of models using the Information Criterion algorithms (AIC and BIC). These concepts and their associated equations are used extensively throughout the analysis as will be seen in the following two chapters. The two questions have been introducted at the beginning of the chapter: What type of dynamics are suitable for the modelling of ASL-fMRI data? Can transient features such as spiking and ramping, measured for CBF using other techniques also be found in ASL-fMRI data? These questions will be addressed through analyzing a combination of simulated and experimental data.

Chapter 4

Simulations

This chapter provides analysis of simulated CBF models described in Chapter 3. The simulations provide better understanding of the limits in which models are able to operate. They also facilitate model comparison, highlighting differences as well as similarities between the various CBF models. The aim is to determine the optimal CBF model suited for analysis of ASL-fMRI datasets. Simulations provide a standardized framework to facilitate model selection on a theoretical level.

The ASL-fMRI signal is a noisy and slowly-sampled signal. Since the models model framework presented in Table 3.2 are being used in estimation of the ASL-fMRI signal, the most important questions that are able to be answered through simulation are that of determining the optimal model to be used in such a noisy and slowly-sampled environment. Three questions are answered through simulation: 1) In which range of SNR/TR values does the estimation of dynamic model parameters (k, k_1 and k_2) become unnecessary? 2) In which range of SNR/TR values does the estimation of the transient parameters ϵ_1 and ϵ_4 become unnecessary? and 3) In which range of SNR/TR values does estimation with a lower order model yield better accuracy than a higher order model? By answering the three questions, it is possible to have a very good indication of the typical performance of each model for real data as well as to provide a guideline of additional improvements in measurement technology for inclusion of additional parameters for estimation.

Basic analysis techniques are first introduced and then slowly integrated into a larger analysis framework. Single estimations of model parameters were done repeatedly for each node of a SNR/TR grid. The estimation algorithms minimize the least squares error through linear or nonlinear least squares methods.The output of each grid were used to provide more insight into the problem. Various factors affecting estimation performance are explored. The modules used for analysis are presented in the earlier sections whilst

the actual analysis of where the three questions presented in the previous paragraph are answered in the latter sections 4.4, 4.5 and 4.6

4.1 Introduction to Simulations

Physical limitations of CBF Models defined in Table 3.2 were investigated through simulations. The simulation framework was constructed so that input stimuli of different length and duration could be generated. The paradigm of the pain dataset was matched through simulation so that generated signals were as closely matched to experimental data as possible. Linear least squares estimation was used to solve model parameters in most of the simulations. However, certain simulations required the use of nonlinear least squares as some parameters were exponentially correlated to the model function. The simulations were built up in a hierarchical manner, with the more complicated analysis done through combinations of simpler ones. The procedure, the results and the purpose of each simulation will be explained in greater detail through the following sections.

Modelling the CBF Response The input paradigm for simulations was matched with that of the experimental pain dataset described in more detail in Chapter 5. The total duration of the block is 78 seconds, there is a 12 second delay before the stimulus is switched on for 36 seconds. There is an off period of 30 seconds before the end of the block. The single block paradigm can be seen in Figure 4.1. This paradigm is used throughout the simulations as the input function.

A CBF response to the input paradigm (defined in Section 3.2) can be generated using the choice of the CBF model and the selection of parameters for the model. Examples of how parameter choice affect the generated response can be seen in Figure 4.2. In this example, the change in the CBF function in response to variations of single parameters were demonstrated for ϵ_1 to ϵ_4 for a given model and input function. More complicated responses can be obtained through combinations of parameter values. In this way, a variety of shapes can be generated to simulate the CBF response. In general, ϵ_1 governs the magnitude of the onset spike (Figure 4.2a), ϵ_2 governs the magnitude of the steady state response (Figure 4.2b), ϵ_3 governs the magnitude of the ramping response (Figure 4.2c) whilst ϵ_4 governs the magnitude of the offset spike (Figure 4.2d).

Figure 4.2 showes the variations of signal whilst changing the ϵ parameters (DTs). The model equation itself (DMs) can also be changed. In contrast to the DTs, the DMs define the smoothness of the CBF signal as well as the responsiveness of the signal to the input function. Figures 4.3 and 4.4 show the variety of CBF responses that can be generated.

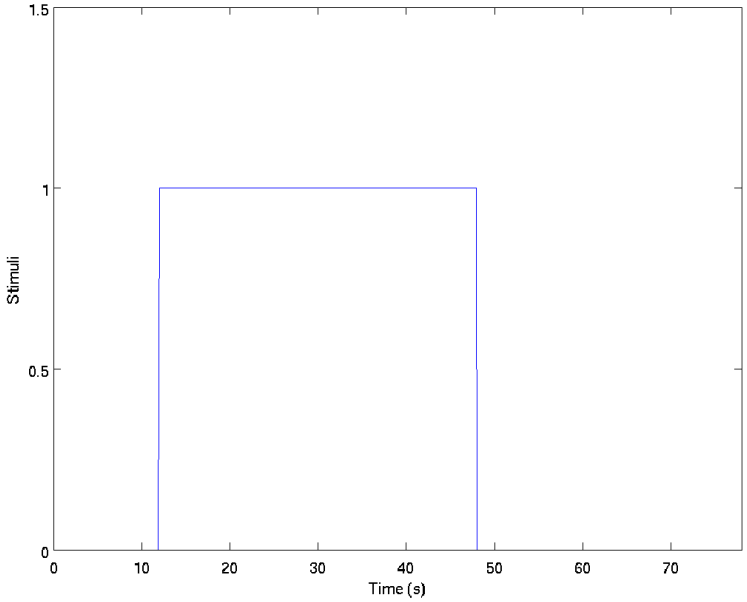

Figure 4.1: Input Stimulus for Simulation.

Figure 4.3 shows example responses generated using different DMs with the same DT. Figure 4.4 shows example responses generated using the same DM with different DTs. The parameters used in Figures 4.3 and 4.4 are shown in Tables 4.1 and 4.2 respectively.

	Driving Term	
	$\epsilon_1 \frac{d}{dt}u(t) + \epsilon_2 u(t) + \epsilon_3 \int u(t)\,dt,$	$0 < t < T_{ON}$
	$\epsilon_4 \frac{d}{dt}u(t),$	$t \geq T_{ON}$
	$\epsilon_1 = 1.0,\ \epsilon_2 = 0.4,\ \epsilon_3 = 0.02,\ \epsilon_4 = 0.5$	
	Dynamic Models	
A	$\frac{1}{k_2}\ddot{f}_n(t) + \frac{k_1}{k_2}\dot{f}_n(t) + [f_n(t) - 1],$	$k_1 = 2.0,\ k_2 = 1.09$
B	$\frac{1}{k_2}\ddot{f}_n(t) + \frac{k_1}{k_2}\dot{f}_n(t) + [f_n(t) - 1],$	$k_1 = 2.0,\ k_2 = 0.91$
C	$\frac{4}{k_1^2}\ddot{f}_n(t) + \frac{4}{k_1}\dot{f}_n(t) + [f_n(t) - 1],$	$k_1 = 2.0$
D	$\frac{1}{k}\dot{f}_n(t) + [f_n(t) - 1],$	$k = 1$
E	$f_n(t) - 1$	

Table 4.1: Equations and parameter settings for different DMs coupled with the same DT. Graphs of the functions are seen in Figure 4.3

4.1.1 Signal Generation

Example responses obtained using theoretical models are shown in Figures 4.3 and 4.4. The theoretical signals are all smooth and continuous. Experimental data however, is noisy and is discretely sampled. Additional steps were required to convert the smooth

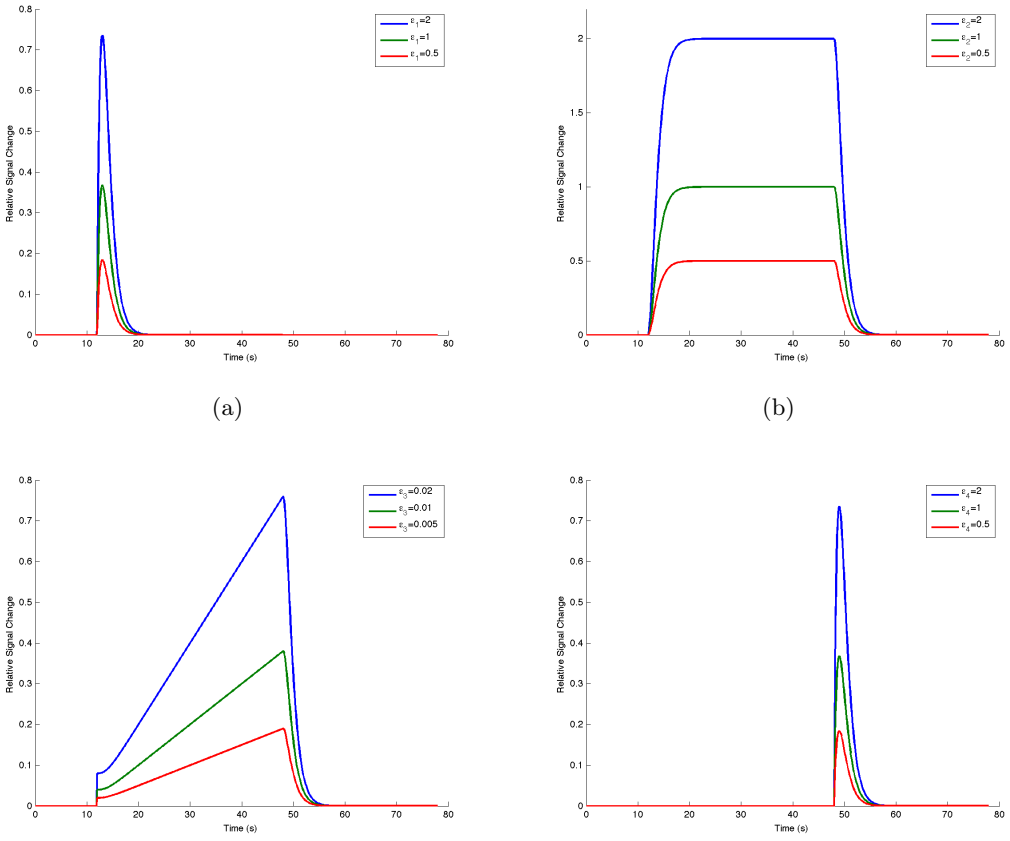

(a) (b)

(c) (d)

Figure 4.2: CBF response changes of Dynamic Model: $\frac{4}{k_1^2}\ddot{f}_n(t)+\frac{4}{k_1}\dot{f}_n(t)+[f_n(t)-1]$, $k_1 = 2.0$ to specific Driving Term parameters. a) Responses governed by parameter ϵ_1. b) Responses governed by parameter ϵ_2. c) Responses governed by parameter ϵ_3. d) Responses governed by parameter ϵ_4.

Dynamic Model $\frac{4}{k_1^2}\ddot{f}_n(t) + \frac{4}{k_1}\dot{f}_n(t) + [f_n(t) - 1],$ $k_1 = 2.0$	
Driving Term	
$\epsilon_1 \frac{d}{dt}u(t) + \epsilon_2 u(t) + \epsilon_3 \int u(t)\,dt,$	$0 < t < T_{ON}$
$\epsilon_4 \frac{d}{dt}u(t),$	$t \geq T_{ON}$
A	$\epsilon_1 = 5.0,\ \epsilon_2 = 0.4,\ \epsilon_3 = 0.02,\ \epsilon_4 = 3.0$
B	$\epsilon_1 = 3.0,\ \epsilon_2 = 1.0,\ \epsilon_3 = 0.02,\ \epsilon_4 = 1.0$
C	$\epsilon_1 = 0.5,\ \epsilon_2 = 0.8,\ \epsilon_3 = 0.02,\ \epsilon_4 = 0.0$
D	$\epsilon_1 = 0.5,\ \epsilon_2 = 0.7,\ \epsilon_3 = 0.00,\ \epsilon_4 = 0.0$
E	$\epsilon_1 = 0.0,\ \epsilon_2 = 1.0,\ \epsilon_3 = 0.02,\ \epsilon_4 = 0.0$

Table 4.2: Equations and parameter settings for the same DM coupled with different DTs. Graphs of the functions can be seen in Figure 4.4.

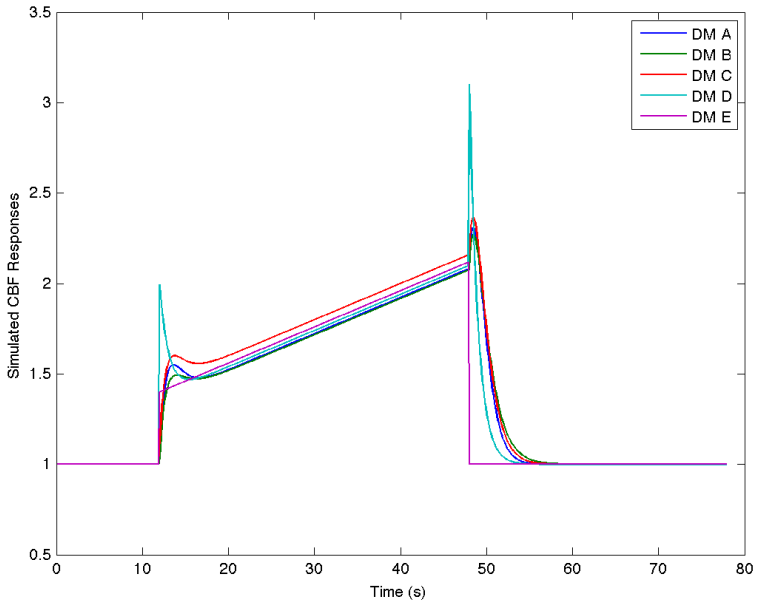

Figure 4.3: Simulated responses for different DM using the same DT. Systems A to E are examples of functions with various response speeds and transient features determined by the type of DM used. See Table 4.1 for more details.

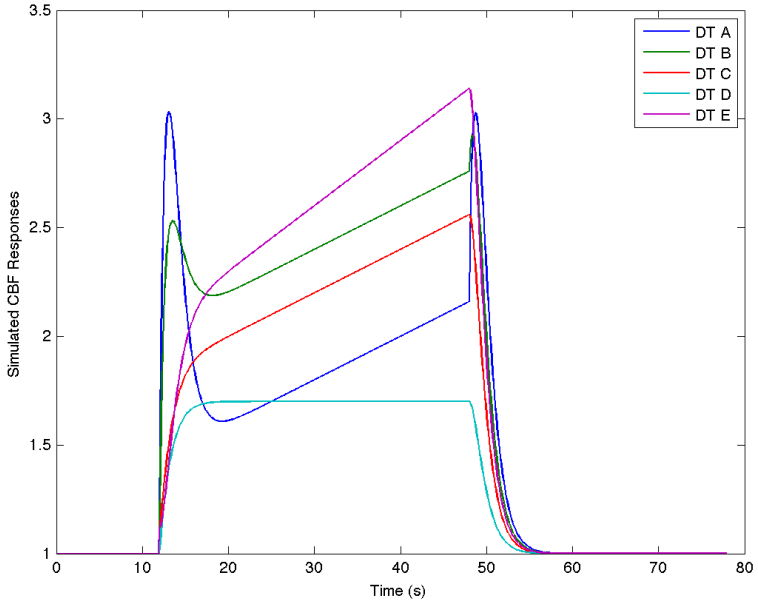

Figure 4.4: Simulated responses for different DTs using the same DM. The responses are more varied than Figure 4.3 due to the fact that the DT parameters (ϵ_1 to ϵ_4) contribute more prominently to the stationary features of the generated response (spikes, blocks, and ramps). See Table 4.2 for the list of curves generated.

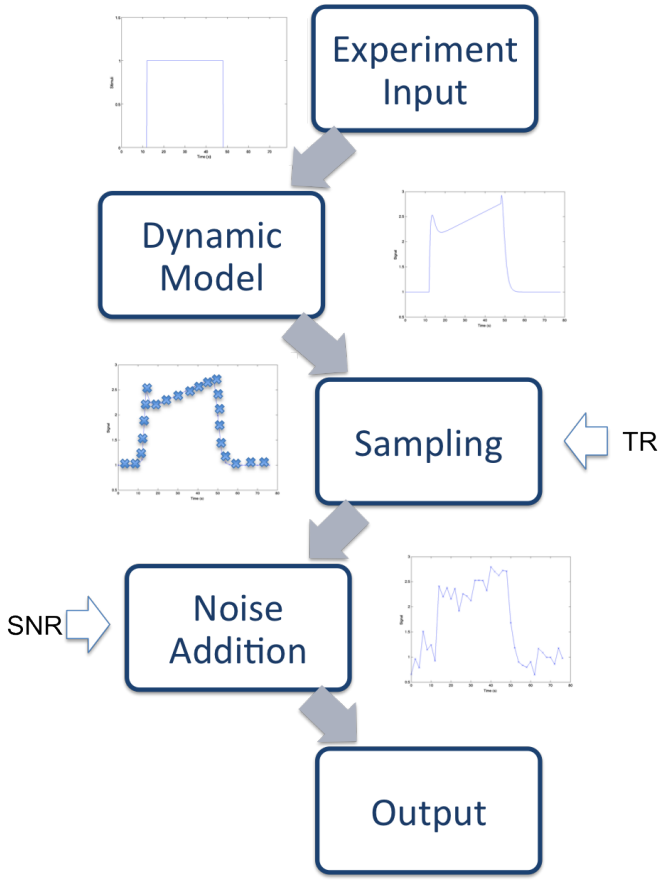

Figure 4.5: Signal generation workflow showing how a noisy signal is generated through the simulation process. TR and SNR can be varied for for flexibility in output.

signal into a simulated CBF response. The simulation framework was set up so that the signal to noise ratio (SNR) as well as the sampling time (TR) can be varied. Noise was assumed to be Gaussian for ease of calculation. Figure 4.5 show the steps involved in signal generation. Along with the ability to vary DT and DM, a wide selection of signals can be produced through simulation. The terminology used therein for simulation purposes refers to the model used to generate the underlying noiseless signal as the 'generating model'. The signal that is generated referred to as the 'noiseless signal' or the 'actual signal'. When noise is added to the noiseless signal, it is referred to as 'observed signal' or the 'noisy signal'.

4.2 Basic Modules for Comparing Estimation of the CBF Response

Once CBF signals can be simulated with control of noise (SNR) and sampling time (TR) through the different models, analysis can be done for the comparison of estimation mod-

els. The analysis of estimation models have been organized into a hierarchical manner for programming versatility. This was done for two critical factors required for model comparison: First, the analysis framework was required to compare and make sense of the large number of possible combinations of DMs and DTs for estimation. Second, the analysis framework was required to do comparisons of these estimation models over an even greater range of noise and sampling times. These two factors compound together to form a very large set of tests to perform. The goal of developing the analysis framework was firstly to package similar tests into modules and then to be able to reuse these modules to perform selective analysis that enables cross-sectional views across the set of all possible CBF estimation models and their performance across various SNR and TR values. In this chapter, modules are also known as blocks and the two terms will be used interchangeably. In addition to the terms defined for generated signals in Section 4.1.1, more terms are defined to distinguish between the signals that are generated from user-defined parameters and the signals that are generated from estimated parameters. The model that is used in the estimation algorithm is referred to as the 'estimation model'. The signal determined by the estimator as the best estimate of the true signal is referred to as the 'estimated signal'.

4.2.1 Single Instance Module

The Single Instance module forms the most basic analysis done for a given model and its parameter and provides a general summary that is used by most other subsequent modules. The Single Instance module allows the following question to be asked: If a signal is generated from a given CBF model with known input parameters, can the input parameters be accurately recovered through estimation?

The Single Instance module assumes that the generated signal uses the same model as the estimation. The estimated signal and model parameters for the estimation model are obtained by performing a single estimation of model parameters using the observed signal. The estimated parameters are then compared to the original parameters used to generate it. The system diagram and a thorough description of the module can be found in Figure 4.6. An example of such an analysis can be seen in Figure 4.7. Models A to D of Table 4.1 have been used to generate noisy signals with a SNR of 20.0 dB and a TR (repeat time or sampling time) of 0.5 seconds. The same models were then used to estimate DT and DM parameters which are then compared to the actual value.

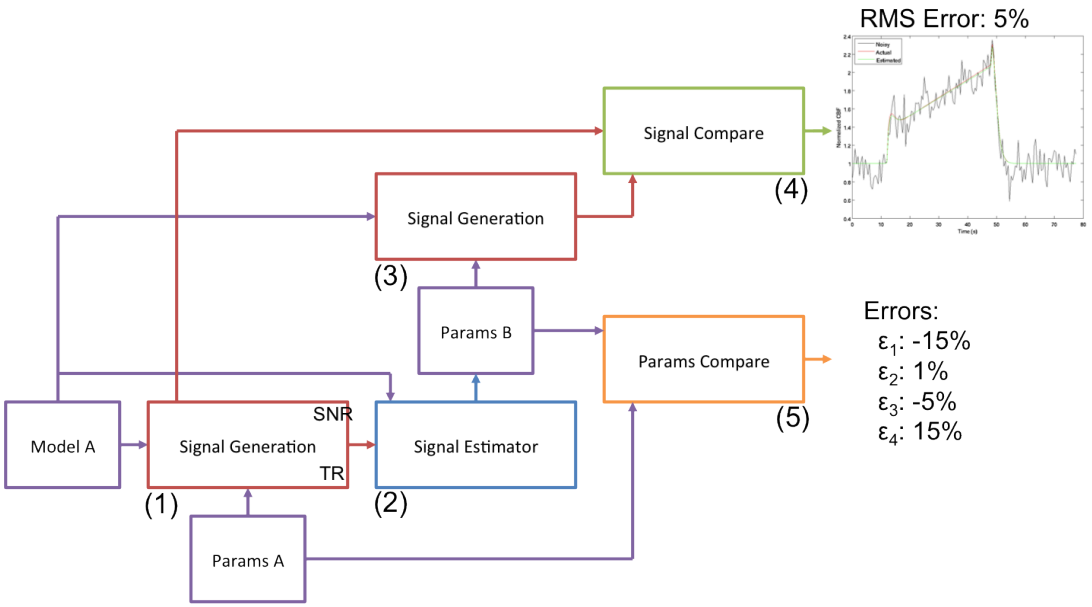

Figure 4.6: System diagram of a Single Instance module. The diagram of 'Signal Generation' blocks can be found in Figure 4.5. Steps are explained as follows: (1) The initial noisy signal is generated from one of the 'Signal Generation' blocks by taking in a model and the parameters for the model as input, as well as specified TR and SNR values to generate a noisy signal. (2) The 'Signal Estimator' block can be either a linear or nonlinear least squares solver depending upon the parameters required to be solved. The 'Signal Estimator' block takes in the model used by the 'Signal Generation' block, along with the noisy signal in order to generate an additional set of estimate parameters. (3) Using these estimated parameters, an estimated signal is generated. (4) (5) The estimated signal and estimated parameters are then compared to the original set of parameters and the signal that was generated to determine a set of statistics for the estimation. A set of sample estimates can be seen in Figure 4.7.

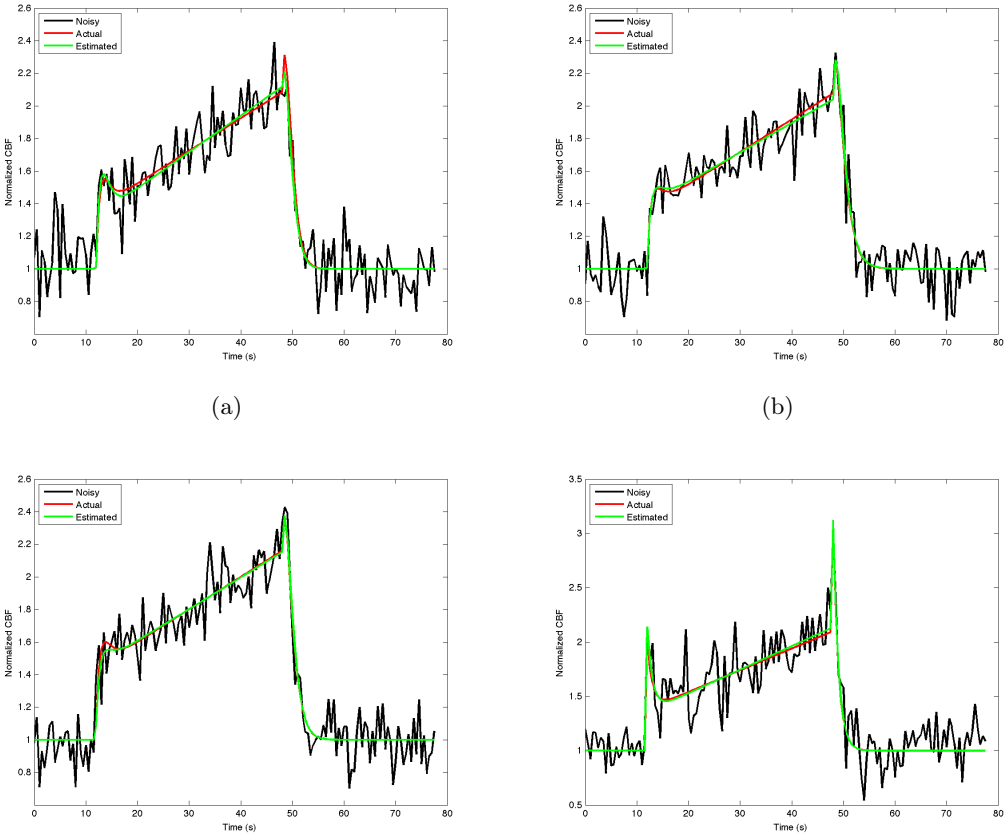

Figure 4.7: Estimates of parameters using the Single Instance module. The same model is used for signal generation as well as for estimation. Table 4.1 shows the model equations. a) Sample response and estimate for DM A. b) Sample response and estimate for DM B. c) Sample response and estimate for DM C. d) Sample response and estimate for DM D.

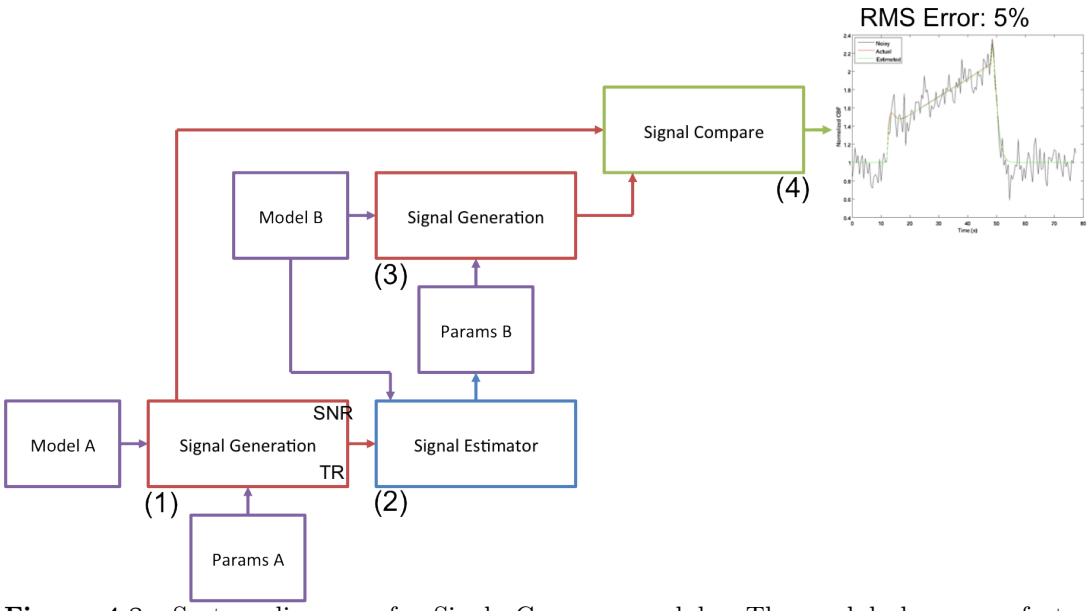

Figure 4.8: System diagram of a Single Compare module. The module has some features similar to the Single Instance module (Figure 4.6) with a few differences. Firstly, instead of one CBF model as input, two models are required (Models A and B). Secondly, no parameter comparison is done as input parameters are for Model A whilst the estimated parameters are for Model B. Steps are explained as follows: (1) A noisy signal is generated through 'Signal Generation' block with Model A and Params A as inputs. (2) The noisy signal is then used along with Model B to estimate Params B. (3) Model B and Params B are used to generate the estimated signal. (4) The RMS error between the noiseless signal and the estimated signal can be found. A normalized RMS error is calculated by diving the RMS error with the amplitude of the noiseless signal.

4.2.2 Single Compare Module

The Single Compare module is another foundation module but asking a different question to that of the Single Instance module. The Single Compare module asks: How accurately can one model be used to estimate the signal produced from a different model? This question is important as it compares the similarities between one model to the other. If signal estimation produces very close results, it suggests that the two models used for comparison are similar and may in fact be substituted for each other. The block diagram and description of the module can be seen in Figure 4.8. An example of such an analysis can be seen in Figure 4.9. The generating model is Model A of Table 4.1. It has been used to generate noisy signals with a SNR of 20.0 dB and a TR of 0.5 seconds. The estimation models are models A to D of the same table.

4.2.3 Multiple Instance Module

Following the definition of the Single Instance module, a Multiple Instance module is defined. The Single Instance module is used inside a Multiple Instance module to itera-

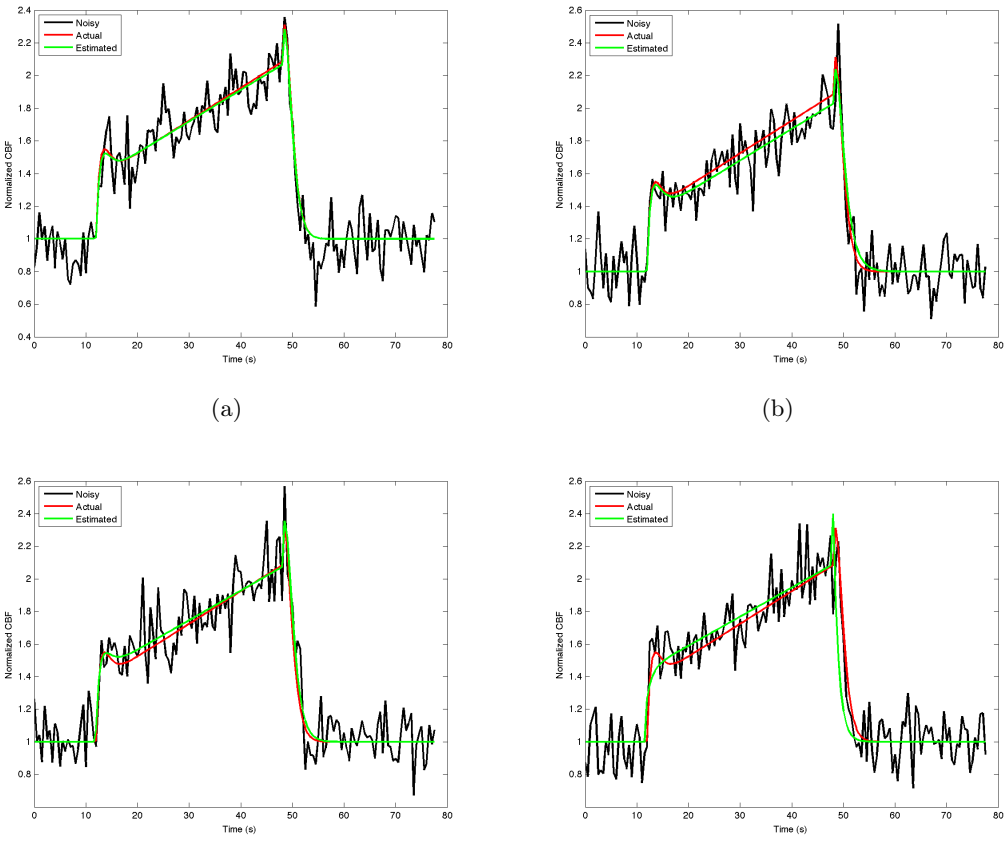

Figure 4.9: Estimates of parameters using the Single Compare module. Generation of signal was done using DM A of Table 4.1 and estimation of model parameters were done through various estimation models. See Table 4.1 for the model equations. a) Sample estimation of generated DM A response using DM A estimator. b) Sample estimation of generated DM A response using DM B estimator. c) Sample estimation of generated DM A response using DM C estimator. d) Sample estimation of generated DM A response using DM D estimator.

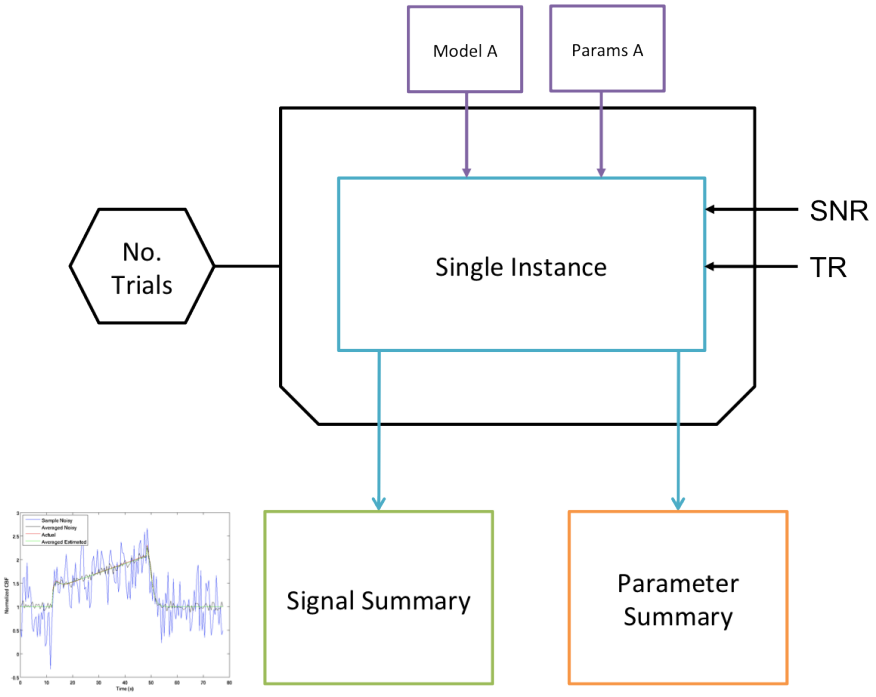

Figure 4.10: System diagram of the Multiple Instance module. The inputs to the module are the number of trials, a model and its parameter inputs as well as particular SNR and TR values. The module takes all the inputs and uses the Single Instance block (details shown in Figure 4.6) iterates over the number of trials specified such that a summary of the outputs are generated. The bias and variance of parameter values as well as signal estimation can be determined. Examples are shown in 4.11 with the summary statistics of the analysis shown in Table 4.3.

tively generate a set of statistics summarizing the bias and variance of the estimator at predetermined SNR and TR values. Figure 4.11 show the block diagram and description of such a setup. Figure 4.11 show results of parameter estimation for the same models in Figure 4.7 using a SNR of 10.0 dB, a TR (repeat time or sampling time) of 0.5 seconds and 50 repeats. Table 4.3 summarizes the statistics of each estimation model shown in Figure 4.11. Note that the normalized standard error (NSE) instead of the standard deviation (SD) is given. The NSE is the standard error divided by the actual parameter value and is used to compare effectiveness of estimation between each of the parameters. The RMS error of the estimated signal compared to that of the noiseless signal was also calculated. The normalized RMS error (NRE), or the RMS error divided by the amplitude of the noiseless signal was also calculated and used to compare between models.

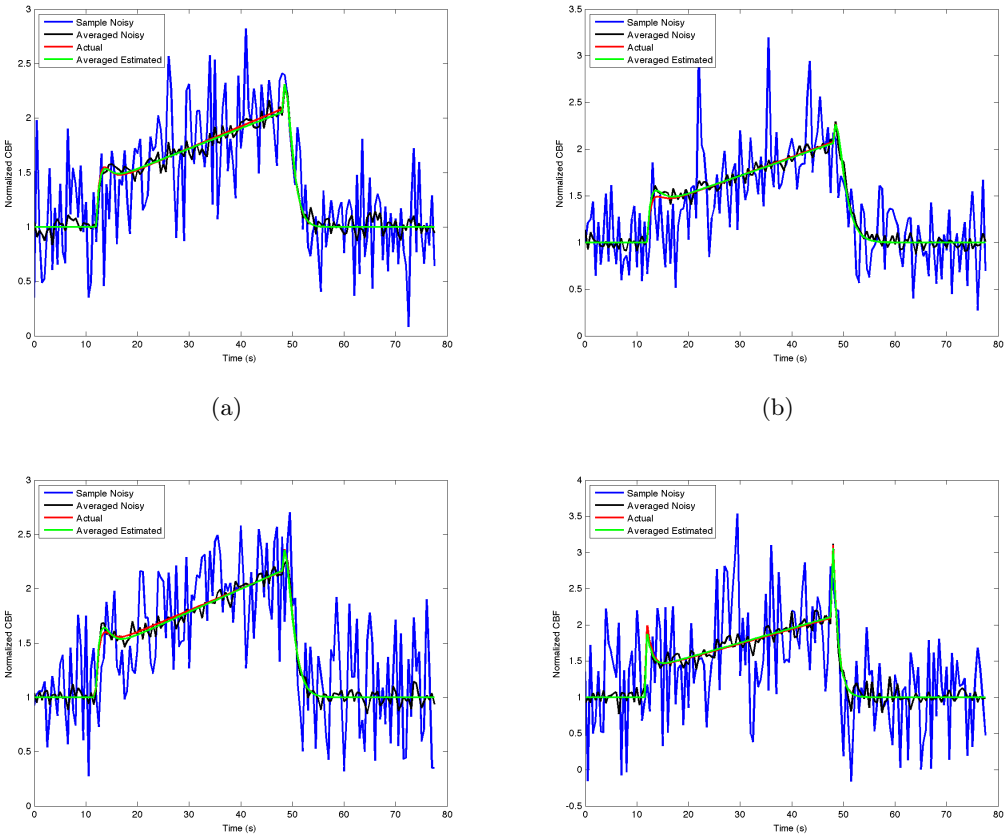

Figure 4.11: Summary of results using Multiple Instance module. Multiple estimates using the same model for signal generation and estimation. Additional inputs specified are SNR of 10.0, a TR of 0.5 seconds and 50 trials. See Table 4.1 for the model equations. a) Summary of DM A multiple estimation. b) Summary of DM B multiple estimation. c) Summary of DM C multiple estimation. d) Summary of DM D multiple estimation. Each of the sub-figures show four signals: 'Sample Noisy' is a sample of the noisy signal that was generated during the analysis process. 'Average Noisy' is the average of all the noisy signals that was generated. 'Actual' is the noiseless signal generated. 'Averaged Estimated' is the estimated signal generated using the mean values of all parameter estimates.

	Actual	DM A	DM B	DM C	DM D
ϵ_1	1.0				
estimate		0.9	1.1	1.3	0.85
bias		−10%	14%	27%	−15%
NSE		7.6%	7.8%	8.3%	8.4%
ϵ_2	0.4				
estimate		0.42	0.41	0.37	0.40
bias		−4.8%	3.2%	−8.1%	0.63%
NSE		3.5%	2.7%	4.5%	5.4%
ϵ_3	0.02				
estimate		0.019	0.019	0.021	0.021
bias		−7.2%	−4.2%	4.11%	2.5%
NSE		3.7%	2.6%	3.7%	5.1%
ϵ_4	0.5				
estimate		0.55	0.50	0.49	0.43
bias		13%	0.17%	−2%	−15%
NSE		8.4%	8.6%	9.8%	7.4%
Signal					
RMS error		0.0585	0.0539	0.0654	0.09
NRS		4.5%	4.2%	4.8%	7.2%

Table 4.3: Statistics of Multiple Instance module estimations for Figure 4.11.

4.2.4 Multiple Compare Module

Similar to the Multiple Instance module, the Multiple Compare module takes the Single Compare module and recursively generates a set of statistics summarizing the closeness of fit for two different models. Figure 4.12 show the block diagram and description of such a setup. Figure 4.13 show results of parameter estimation for the same models in Figure 4.9 using a SNR of 10.0 dB, a TR (repeat time or sampling time) of 0.5 seconds and 50 repeats.

	DM A	DM B	DM C	DM D
RMS error	0.0659	0.0667	0.0827	0.161
NRS	4.8%	4.8%	6.0%	12%

Table 4.4: Statistics of Multiple Compare module estimations for Figure 4.13.

4.3 Model Characterization through SNR/TR Profiles

Although models may give accurate estimates at high SNR and fast TR (seen in Figures 4.11 and 4.13), this may not be the case when SNR is lowered and/or TR is slowed. Therefore, the effectiveness of a model requires that its performance can be maintained

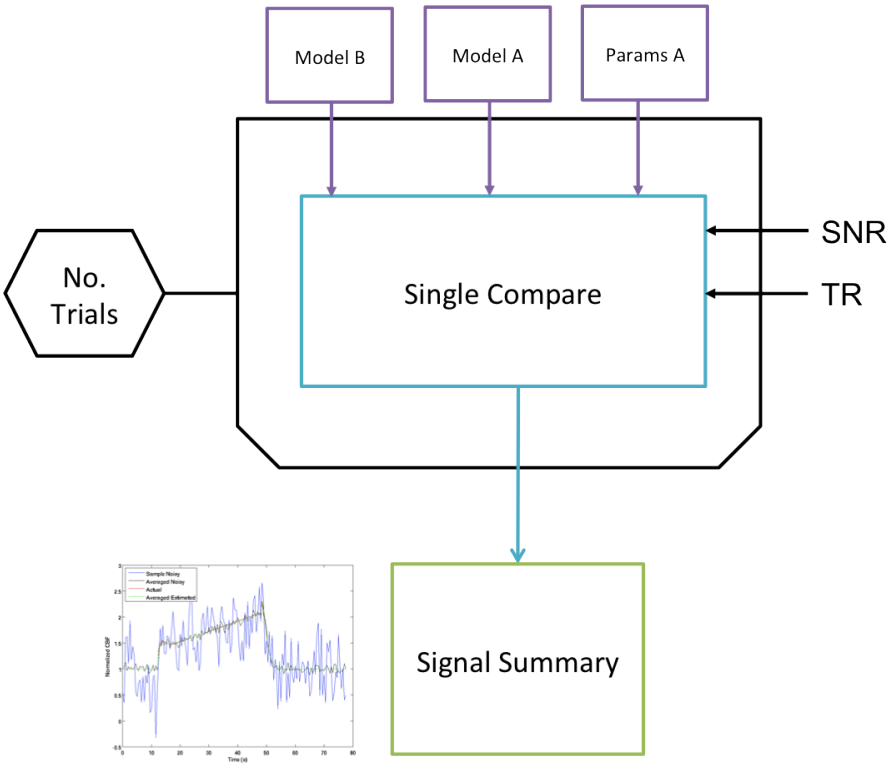

Figure 4.12: System diagram of the Multiple Compare module. The inputs to the module are the number of trials, a model and its parameter inputs, a comparison model as well as particular SNR and TR values. The module takes all the inputs and uses the Single Compare block (details shown in Figure 4.8) iterates over the number of trials specified such that a summary of the outputs are generated. The bias and variance of signal estimation can then be determined. Examples are shown in 4.13 with the summary statistics of the analysis shown in Table 4.4.

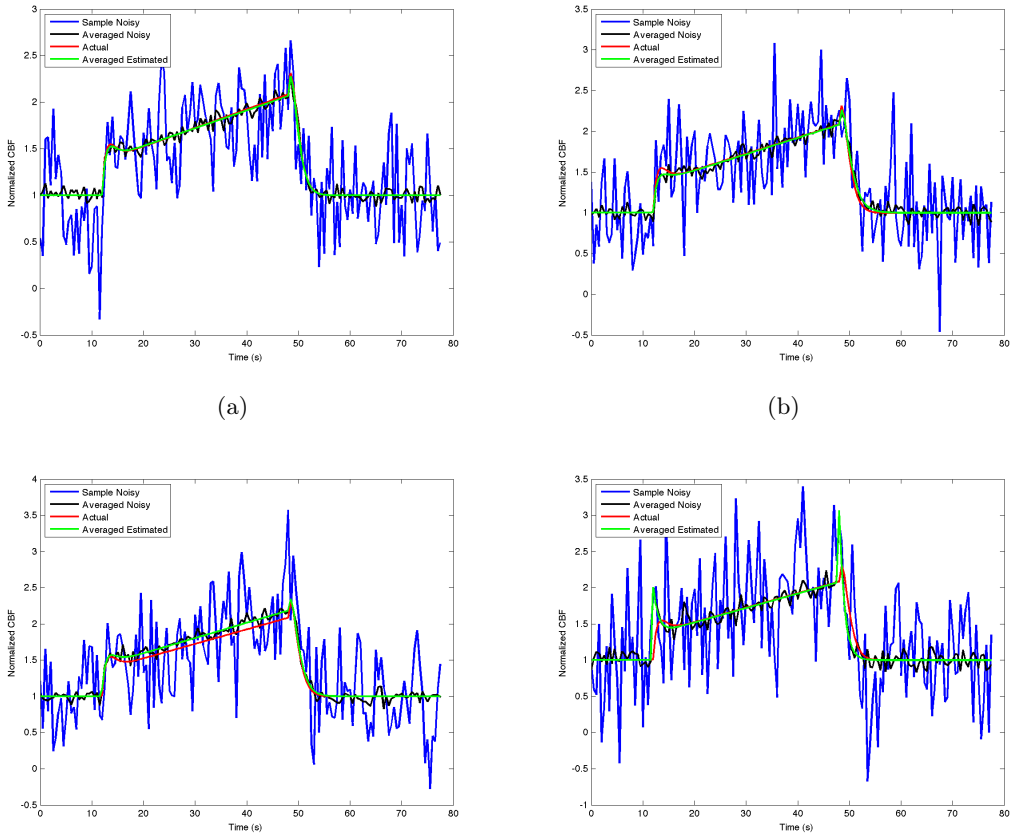

Figure 4.13: Generation of results using Multiple Compare module. Signal was generated using DM A of Table 4.1 and multiple signal estimates were done through various estimation models. Inputs specified have SNR of 10.0, a TR of 0.5 seconds and 50 trials. See Table 4.1 for the model equations. a) Sample estimation of generated DM A response using DM A estimator. b) Sample estimation of generated DM A response using DM B estimator. c) Sample estimation of generated DM A response using DM C estimator. d) Sample estimation of generated DM A response using DM D estimator. Each of the sub-figures show four signals: 'Sample Noisy' is a sample of the noisy signal that was generated using the generating model. 'Average Noisy' is the average of all the noisy signals that was generated. 'Actual' is the underlying noiseless signal. 'Averaged Estimated' is the estimated signal generated using the mean values of all parameter estimates of the estimation model.

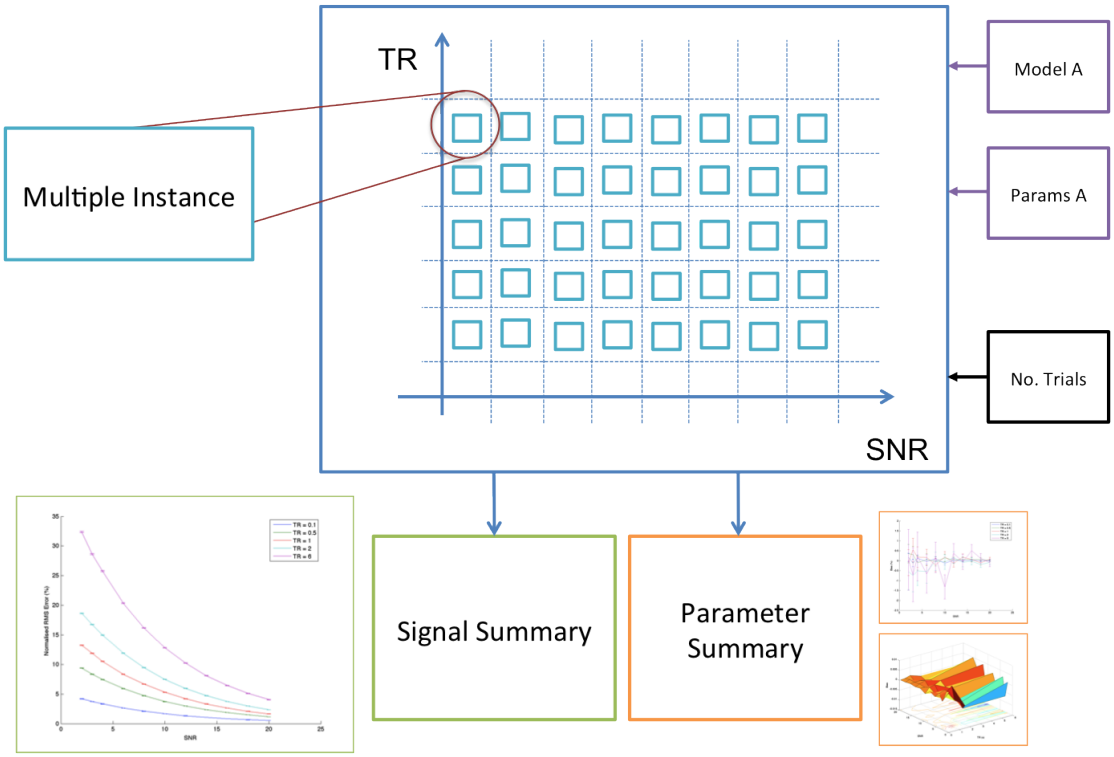

Figure 4.14: Block diagram of the Grided Multiple Instance module. The module input takes in a user specified model and its parameter input and also the number of trials to be performed. Each node of the grid is a Multiple Instance module (for more details see Figure 4.14) and each type of statistics generated by the each nodes are then stored within the grid for display purposes. Each row of the statistics seen in Table **??** can be visualized in a grid form, making this module an extremely useful tool for profiling models.

across all ranges of SNR and TR values. It was found through experience that any estimation model is most effectively categorized through building a profile of model effectiveness across a range of SNR and TR values. Thus, two types of grid analysis were introduced - The Grided Multiple Instance Module and the Grided Multiple Compare Module.

4.3.1 Grided Multiple Instance Module

The Grided Multiple Instance module provides visualization of all statistics generated by the Multiple Instance module over a range of SNR and TR values. This is a very effective tool for understanding how estimation of signal and model parameters are affected through noise and sampling time. These generated profiles are incredibly useful in choosing the right model for a given application as well as understanding where estimation may start to break down within a model. The block diagram of the module and its description can be seen in Figure 4.14.

Using the module, an SNR/TR profile can be constructed for any given CBF model.

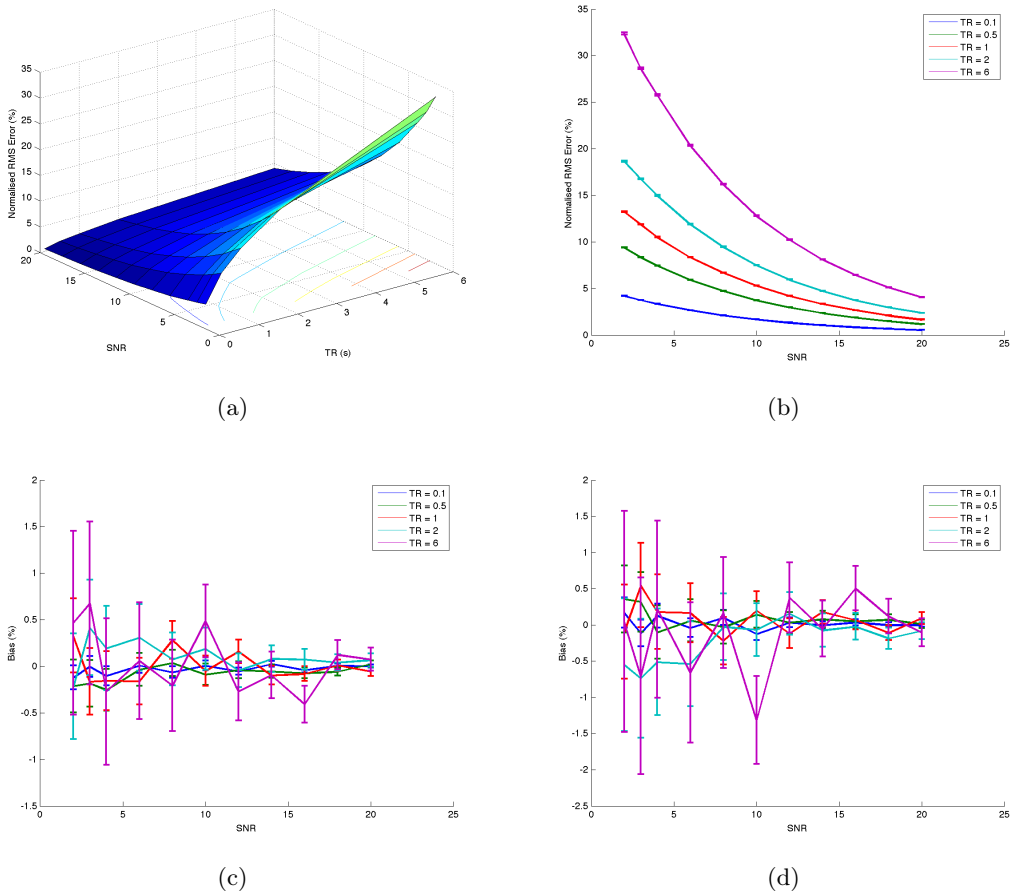

(a) (b)

(c) (d)

Figure 4.15: Example of results generated using the Grided Multiple Instance module. SNR/TR profile of ϵ_2 and ϵ_3 estimates for model E in Table 4.2 using 5000 trials per SNR/TR node. a) 3D Mean Signal Estimation RMS Error Profile. b) Cross-section of the RMS Profile along selected TRs with standard error bars showing variability in estimation of signal. c) Bias of estimation of parameter ϵ_2 with standard error bars. The plot shows more estimation variability at high TR (TR=6.0) compared to lower TR values (TR=0.1). d) Bias of estimation of parameter ϵ_3 with standard error bars. The plot shows the same effect as in Figure 4.15c.

This is done by specifying a SNR and TR grid and performing a multi-signal estimation on each of the nodes of the grid. Parameter estimates for same generating model as the estimation model can be visualized as a 3D plot or a series of 2D plots. Figure 4.15 shows the profile of Model E in Table 4.1, estimating parameters ϵ_2 and ϵ_3 using 5000 trials per node. Figure 4.15a shows the mean RMS error in a mesh form across all values of SNR and TR. Figure 4.15b shows the same plot with error bars, picking out selected TR to plot cross-sections of the mesh. Figures 4.15c and Figure 4.15d show bias of estimation for ϵ_2 and ϵ_3 respectively. It can be seen that in this particular case, the parameter estimates have a bias of 0 and low standard error at short TRs, when TR increases, the standard error also increases.

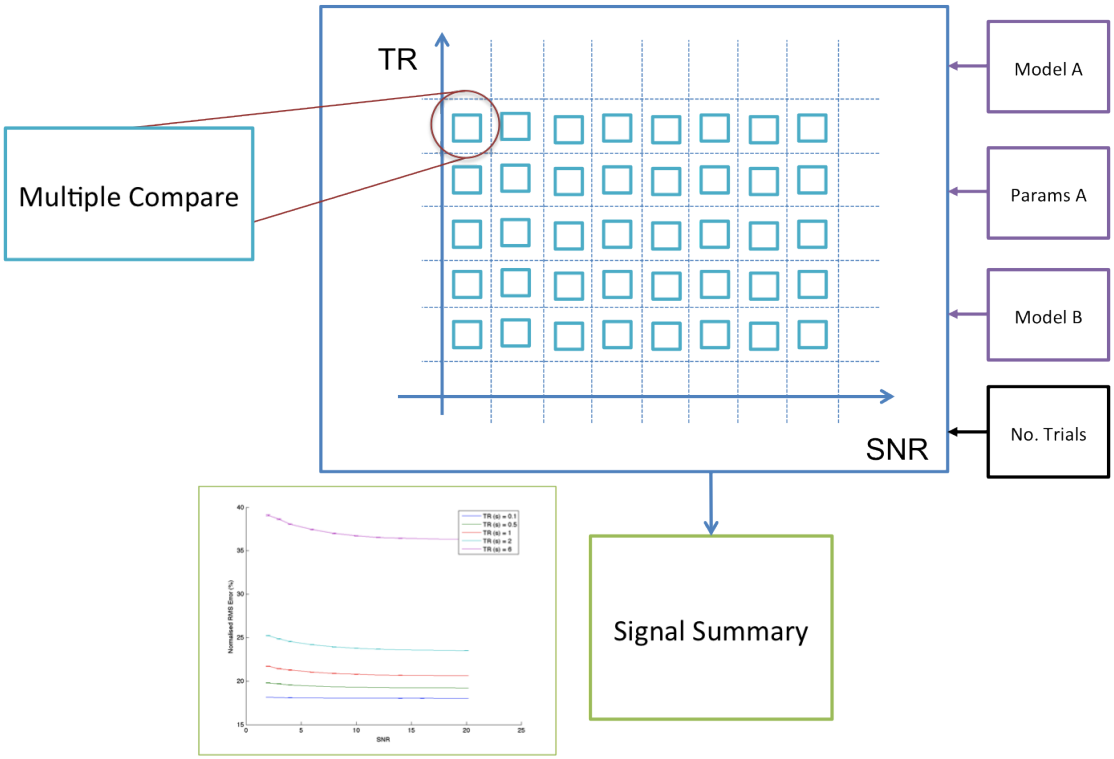

Figure 4.16: Block diagram of the Grided Multiple Compare module. The analysis is again set up in a grid with each node being a Multi Compare Module. Two input models are compared against each other for closeness of fit across a specified TR/SNR profile. The RMS error or error in estimation of the signal can be visualized in a grid form.

4.3.2 Grided Multiple Compare Module

Following on from the Grided Multiple Instance module, the same SNR/TR grid concept was applied to the Multiple Compare module in order to build the Grided Multiple Compare module. The block diagram of the module and its description can be seen in Figure 4.16. The figure is very similar in concept to that seen in Figure 4.14 with the main purpose of the module being that of compiling a profile of how one model can effective model another through different SNR and TR values. The module accepts as input two models - a signal generating model (Model A) and a signal estimation model (Model B) - and builds an estimation profile across different SNR and TR values for comparing closeness of model fits. Figure 4.17 shows two such profiles. In both profiles, the generating model has second order dynamics, whilst the two estimation models are of first order and a zeroth order respectively. This module has uses in determining whether estimation can be simplified. An example of this would be the question: Instead of using a 2nd order model for estimation of a noisy and discretely sampled signal, would a 1st order model or even a 0th order model be sufficient?

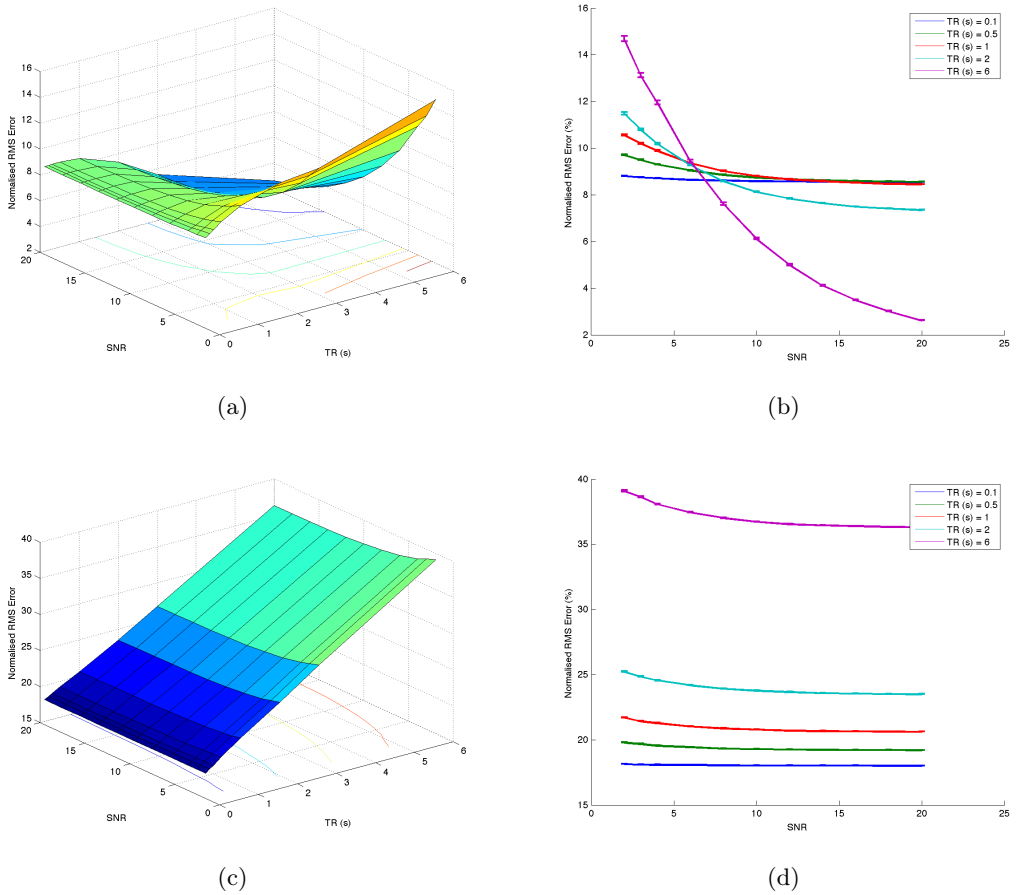

(a) (b)

(c) (d)

Figure 4.17: Example of results generated using the Grided Multiple Compare module. SNR/TR profile of various estimation models for the generating model E in Table 4.1. a) and b) show the 3D Normalized RMS Error Profile as well as selected cross-sectional plots of estimation using a 1st Order system. c) and d) show the 3D Normalized RMS Error Profile as well as selected cross-sectional plots of estimation using a 0th Order system.

4.4 Analysis 1 - Estimation Bias of DM Parameters

The Grided Multiple Instance and Grided Multiple Compare modules provide visualizations for model characterization and model comparison. The through a SNR/TR Profile the two modules effectively answers the second critical factor raised in Section 4.2 - How to do comparisons of estimation models over a range of noise and sampling times? The first factor is a more difficult question - How to make sense of the large number of possible combinations of DMs and DTs for estimation? Because of the endless amount of model possibilities, this question has to be answered in a more heuristic manner. The first question calls for examination of the proposed models - are there any extra parameters that can be ignored in the course of estimation? By eliminating parameters, choosing an effective model becomes much simpler.

The first analysis looks at the effectiveness of estimating parameters within the DMs. Grid analysis was done on 5 differing CBF systems in order to determine whether estimation of DM coefficients could results in a better fit of the CBF response across a range of TR and SNR values. The five systems were chosen to provide a variety of DM properties over 1st and 2nd order behaviour. The five systems that were chosen can be seen in Table 4.5:

	Driving Term	
	$\epsilon_1 \frac{d}{dt}u(t) + \epsilon_2 u(t) + \epsilon_3 \int u(t)\,dt, \quad 0 < t < T_{ON}$ $\epsilon_4 \frac{d}{dt}u(t), \qquad t \geq T_{ON}$ $\epsilon_1 = 0,\ \epsilon_2 = 0.4,\ \epsilon_3 = 0,\ \epsilon_4 = 0$	
	Dynamic Models	
A_1	Oscillating 2nd Order System	$\frac{1}{k_2}\ddot{f}_n(t) + \frac{k_1}{k_2}\dot{f}_n(t) + [f_n(t) - 1]$, $k_1 = 2, k_2 = 5$
A_2	Overdamped 2nd Order System	$\frac{1}{k_2}\ddot{f}_n(t) + \frac{k_1}{k_2}\dot{f}_n(t) + [f_n(t) - 1]$, $k_1 = 2, k_2 = 0.75$
A_3	Critically Damped 2nd Order System	$\frac{4}{k_1^2}\ddot{f}_n(t) + \frac{4}{k_1}\dot{f}_n(t) + [f_n(t) - 1]$, $k_1 = 2$
A_4	Fast 1st Order System	$\frac{1}{k}\dot{f}_n(t) + [f_n(t) - 1]$, $k = 5$
A_5	Slow 1st Order System	$\frac{1}{k}\dot{f}_n(t) + [f_n(t) - 1]$, $k = 0.5$

Table 4.5: DT and DM values for determination of SNR/TR profiles for Analysis 1.

Each DM equation was coupled with the same DT equation with parameters set as $\epsilon_1 = 0$, $\epsilon_2 = 0.4$, $\epsilon_3 = 0$, $\epsilon_4 = 0$. The equation has only ϵ_2 active as experience found that there was significant interference of estimation between ϵ_1, ϵ_4 and the DM coefficients. It was very difficult to estimate both of them together at the same time. For each system, two grid analysis was done - one using linear least squares solving for just ϵ_2, the other using nonlinear least squares solving for ϵ_2 as well as the DM coefficients (k_1 and k_2 for A

and B, k_1 for C, k for D and E). Summary of all trials were displayed as an SNR/TR profile with comparison of the nonlinear estimation with that of the linear estimate. Furthermore, a grided summary of the estimated DM coefficients (nonlinear estimation only) was also viewed to determine the effectiveness of estimation.

2nd Order Systems - Models A_1, A_2 and A_3 Results of the 2nd order systems can be seen in Figures 4.18, 4.19 and 4.20 - these three profiles are representative of different types of 2nd order systems used for modelling purposes.

Model A_1 - Figure 4.18a shows signal estimation error of the oscillating 2nd order system using the nonlinear least squares method. Parameters ϵ_2, k_1, and k_2 where variables to be estimated. In comparison, Figure 4.18b shows signal estimation error of the same system using linear least squares. Only ϵ_2 was the only free parameter in the second case. It can be seen from the comparison of the two figures that nonlinear estimation of signal was close to the optimal case where both k_1 and k_2 were known. However, estimation of k_1 and k_2 parameters - seen respectively in Figures 4.18c and 4.18d are not very ideal. In fact, there is alot of bias within estimation. Both DM parameters had significant bias within all SNR/TR combinations except for TR=0.1s and SNR>15 dB. It is interesting to note that k_1 and k_2 were most biased when TR=1.0s as this corresponds directly with the oscillation period of the signal. Furthermore, noise had a big effect in biasing of the signal at the typical TR=6.0s expected of ASL-fMRI datasets; there was still a bias of 20000% in estimation of k_1 and 5000% in the estimation of k_2 at SNR=20dB, the highest SNR profiled. Because of the enormous bias, it can be interpreted from the result that parameters k_1 and k_2 have minimal effect on the model at high TRs for the oscillating 2nd order model.

Model A_2 - Figures 4.19a and 4.19b show the comparative signal estimation error between nonlinear and linear least squares estimation respectively. As can be seen in Figure 4.19a, the nonlinear least squares being only able to find a local minimum, was not robust enough at low SNR and long TRs. Furthermore, estimation of DM parameters proved even more difficult with the underdamped model than the oscillatory model as parameter estimates had more biasing problems as can be seen in Figures 4.19c and 4.19d. This result matches to intuition as underdamped systems typically do not have the same amount of features as that of oscillating systems so that DM parameters have even less influence upon the model.

Model A_3 - In the critically damped case, there is only one DM parameter for estimation and so it is expected that there will be less bias for estimation of k_1 than in the previous two cases. Figures 4.20a and 4.20b show that nonlinear estimation was only slightly less

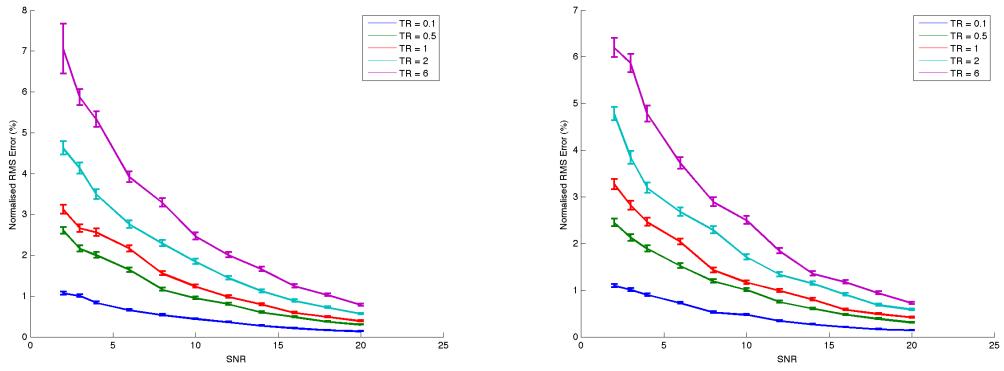

(a)

(b)

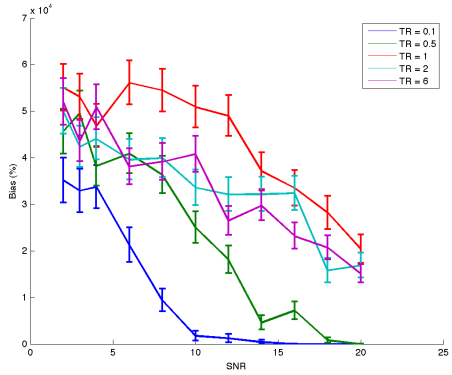

(c)

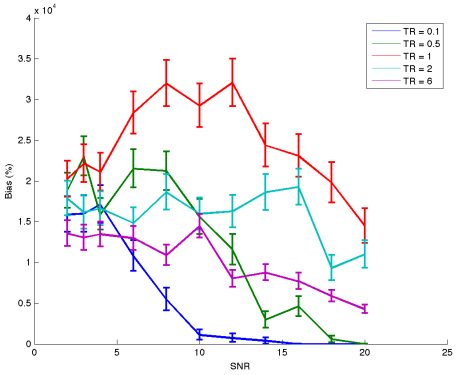

(d)

Figure 4.18: Results of Analysis for Model A_1, an oscillating 2nd order system of equation $\frac{1}{k_2}\ddot{f}_n(t) + \frac{k_1}{k_2}\dot{f}_n(t) + [f_n(t) - 1]$, $k_1 = 2, k_2 = 5.0$. a) Profile of RMS signal error using nonlinear least squares estimation and 3 free parameters (ϵ_2, k_1, and k_2). b) Profile of RMS signal error using linear least squares estimation and 1 free parameter (ϵ_2). c) Profile of bias in estimation of k_1. d) Profile of bias in estimation of k_2.

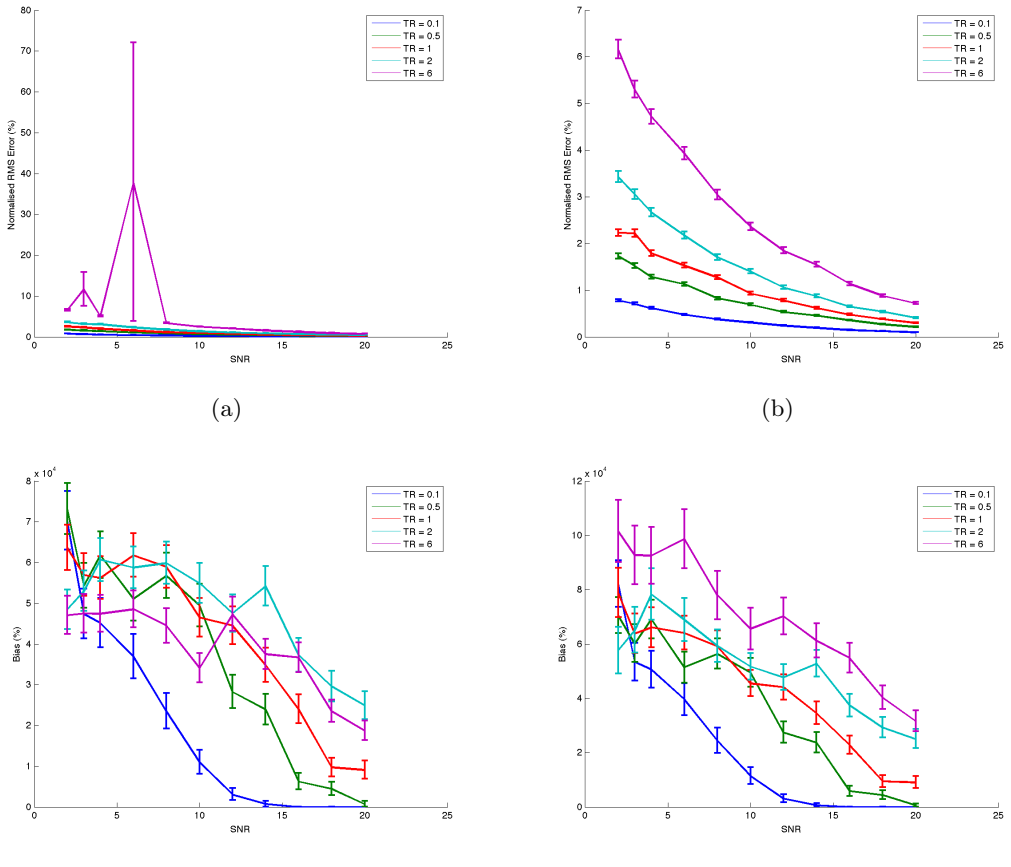

Figure 4.19: Results of Analysis for Model A_2, an overdamped 2nd order system of equation $\frac{1}{k_2}\ddot{f}_n(t) + \frac{k_1}{k_2}\dot{f}_n(t) + [f_n(t) - 1]$, $k_1 = 2, k_2 = 0.75$. a) Profile of RMS signal error using nonlinear least squares estimation and 3 free parameters (ϵ_2, k_1, and k_2). b) Profile of RMS signal error using linear least squares estimation and 1 free parameter (ϵ_2). c) Profile of bias in estimation of k_1. d) Profile of bias in estimation of k_2.

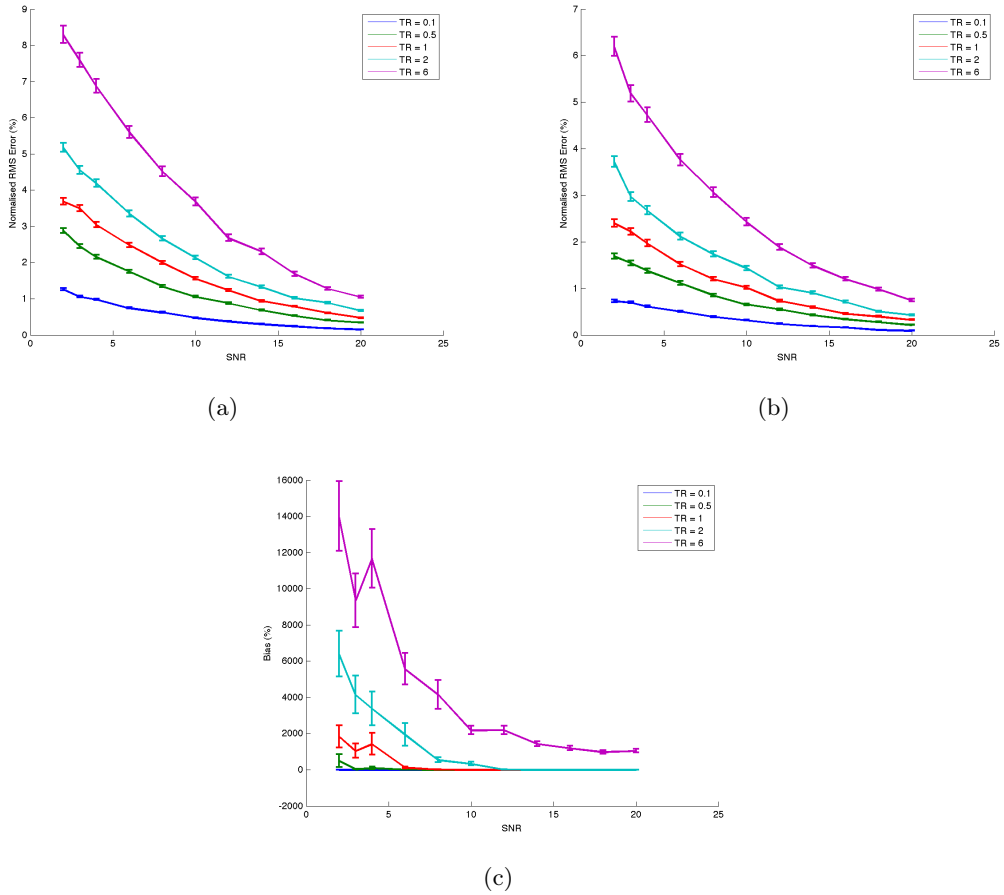

Figure 4.20: Results of Analysis for Model A_3, a critically damped 2nd order system of equation $\frac{4}{k_1^2}\ddot{f}_n(t)+\frac{4}{k_1}\dot{f}_n(t)+[f_n(t)-1]$, $k_1 = 2$. a) Profile of RMS signal error using nonlinear least squares estimation and 2 free parameters (ϵ_2, k_1). b) Profile of RMS signal error using linear least squares estimation and 1 free parameter (ϵ_2). c) Profile of bias in estimation of k_1.

accurate than the linear case but the biasing for estimation of k_1 was clearly evident in Figure 4.20c. Although it was an order of magnitude better than Models A_1 and A_2, estimation of k_1 for Model A_3 still suffered significant biasing with longer TRs.

1st Order Systems - Models A_4 and A_5 As with the 2nd order systems, profiles of the 1st order systems can be seen in Figures 4.21 and 4.22. Although there were less features contained in the 1st order systems compared to that in 2nd order systems, the responsiveness of the transition response was varied and profiled through simulations. Although only done for 1st order systems, the profiles of responsiveness would theoretically also hold true for 2nd order systems in terms of observing a general trend in estimation biasing.

Model A_4 - Of all the models, estimation of the fast 1st order system yielded the lowest biasing of the DM parameter estimate. The signal estimation profile seen in Figures 4.21a

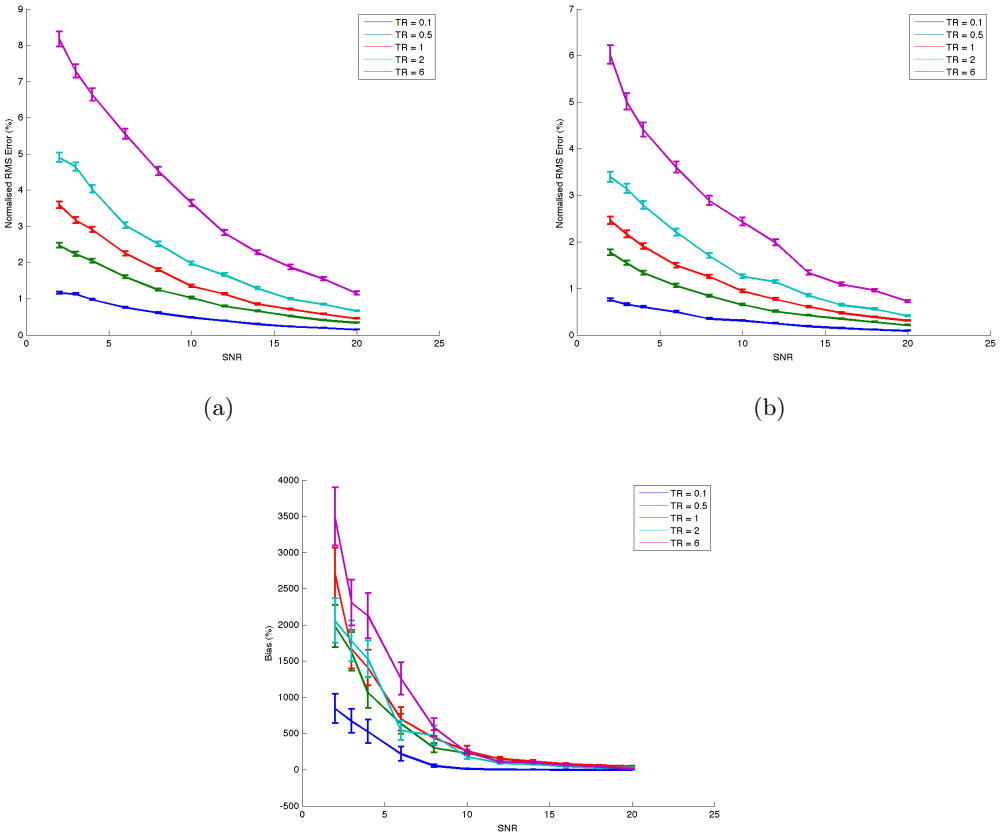

(a) (b)

(c)

Figure 4.21: Results of Analysis for Model A_4, a fast 1st order system of equation $\frac{1}{k}\dot{f}_n(t) + [f_n(t) - 1]$, $k = 5.0$. a) Profile of RMS signal error using nonlinear least squares estimation and 2 free parameters (ϵ_2, k). b) Profile of RMS signal error using linear least squares estimation and 1 free parameter (ϵ_2). c) Profile of bias in estimation of k.

and 4.21b are remarkably similar to that of Model A_3. However, biasing in estimation of k, seen in Figure 4.21c is around half a magnitude better than Model A_3 and a full magnitude better than Model A_5. The profile shows the same patterning of earlier analysis that estimation bias becomes much more pronounced with longer TR and there is an exponential growth in estimator bias with decreasing SNR.

Model A_5 - A comparison of parameter k estimation profiles of Model A_4 and Model A_5 (Figure 4.21c and Figure 4.22c respectively) shows that estimation biasing of Model A_5 is much more affected by TR than that of Model A_4. Although still an exponential growth with decreasing SNR, the bias grows much more quickly. Although both have the same signal estimation profiles - Figures 4.22a and 4.22b compared with Figures 4.21a and 4.21b - it seems that the slow 1st order models are less sensitive to changes in k than the fast 1st order models.

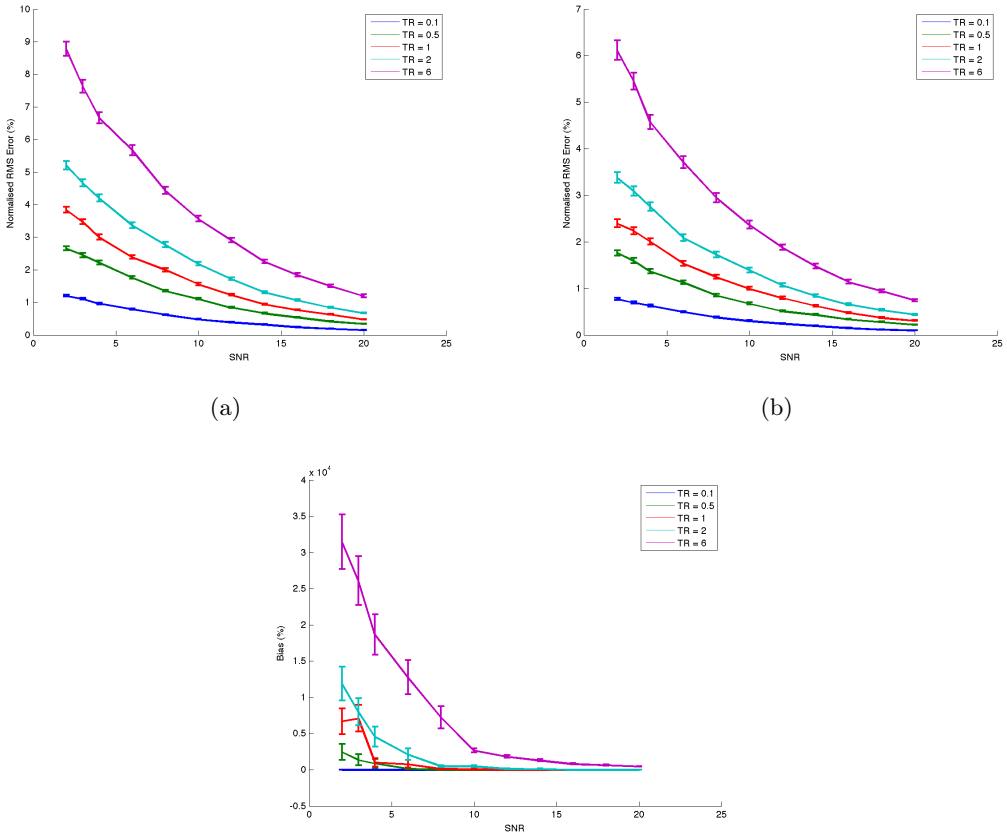

Figure 4.22: Results of Analysis for Model A_5, a slow 1st order system of equation $\frac{1}{k}\dot{f}_n(t) + [f_n(t) - 1]$, $k = 0.5$. a) Profile of RMS signal error using nonlinear least squares estimation and 2 free parameters (ϵ_2, k). b) Profile of RMS signal error using linear least squares estimation and 1 free parameter (ϵ_2). c) Profile of bias in estimation of k.

Analysis Summary As demonstrated by all five models (A_1 to A_5) tested, estimation of DM parameters face problems with estimator biasing, with the effect being much more exaggerated at higher TRs. The experimental ASL-fMRI dataset has a TR of 6.0 seconds and simulations show that it is not possible to estimate the parameters with any degree of certainty at that value. If the TR of the experiments were closer to 0.1 seconds, then DM parameter estimation would be beneficial as it is able to pick up the finer features offered using a more complicated 2nd order model. However, the simulated profiles created here clearly advises against the case for using nonlinear least squares for estimation of DM model parameters in current ASL-fMRI datasets. The estimation model may thus be simplified. Jittering of stimulus and detection has been used in recent experiments involving ASL (Diekhoff et al., 2011). However, the jittering of experimental results are in the range of seconds, an order of magnitude out from the level of jittering required to measure the finer effects of this experiment. Results from the analysis verify that parameters in the DM equation can be fixed to produce biologically plausible dynamics. In this way, the parameters in the DT equation could then be estimated using linear least squares, giving a faster estimation.

4.5 Analysis 2 - Estimation Bias for DT Parameters ϵ_1 and ϵ_4

The transient DT parameters (ϵ_1 and ϵ_4) are responsible for the responses occurring in a short span of time. These features in the signal may not be able to be seen during slow TR or may be distorted during high SNR. As such, simulations were done to determine regions within a SNR/TR profile that would be reasonable to include the parameters for estimation. As ϵ_1 and ϵ_4 could potentially vary between a range of values as well as being attached to different dynamic models, the simulation of such a large number of free-variables would be very difficult. It was decided to categorize the transient parameters into 3 DT groups: 'Weak', 'Normal' and 'Strong' with the generating ϵ_1 and ϵ_4 parameters taking values of 0.1, 1.0 and 10.0 respectively. Furthermore, four types of dynamic models all having fixed parameters were representative of the different dynamics that could be involved in real estimation. Table 4.6 shows 3 DTs and 4 DMs.

The analysis performed an SNR/TR profile of parameter estimates on each combination of DTs and DMs using 2000 trials per node. Estimates of ϵ_1 and ϵ_4 were obtained using the same estimation model as the generating model. There were 12 profiles calculated in all. The profiles for parameter ϵ_1 can be seen in Figure 4.23. Because the parameter profiles for ϵ_4 are similar to that of ϵ_1, it is omitted from the results for the sake of clarity.

	Driving Term	$\epsilon_1 \frac{d}{dt}u(t) + \epsilon_2 u(t) + \epsilon_3 \int u(t)\,dt, \quad 0 < t < T_{ON}$ $\epsilon_4 \frac{d}{dt}u(t), \quad t \geq T_{ON}$
	Weak Features	$\epsilon_1 = 0.1$, $\epsilon_2 = 0.4$, $\epsilon_3 = 0.02$, $\epsilon_4 = 0.1$
	Normal Features	$\epsilon_1 = 1.0$, $\epsilon_2 = 0.4$, $\epsilon_3 = 0.02$, $\epsilon_4 = 1.0$
	Strong Features	$\epsilon_1 = 10.0$, $\epsilon_2 = 0.4$, $\epsilon_3 = 0.02$, $\epsilon_4 = 10.0$
	Dynamic Models	
B_1	Oscillating 2nd Order System	$\frac{1}{k_2}\ddot{f}_n(t) + \frac{k_1}{k_2}\dot{f}_n(t) + [f_n(t) - 1]$, $k_1 = 2.0$, $k_2 = 1.09$
B_2	Overdamped 2nd Order System	$\frac{1}{k_2}\ddot{f}_n(t) + \frac{k_1}{k_2}\dot{f}_n(t) + [f_n(t) - 1]$, $k_1 = 2.0$, $k_2 = 0.91$
B_3	Critically Damped 2nd Order System	$\frac{4}{k_1^2}\ddot{f}_n(t) + \frac{4}{k_1}\dot{f}_n(t) + [f_n(t) - 1]$, $k_1 = 2.0$
B_4	1st Order System	$\frac{1}{k}\dot{f}_n(t) + [f_n(t) - 1]$, $k = 1$

Table 4.6: DT and DM values for determination of SNR/TR profiles for Analysis 2.

For analytical purposes, thresholding was used and an additional requirement was placed on the simulations: For each SNR/TR profile, given a particular TR value, find the lowest SNR that produces an estimation for ϵ_1 that is deemed to be 'acceptable'. In this case, the definition of 'acceptable' is defined arbitrarily as the estimate of ϵ_1 within 50% variance and 10% bias. The visualization for such requirement can be seen in Figure 4.25.

Analysis Summary From the estimates seen in Figure 4.25, it is clear that the best performing model in the majority of cases and especially at higher TR values is the 1st Order System. It can also be seen that the SNR required to produce an acceptable model increases very quickly from a TR = 0.1s to a TR = 0.5s and then rises more slowly as TR becomes larger. Furthermore, both weak and strong transient features yield less desired curves than the normal transients. Weak features, are harder to estimate as they are relatively small compared to the other features. Strong features tend to distort estimation of the non-transient parameters (ϵ_2 and ϵ_3)) and so would indirectly yield less accurate estimations. Normal features fulfill the Goldilocks - 'its just right' - principle to yield the best estimates out of all three features.

From the performance point of view, it is clear that the transient features are best included when the TR is 0.5 seconds or less. A TR of 1.0 seconds or more for all second order dynamics would require high SNR (15 or more) to compensate for the long TR. At a TR of 6.0 seconds, which is the TR of real ASL-fMRI measurements, a SNR of 30 or more would be needed to yield acceptable transient estimates. Due to the nature of

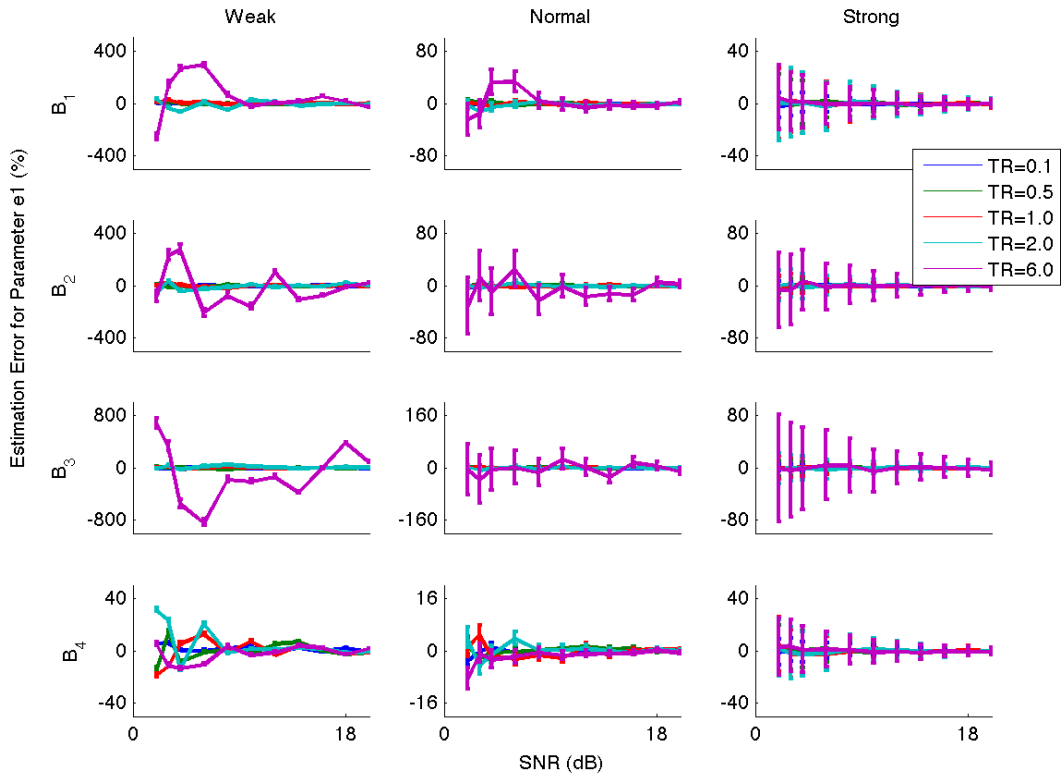

Figure 4.23: SNR/TR profiles for various DT and DM combinations for parameter ϵ_1. The columns correspond to the strength of DT transients: Weak, Normal and Strong. The rows correspond to various DMs: Oscillating 2nd Order (B_1), Overdamped 2nd Order (B_2), Critically Damped 2nd Order (B_3) and 1st Order (B_4). The figure at each of the nodes of the matrix correspond to the SNR/TR profile of bias in ϵ_1 bias generated for the combination of DT transient type and DM type.

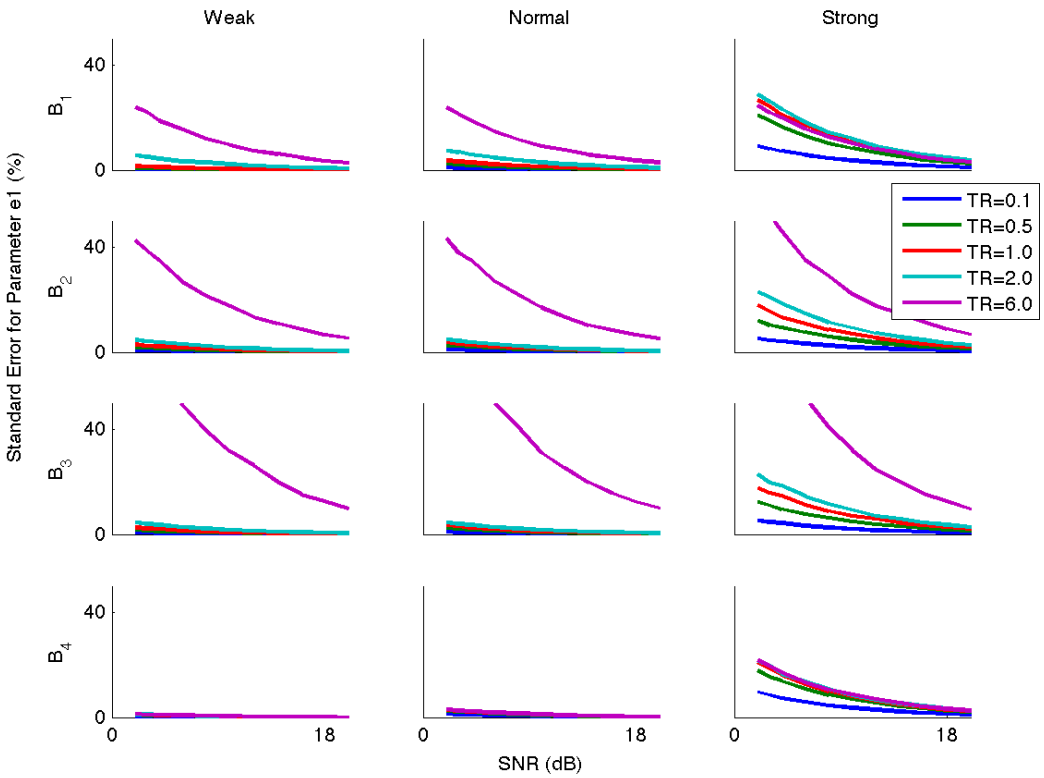

Figure 4.24: SNR/TR profiles for various DT and DM combinations for the standard error in bias for parameter ϵ_1. The profiles follow the same format as that in Figure 4.23 although only the standard error is plotted.

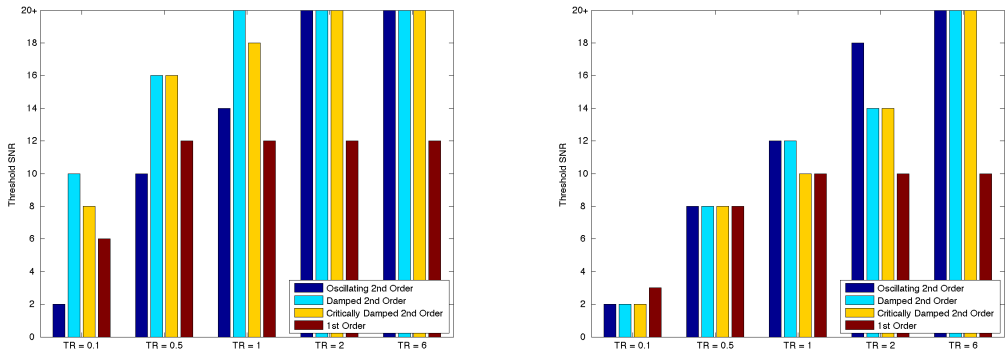

(a) (b)

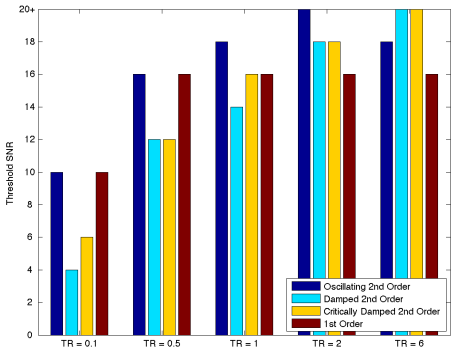

(c)

Figure 4.25: Lowest SNR threshold to yield 'acceptable' estimation of ϵ_1 (within 50% variance and 10% bias) with Weak, Normal and Strong Features. See Table 4.6 for model equations. Each plot determines the best model for a given TR using the given value of ϵ_1. With each group shown, the lower the bar, the better performing the model compared to its peers. For example, in graph a) whilst estimating weak features at TR=0.1, the blue bar representing the oscillating 2nd order system is the best performing model.

noise in ASL-fMRI datasets, an SNR of 30 would not be achievable and so the results shown in this simulation strongly advises including the transient ϵ_1 and ϵ_4 features in the estimation of experimental datasets.

4.6 Analysis 3 - Model Substitution and Simplification

The third analysis assumes that the underlying signal model and the model used for estimation can be different to each other. Because of the low SNR and long TR times in ASL-fMRI datasets, there is a possibility that two different models may yield similar types of signals and so may be substituted for each other. The following analysis tests this hypothesis with the understanding that if higher order and lower models are in fact similar for a given range of SNR/TR values, then the lower order model can be substituted for the higher order one for ease of calculation. The models used in the simulation can be seen in Table 4.7. Note that a 0th order system was also added as this was the simplest model available for CBF coupling.

Each of the five models were compared to each other in a matrix form so that one model acts as the generating model and the other acts as the estimation model. 25 model combinations were possible and SNR/TR profiles were done for all. The number of trials used for each node in the Grid was 2000. Results of Analysis 1 and Analysis 2 affected choice of selecting the parameters to be estimated; estimation of DM parameters were not included, nor that of estimation of DT parameters - the simulation was performed by setting ϵ_1 and ϵ_4 to zero. Only the signal, ϵ_2 and ϵ_3 were solved in the analysis.

Driving Term		
$\epsilon_1 \frac{d}{dt}u(t) + \epsilon_2 u(t) + \epsilon_3 \int u(t)\,dt, \quad 0 < t < T_{ON}$ $\epsilon_4 \frac{d}{dt}u(t), \qquad t \geq T_{ON}$ $\epsilon_1 = 0.0,\ \epsilon_2 = 0.4,\ \epsilon_3 = 0.005,\ \epsilon_4 = 0.0$		
Dynamic Models		
C_1	Oscillating 2nd Order System	$\frac{1}{k_2}\ddot{f}_n(t) + \frac{k_1}{k_2}\dot{f}_n(t) + [f_n(t) - 1]$, $k_1 = 2, k_2 = 5$
C_2	Damped 2nd Order System	$\frac{1}{k_2}\ddot{f}_n(t) + \frac{k_1}{k_2}\dot{f}_n(t) + [f_n(t) - 1]$, $k_1 = 2$, $k_2 = 0.91$
C_3	Critically Damped 2nd Order System	$\frac{4}{k_1^2}\ddot{f}_n(t) + \frac{4}{k_1}\dot{f}_n(t) + [f_n(t) - 1]$, $k_1 = 2$
C_4	1st Order System	$\frac{1}{k}\dot{f}_n(t) + [f_n(t) - 1]$, $k = 1$
C_5	0th Order System	$f_n(t) - 1$

Table 4.7: DT and DM values for determination of SNR/TR profiles for Analysis 3.

Results of the analysis can be seen in Figure 4.26. The graphs on the diagonal going from top-left to bottom-right show estimations using the same generating model as the

estimation model. These are the 'ideal' estimates. The graphs also show symmetry reflected on either side of the diagonal. This suggests that a higher order system cannot produce a better estimation of a lower order system when only ϵ_2 and ϵ_3 are estimated. An interesting aspect of the graphs show that although at TRs of 2.0 seconds or less, there is an error in estimation when the estimation model used is different generating model, at a TR of 6.0 seconds, the signals of the models begin to behave like each other. For example, in the case of Model (C_1) in Figure 4.26, which is an oscillating 2nd order system. It is clear that at TRs of 2.0 seconds or less, when different estimations models such as Models (C_2), (C_3) are used, the signal estimation error would stay at around 5% regardless of the increase in SNR. However at a TR of 6.0 seconds, high SNR results in the estimation error tending towards 0%. This result can be interpreted to mean that at a TR of 6.0 seconds, the oscillating 2nd order system can be substituted with an overdamped 2nd order system or a critically damped 2nd order system provided that the SNR is high enough. Conclusions such as this can be drawn between models from each of the graphs in Figure 4.26.

Because of the large amount of information provided through model comparison, an easier way to understand the data is through thresholding. Like Analysis 2, another condition was placed on the data for visualization purposes: Given a particular TR value, find the lowest SNR that produces an estimation of signal that is deemed acceptable (estimated signal RMS error of 10%). The results of each model can be seen in Figure 4.27.

Analysis Summary It can be seen from results in Figure 4.27 that at TR = 6.0 seconds, the 1st Order System can provide best fits for all the 2nd Order Systems whilst the 0th Order System obtains different signals from the rest. This leads to the conclusion that using a 1st Order System can be much more effective than using a whole group of 2nd Order Systems as it seems to be able to emulate the dynamics at both short and long TR times. Furthermore, it is interesting that at TR = 6.0 seconds, all the models bar the 0th order model have the same SNR threshold of estimation. This result indicates that all dynamic models become indistinguishable from each other at TR = 6.0 seconds. Effectively, it means that at a TR = 6.0 seconds, estimation of the CBF function using higher order dynamics than a 1st Order System becomes redundant.

4.7 Chapter Summary

In this section, the basic modules of the simulation framework was described as well as how such modules are built up in a hierarchical manner to form the model characteriza-

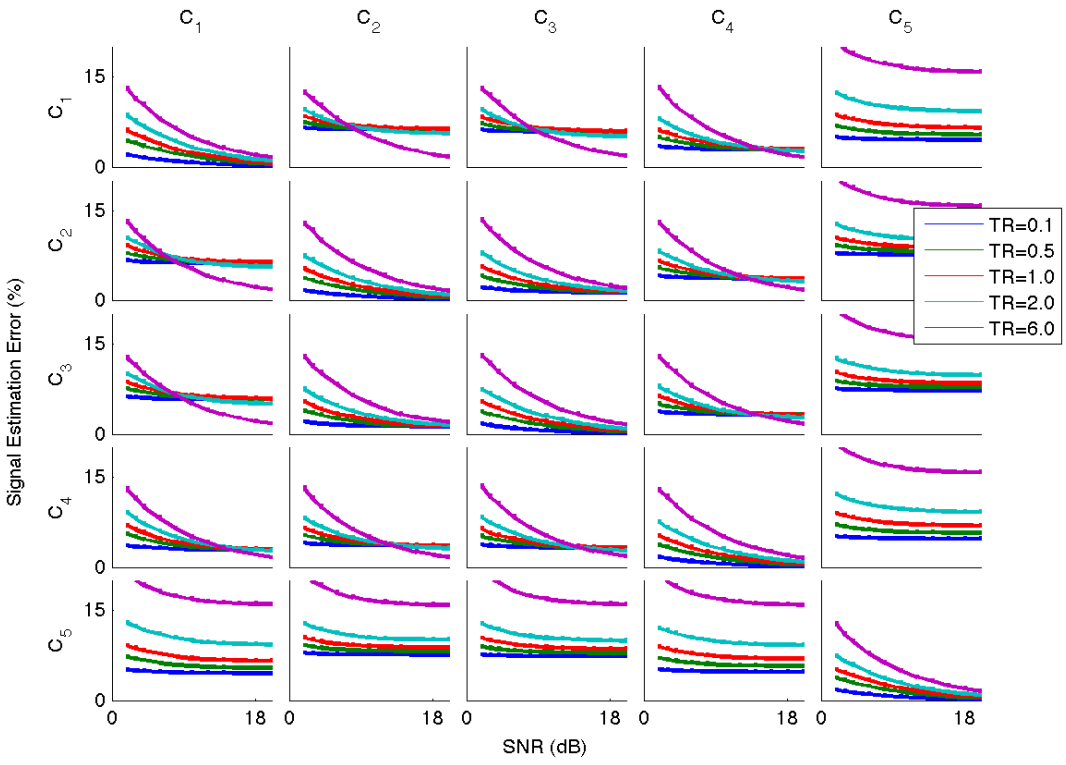

Figure 4.26: SNR/TR profiles for the model combinations used for analysis. The rows of the figure contain generating models whilst the columns of the figure contain the estimation models. Each graph within the matrix is an SNR/TR profile generated using the Grid Multiple Compare module having inputs of the generating model and estimation model at the indices of the graph with the matrix. For example: the graph on row C_2 and column C_4 shows the SNR/TR profile of signal comparison using the Damped 2nd Order System as the generating model and the 1st Order System as the estimation model.

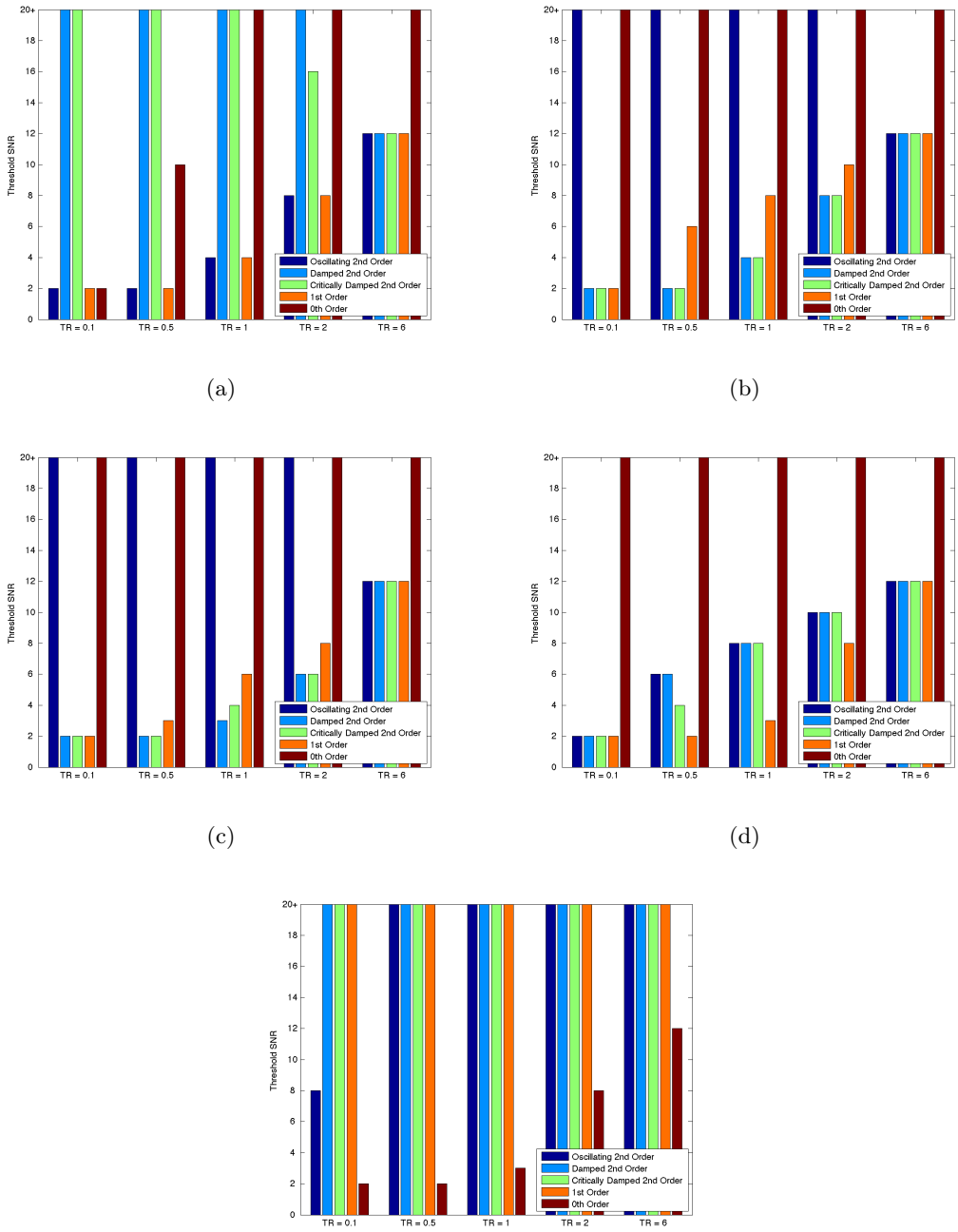

(a) (b)

(c) (d)

(e)

Figure 4.27: The lowest thresholded SNR in order to estimate a signal with RMS error of 10%. Each generating model has been given its own bar graph a) Oscillating 2nd Order System (C_1). b) Damped 2nd Order System (C_2). c) Critically Damped 2nd Order System (C_3). d) 1st Order System (C_4). e) Zeroth Order System (C_5). The lower the bar, the better the estimation by the relevant model. For example, in a) which the generating model is the Oscillating 2nd Order System; at TR=0.5 seconds, the 1st Order System is a better estimator of the oscillating 2nd order system than the 0th Order System, which is a better estimator that both the Damped 2nd Order and the Critically Damped 2nd Order Systems.

tion analysis work in order to describe advantages and disadvantages of using differential models for CBF modelling. It was found from analysis that the questions posed at the beginning of the chapter could be determined through simulation:

Question 1: In which range of SNR/TR values does the estimation of dynamic model parameters (k, k_1 and k_2) become unnecessary?

Result: Using the analysis done in Section 4.4, when the data concurrently contains TR $>$ 0.1 seconds and SNR $<$ 15 dB.

Question 2: In which range of SNR/TR values does the estimation of the transient parameters ϵ_1 and ϵ_4 become unnecessary?

Result: Using the analysis done in Section 4.5, when the data concurrently contains TR $>$ 1.0 seconds and SNR $<$ 10 dB.

Question 3: In which range of SNR/TR values does estimation with a lower order model yield the same or better accuracy than a higher order model?

Result: Using the analysis done in Section 4.6, when the data is sampled at TR $>$ 2.0 seconds.

From the results found for the different simulations, it can be seen that unless ASL-fMRI data collection is faster than 2.0 seconds, the use of dynamic systems to model CBF as well as any type of transient behaviour cannot be accurately done at a SNR lower than 10 dB. Whilst transient behaviour may in fact be present in the CBF signal, the behaviour cannot be estimated at the levels of noise and sampling rate found in the typical experimental ASL-fMRI dataset as will be shown in the following chapter (TR of 6.0 seconds and SNR roughly estimated to be around 20dB). These results are important as it determines the limits of data that CBF models can be used and will affect the decisions made for choosing models for fitting of experimental data as presented in the next chapter.

Chapter 5

Analysis of an Experimental Dataset

Simulations performed in chapter 4 enabled the prediction of a number of factors related to the accuracy of model estimation in response to noise. The results however does not provide any indication of how actual CBF data would behave as collected using ASL-fMRI. The main goal of the thesis is to determine whether ASL-fMRI data can be modelled better than the existing methods through inclusion of physiologically grounded parameters. This chapter aims to provide a slight variation of the original problem, investigating whether a model with more complex dynamics would better model CBF data over a standard 0th order system.

Following on from the previous chapter in conducting analysis of simulated CBF data, this chapter provides comparison of estimation using CBF models described in Chapter 3 to experimental data. Chapter 4 results enabled certain CBF models to be ommitted due to redundancy estimation. Performance of estimation using various CBF models were evaluated and then compared to one another to determine the best overall system to be used in estimation of CBF data collected using ASL-fMRI. After the whole brain was compared, regional comparison was done for various regions that looked for specific patterns of activation that would favor one model over another. A global correlation was performed over a number of key indicators to determine any trend in preference of one model over another.

5.1 Analysis Overview

5.1.1 Experimental Data

The data used for analysis was collected within the Melbourne University Neuroimaging Group for a pain analgesic study. Subjects in this study were subjected to âĂŸthumb squishesâĂŹ using a thumbscrew. The screw was applied in an on/off block design

pattern, and is referred to as the stimulus for the experiment. Subjects were asked to rate the level of pain they experienced for each stimulus application, on a scale of 1-10. There were 17 subjects in total each with 2 runs having 5 blocks in each run. In each block, the stimulus was applied at 12.0 seconds and held for 36.0 seconds and then a 30.0 second rest, giving a total time block of 78.0 seconds. The TR of the scan was 6.0 seconds and so there were 13 data points collected for each block. A table of experimental parameters can be seen in 5.1

Experiment Parameters	
No. Subjects	17
No. Runs	2 per Subject
No. Blocks	5 per Run
No. Images	13 per Block
Total Time	78.0 secs per Block
	390.0 secs per Run
TR	6.0 secs
Image Dimension	64 x 64 x 24
Voxel Size	3mm x 3mm x 5mm

Table 5.1: Experimental Parameters of the Pain Analgesic Study

5.1.2 Analysis Setup

Following on from model simulations performed in Chapter 4, further analysis was performed on the experimental dataset. Simulation results from Chapter 4 had indicated that models used for analysis of datasets with TR of 6.0 can be simplified. The number of combinations of DMs and DTs needed to be analysed (originally proposed in Table 3.2) were reduced. The long TR of the dataset meant that there was no need for estimation of driving term parameters ϵ_1 and ϵ_4 nor were there any need for estimation of transient dynamic coefficients for the 1st order (k) and 2nd order models (k_1 and k_2). These simplifications reduce the scope of the analysis to just 12 combinations made of 4 DMs and 3 DTs. Table 5.2 shows the equations governing the DM and DT equations whilst Table 5.3 shows the layout producing 12 models using the possible combinations of DMs and DTs. k, k_1 and k_2 were set as constants for each of the models.

As all free variables in the models are linear, analysis of the dataset was done using the linear least squares method (presented Section 3.6). Group results using t-statistics were produced for each of the 12 models and each set of results were compared for accuracy of estimation.

		DM Equations	
DM_0	0th Order	$f_n(t) - 1$	
DM_1	1st Order	$\frac{1}{k}\dot{f}_n(t) + [f_n(t) - 1]$	$k = 1.25$
DM_{2a}	2nd Order Critical	$\frac{4}{k_1^2}\ddot{f}_n(t) + \frac{4}{k_1}\dot{f}_n(t) + [f_n(t) - 1]$	$k_1 = 1.6$
DM_{2b}	2nd Order	$\frac{1}{k_2}\ddot{f}_n(t) + \frac{k_1}{k_2}\dot{f}_n(t) + [f_n(t) - 1]$	$k_1 = 1.5$, $k_2 = 1.0$
		DT Equations	
DT_2	Block Input	$\epsilon_2 u(t)$	
$DT4$	Ramp Input	$\epsilon_3 \int u(t)\, dt$	
DT_6	Block and Ramp Input	$\epsilon_2 u(t) + \epsilon_3 \int u(t)\, dt$	

Table 5.2: Reduced Combination of DM and DT Equations.

CBF Model Matrix				
		Dynamic Models		
Driving Terms	DM_0	DM_1	DM_{2a}	DM_{2b}
DT_2	$DM_0 = DT_2$	$DM_1 = DT_2$	$DM_{2a} = DT_2$	$DM_{2b} = DT_2$
DT_4	$DM_0 = DT_4$	$DM_1 = DT_4$	$DM_{2a} = DT_4$	$DM_{2b} = DT_4$
DT_6	$DM_0 = DT_6$	$DM_1 = DT_6$	$DM_{2a} = DT_6$	$DM_{2b} = DT_6$

Table 5.3: Reduced Matrix of Models from Combination of DM and DT Equations.

5.2 Analysis Results - Overall Summary

Group analysis using each of the 12 models provided a large amount of data to be inspected. Each DM had three different DTs producing estimates of parameters that required comparison. An example of such an output can be seen in Figure 5.1 where group-level parameter estimates of using 0th-order dynamics are compared with one another.

Parameter Estimation A common feature can be observed across all 12 models that can be seen in the following example: Figures 5.1a (which presents ϵ_2 estimations for a block input) and 5.1b (which presents ϵ_3 estimations for a block input) show very similar estimation profiles. This result suggests that estimation of CBF datasets using a ramp input can obtain relatively similar results to estimation using a block input. This result is actually quite surprising and on closer inspection is more due to the noisy nature of the data itself rather than any trend in modelling.

Another feature evident in the estimations across the 12 models can be found in Figures 5.1c and 5.1d which show ϵ_2 and ϵ_3 estimations for a model with block and ramp input. Although the estimations of both parameters are bigger than those in Figures 5.1a and 5.1b, it can be seen that the estimations actually produce signals that cancel each other out. When a region of 5.1c is red, the corresponding region of 5.1d is blue and vice-

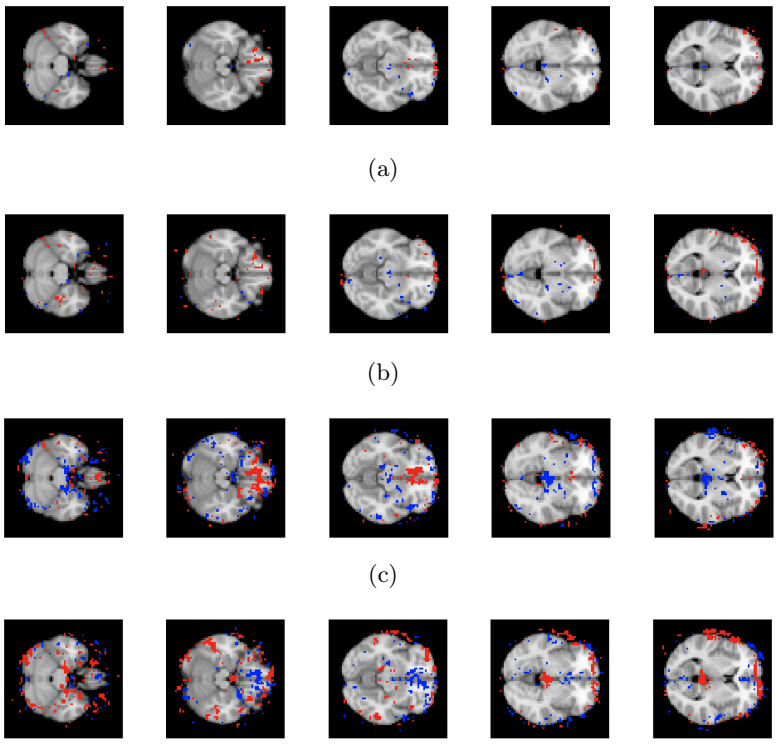

(a)

(b)

(c)

(d)

Figure 5.1: Samples of group-level parameter estimates calculated for the dataset using 0th-order dynamics. They show the most active regions in the group and voxels outside of the brain are purposely shown for indication of edge effects. a) ϵ_2 estimates calculated for a block input. Red: $\epsilon_2 > 0.01$, Blue: $\epsilon_2 < -0.01$. b) ϵ_3 calculated for a ramp input. Red: $\epsilon_3 > 0.0004$, Blue: $\epsilon_3 < -0.0004$. c) and d) respectively shows ϵ_2 and ϵ_3 using a block and ramp input. c) Red: $\epsilon_2 > 0.01$, Blue: $\epsilon_2 < -0.01$. d) Red: $\epsilon_3 > 0.0004$, Blue: $\epsilon_3 < -0.0004$.

versa. This seems to suggest that modelling using the block and ramp input, although providing a better overall fit, may not be providing a better interpretation than using only block or ramp inputs.

A closer examination of effectiveness of estimation uses calculation of Z-statistics for the group analysis. This can be seen in Figure 5.2. The graphs of Z-statistics correspond with parameter estimates seen in Figure 5.1. Note that Figure 5.2a displays statistics of 0th-order dynamics with a block input and is equivalent to the standard GLM analysis. Figure 5.2b displays a remarkably similar map to that of 5.2a and confirms the observations made earlier that modelling using a ramp input may produce very similar results to modelling using a block input. Furthermore, it can be seen that the Z-statistics are not as high in 5.2c and 5.2d, again suggesting that two parameter estimation may not be as effective as one parameter estimation. Also only 0th-order dynamics are shown, the scores are similar across different DMs. Note that the Z-values are very low in 5.2

Figure 5.3 shows the same type of result found in Figure 5.1 except that instead of using 0th-order dynamics, 2nd-order critically damped dynamics have been used. A

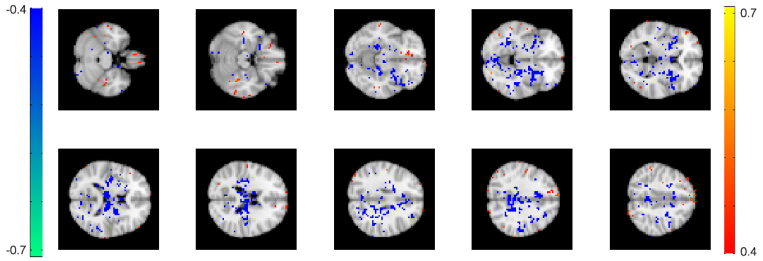

(a)

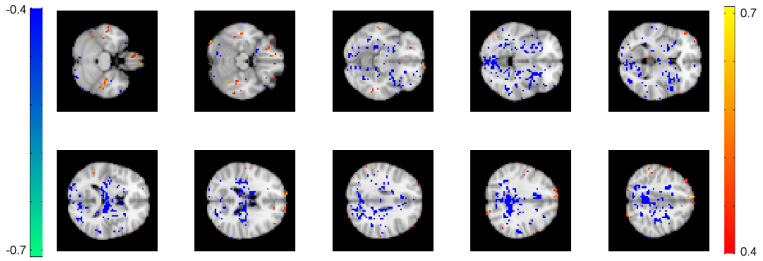

(b)

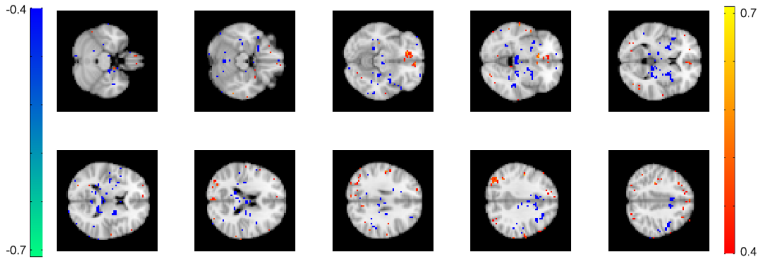

(c)

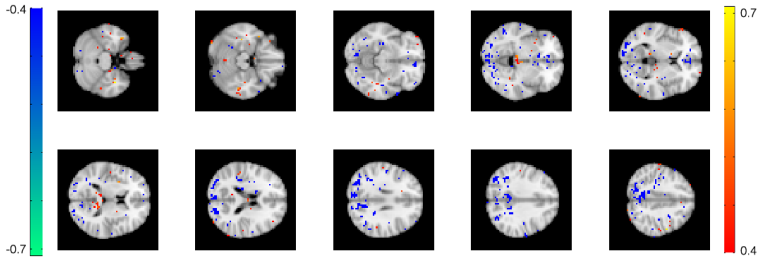

(d)

Figure 5.2: Samples of group-level Z-statistics calculated for the dataset using 0th-order model. The samples provide better understanding for how relevant parameter estimates are for each voxel within the analysis shown in Figure 5.1. The statistics were all masked to the region of the standard brain image. a) shows statistics for ϵ_2 estimates calculated for a block input. b) shows statistics for ϵ_2 estimates calculated for a ramp input. c) and d) respectively shows statistics for ϵ_2 and ϵ_3 using a block and ramp input.

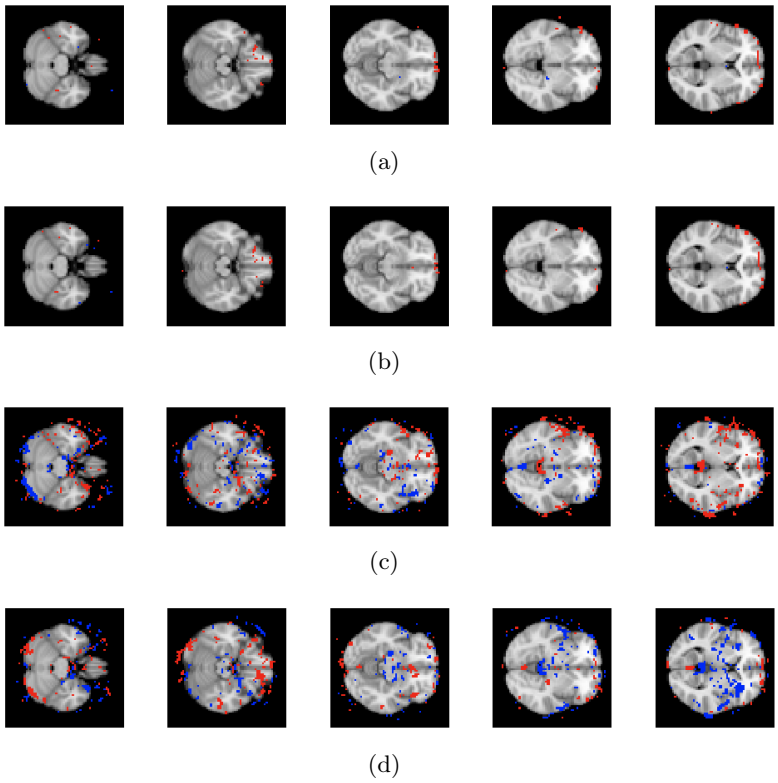

(a)

(b)

(c)

(d)

Figure 5.3: Samples of group-level parameter estimates calculated for the dataset using a 2nd-order model. They show the most active regions in the group and voxels outside of the brain are also shown for indication of edge effects. a) shows ϵ_2 estimates calculated for a block input. Red areas show ϵ_2 estimates > 0.01 whilst blue areas show $\epsilon_2 < -0.01$. b) shows ϵ_3 estimates calculated for a ramp input. Red areas show ϵ_3 estimates > 0.0004 whilst blue areas show $\epsilon_3 < -0.0004$. c) and d) respectively shows estimates for ϵ_2 and ϵ_3 using a block and ramp input. In c) Red areas show ϵ_2 estimates > 0.01 whilst blue areas show $\epsilon_2 < -0.01$. In d) Red areas show ϵ_3 estimates > 0.0004 whilst blue areas show $\epsilon_3 < -0.0004$.

comparison of the subfigures between Figure 5.1 and Figure 5.3 show very similar regions of activation.

Model Comparison After group analysis was performed using all 12 models, the results were compared with one another to determine which model was the best. Model selection algorithms (AIC and BIC introduced in Chapter 3) were used for model comparison. For each set of estimation results generated using the models, an AIC image as well as a BIC image was generated. The models were ranked for each voxel according to which was the most effective. Because of the sheer number of possibilities for comparing ranking, it was decided that the best overall model can be separated into the best overall DM and the best overall DT for easier classification. The DM comparison process and results can be seen in Figures 5.4 and 5.5. Because the AIC and BIC gave the same results due to the model having the same number of free parameters, Figures 5.4 and 5.5 show combined results. DT comparison process and results can be seen in Figures

5.6 and 5.7.

DM Comparison Figure 5.5 shows results from both AIC and BIC comparison. They are the same because the penalty term is redundant as the number of free parameters between DMs are the same. From the results, it is clear that the best performing DM was 0th-order dynamics, outperforming all other DMs in 67% of the total voxels. However, it can be seen that with a block input, the performance increases to 75%. An interesting sidenote about the block input results is that when the 0th-order dynamic is not the best performing, it becomes the worst. A faraway second is the 2nd-order critically damped dynamic with outperformance in 21% of all voxels. the 2nd-order system was the worst performing model across all voxels.

DT Comparison Figure 5.7 shows results from AIC and BIC comparisons of DTs. The two comparisons show very different results. Whilst the AIC method selected the block and ramp input as the overall best performing DT with 56% of all voxels, the BIC selected the block input as the best performing with 75% of all voxels. Such a large difference is due to the penalty terms punishing free-variables. The BIC is much more harsh on the free-parameters than AIC. This can be seen as the two-parametered block and ramp input was considered the worst performing model in all cases using the BIC model selection method.

Figure 5.7 highlights the difficulty in model selection algorithms and the varied results that algorithms produce. Ultimately, more information may be needed to decide the best model other than an algorithm. As the Z-statistics in Figure 5.2 have already shown that the block and ramp input may not be as effective as a single block or single ramp response, it seems that BIC comparison was the better indicator of model performance than the AIC in this case. As such, future comparisons will only show BIC comparisons for easier comprehension.

5.3 Analysis Results - Subregion Summary

From the results of comparison seen in Section 5.2, it is clear that at the image level, the best DM is the 0th-order system (67%) whilst the best DT is the block input (75%). However, it may be that specific regions of the brain may prefer different DMs and DTs. Furthermore, edge effects may also play a part in model selection. Masks were created to segment the images so that only the voxels in a particular region were considered for analysis. Figure 5.8 show masks M0 to M3 that were created. The M0 mask was the

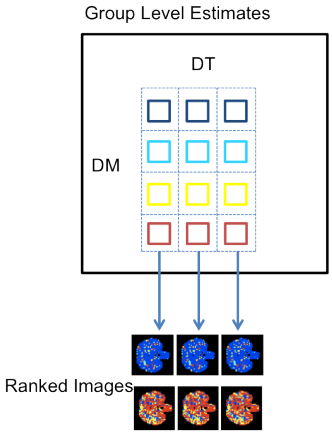

(a)

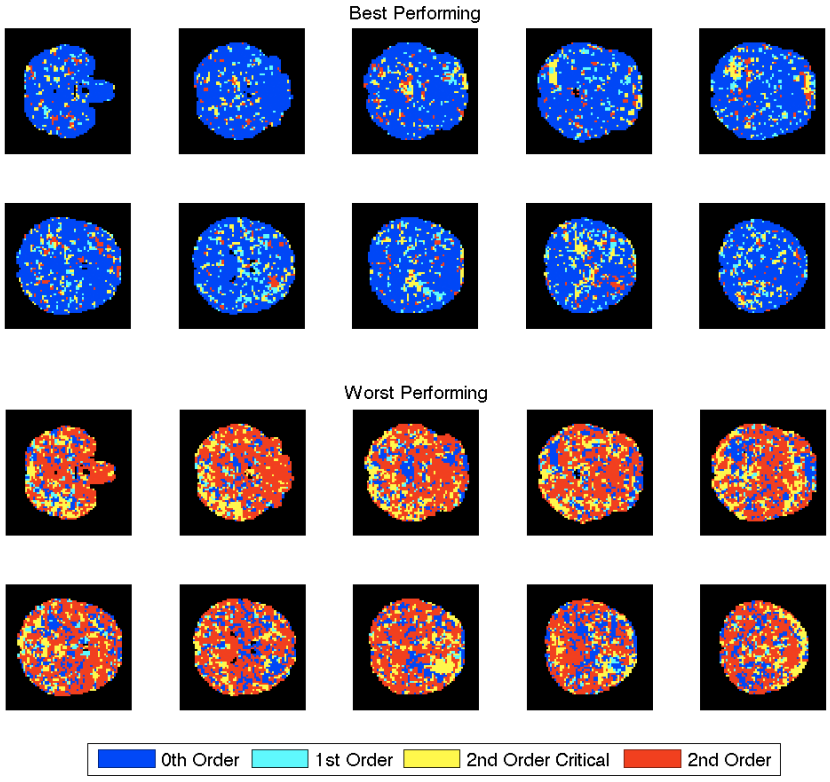

(b)

Figure 5.4: DM comparison process and results a) Ranking across each driving term, four dynamic models were compared to create an image representation of which model could fit the data the best. The region of interest was over all voxels. b) A sample comparison showing best and worst performing models within each voxel masked using the standard brain. The map compares performance of all DMs for a block DT.

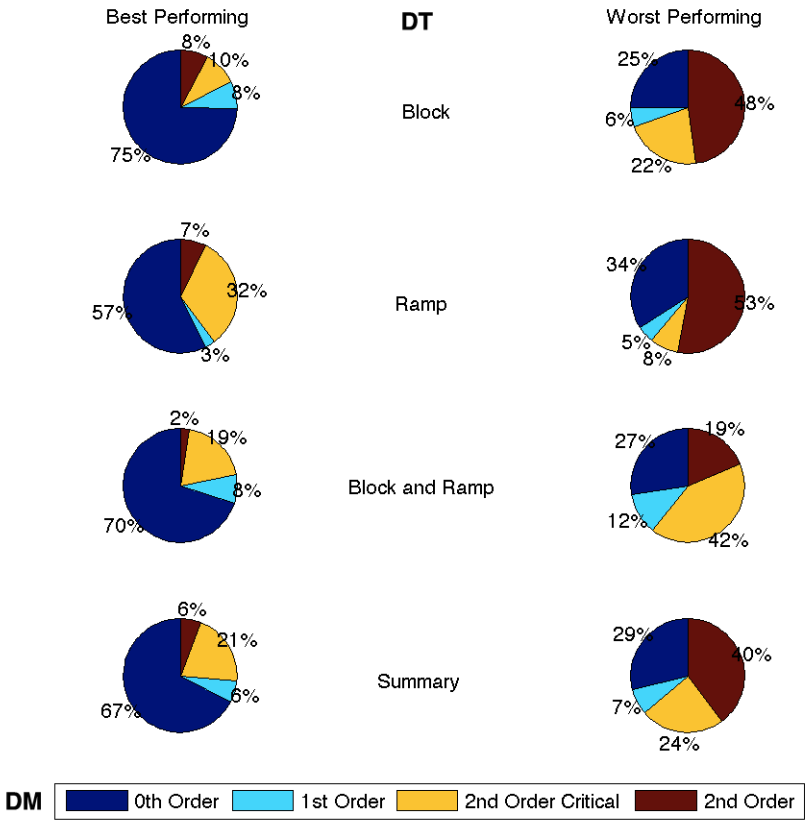

Figure 5.5: Summary of comparisons between estimator performance for different dynamic models for each type of driving terms as well as overall score. There were three different types of driving terms - block, ramp as well as block and ramp - with the overall performance being the an average of the three. Comparison was done using both AIC and BIC as the free parameters involved in estimation of driving terms were the same, both comparison framework gave the same results.

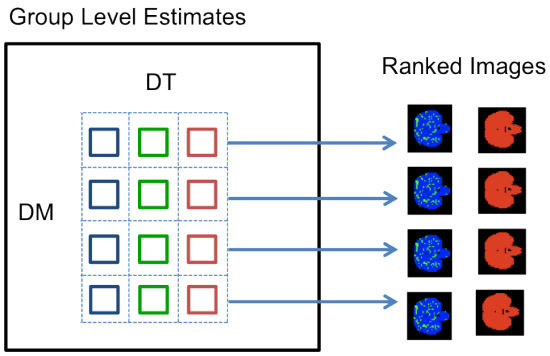

(a)

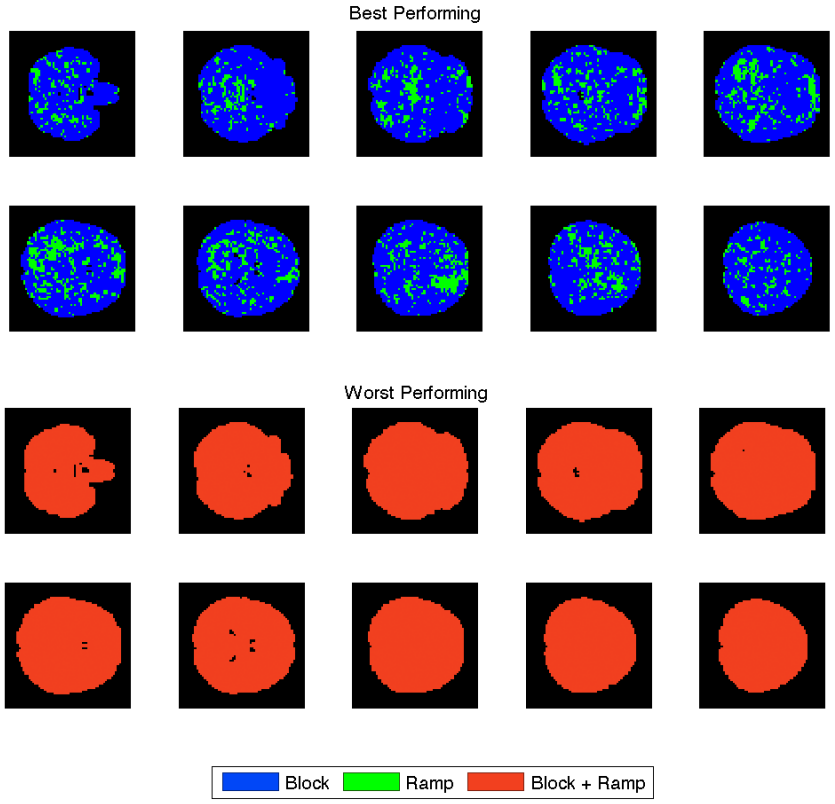

(b)

Figure 5.6: DT comparison process and results a) Ranking across each dynamic model, three driving terms were compared to create an image representation of which model could fit the data the best. The region of interest was over all voxels. b) Sample model comparison showing best and worst performing models within each voxel masked using the standard brain. The map compares all DTs for a 0th-Order DM.

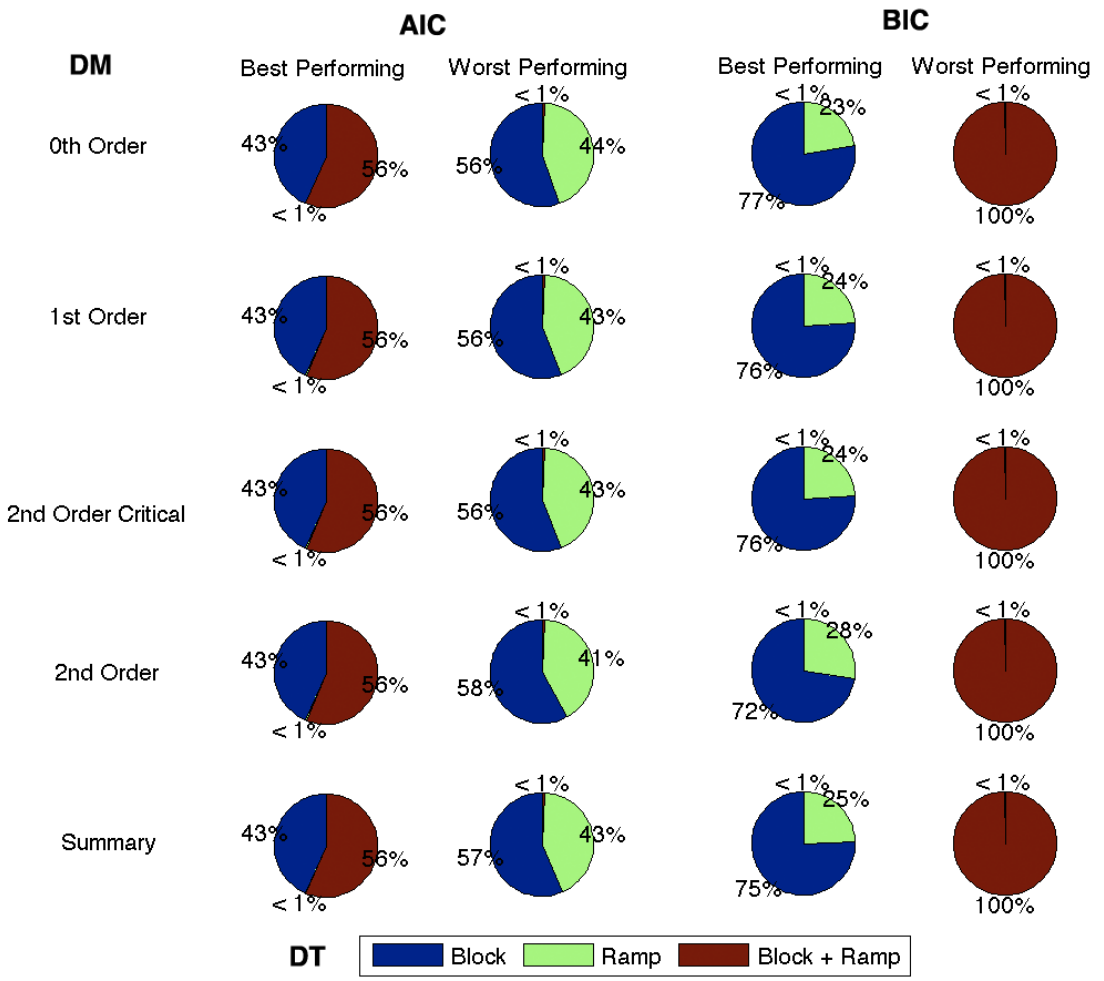

Figure 5.7: Summary of comparisons between estimator performance for different driving terms for each type of dynamic models as well as an overall score. This uses the same data as Figure 5.5 but cuts across it in a different way. For each of the four dynamic models, best and worse performing driving terms were calculated using both AIC and BIC and then summarized. An overall score provides the average across all four models. Note that mapping frequency of models in Figure 5.6(b) is seen in the pair of pie-charts on the right in the first row.

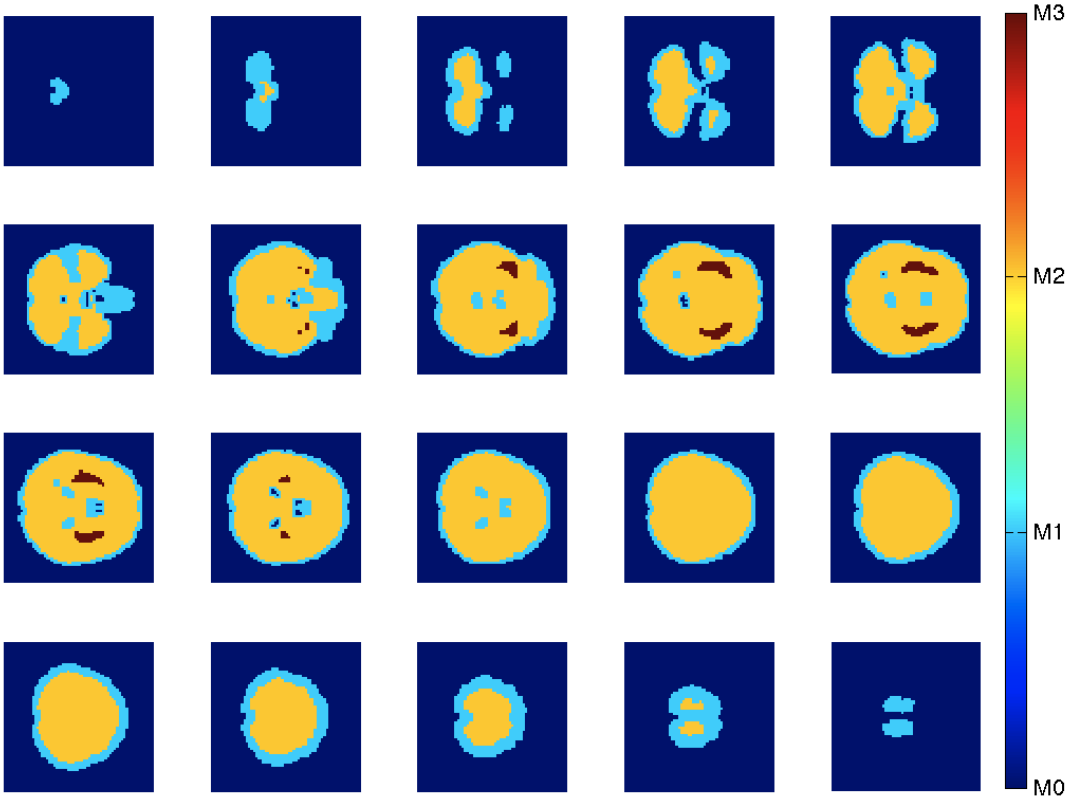

Figure 5.8: Map of masks used for regional analysis of statistics. M0 masks the entire image space. M1 masks just the volume of the brain. M2 masks inner volume of the brain and M3 masks the volume of the insular cortex.

same as previous section and only acts as a comparison for the other three. M1 masked the standard brain image whilst M2 masked the standard brain image without the outer volume. This was to minimize edge effects in the analysis. M3 masked the insular cortex, a region that showed negative activation and was found to be be active in pain-related studies (S Vulliemoz and Lemieux, 2009). The region mask was created and a recount of voxels containing best and worst model performance was done only within the region. Figures 5.9 and 5.10 show pie charts of the model comparisons for each of the masks.

It can be seen from Figure 5.9 that performance of the 0th-order system actually improves through segmenting the brain into areas M1 to M4. Comparing the values of overall statistics in M1 (70%) and M2 (71%) to M0 (67%), it is found that using the 0th-order system within the brain actually leads to a better performance of estimation than the entire image. Comparing M1 with M2, it can be seen that edge effects do not play a significant effect in estimator performance. The overall score of the 0th-order system is improved by 1% whilst there appear to be no significant change in other DMs. There is no change for best performing models when only the block input is taken into account. M3 masks an anatomically specific region, the 0th-order performance in M3 was exceptionally; out of all DMs using the block input, the 0th-order model outperformed

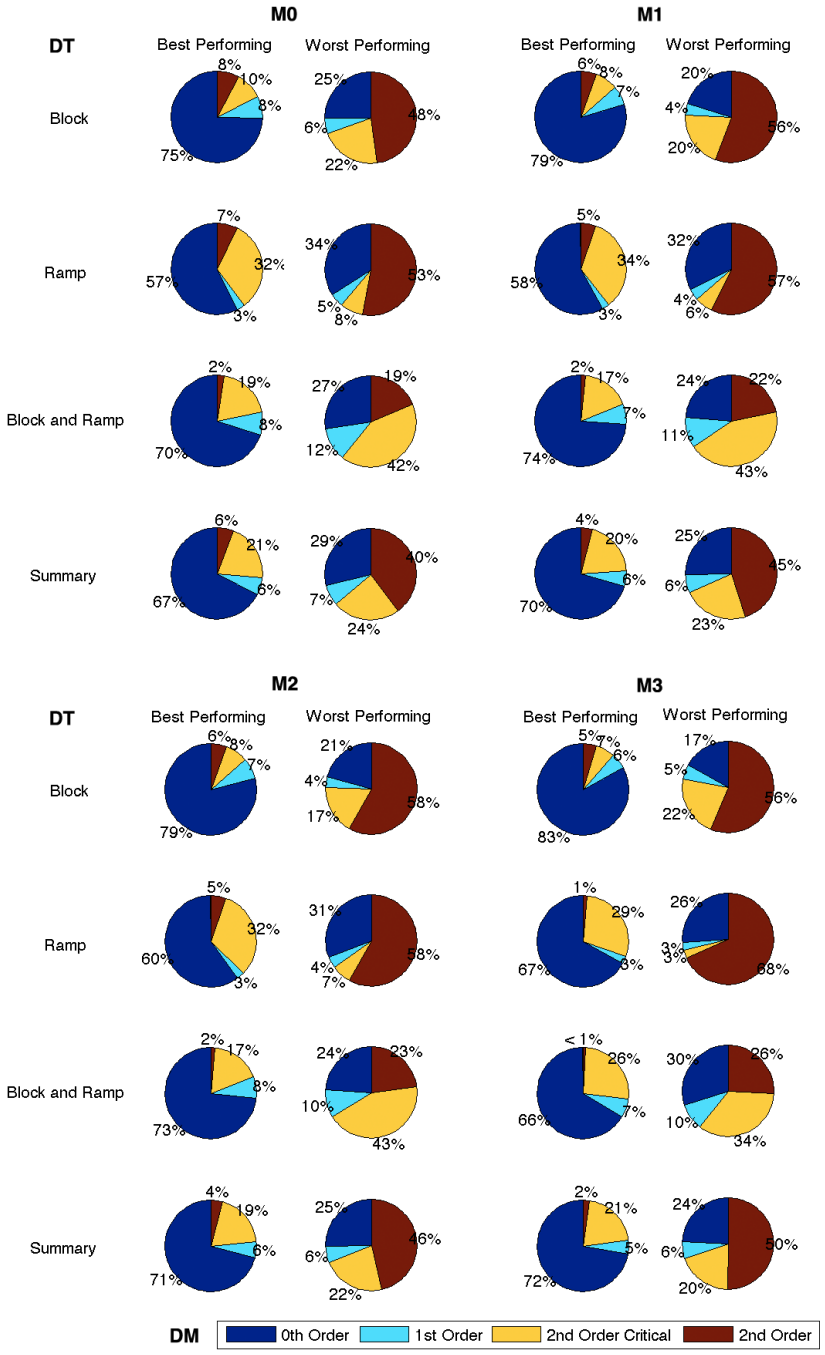

Figure 5.9: Summary of comparisons between estimator performance for different dynamic models for each type of driving terms as well as overall score done for each of the masking regions M0 to M3. The analysis for M0 can also be seen in Figure 5.5 but is shown here for comparison with regional analysis.

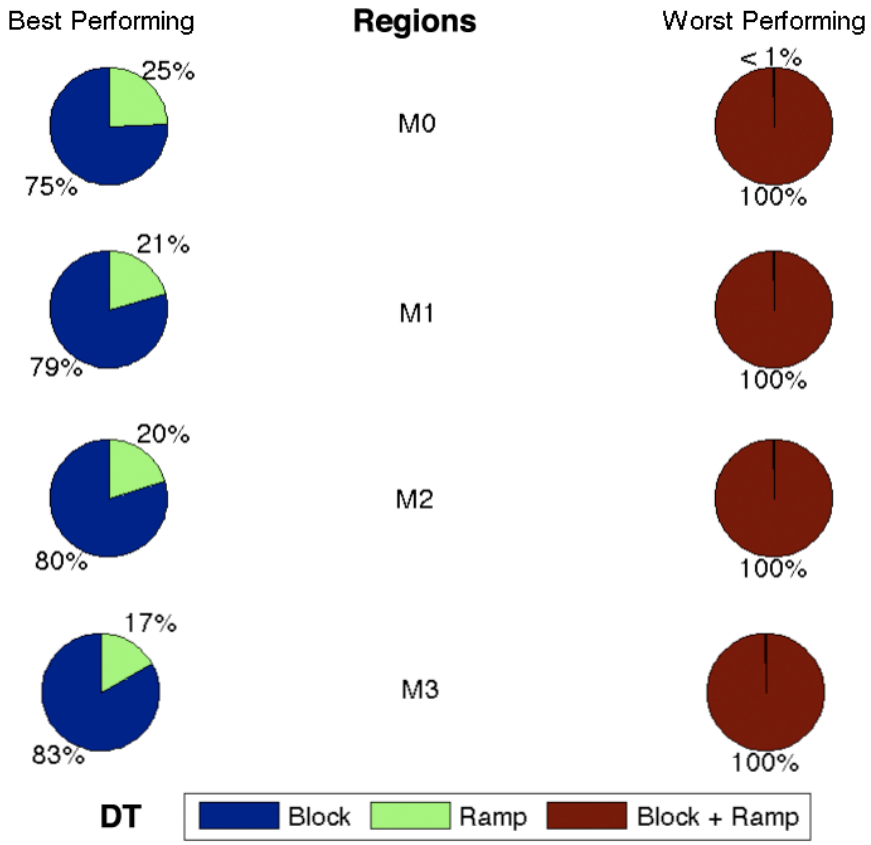

Figure 5.10: Summary of BIC comparison between estimator performance for different driving terms for each of the masking regions M0 to M3.

all others in 83% of all voxels within the region. The worst performing model for M3 was again the 2nd-order system.

Figure 5.10 shows the overalls statistics for DT comparison across the masks. As with the 0th-order DM, the block DT was by far the most outstanding performer and even increases its lead over the ramp input the more region specific the mask became. The worse performer was the block and ramp input as BIC penalized for the extra free parameter.

5.4 Analysis Results - Anatomical Summary

The significant jump in estimator performance within the insular cortex brought up an interesting question: Are there any trends or patterns that may influence model selection? The question was answered by creating further masks. A total of 48 anatomical regions were used to mask the data. The masks can be seen in Figure 5.11 and their corresponding names are given in Figure 5.12 along with key statistics.

Figure 5.12 shows key statistics for each region and shows the variability of estimated

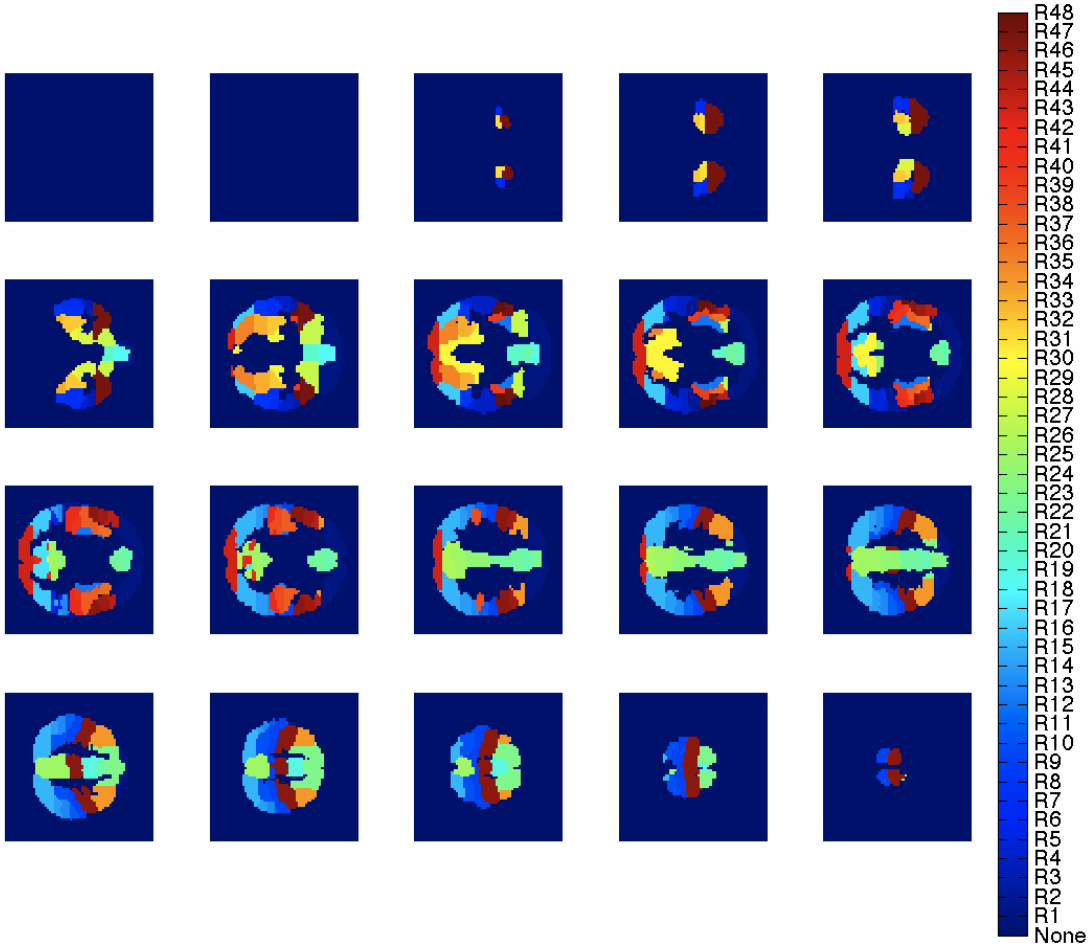

Figure 5.11: Map of masks used for analysis of statistics by anatomical region. The color-bar show the masks for the 48 regions (R1 to R48) used for analysis, of which, the descriptions can be seen in Figure 5.12

Sections	Mask Number	A. Total Number of Voxels	B. % Voxels with E2 Activation above 0.01	C. % Voxels with E2 Activation above 0.005	D. % Voxels with E3 Activation above 0.0005	E. % Voxels with E3 Activation above 0.00025	F. % Voxels with Block as Best Shape	G. % Voxels with Ramp as Best Shape	H. % Voxels with 0th-Order as Best Model	I. % Voxels with 1st-Order as Best Model	J. % Voxels with 2nd-Order Critical as Best Model	K. % Voxels with 2nd-Order as Best Model	L. Maximum E2 Value	M. Minimum E2 Value	N. Maximum E3 Value	O. Minimum E3 Value
Frontal Pole	1	2227	8%	29%	9%	27%	80%	20%	69%	4%	22%	4%	0.1370	-0.0138	0.0031	-0.0006
Insular Cortex	2	335	1%	6%	1%	4%	86%	14%	72%	5%	20%	3%	0.0198	-0.0107	0.0008	-0.0004
Superior Frontal Gyrus	3	144	1%	6%	1%	3%	89%	11%	72%	6%	20%	2%	0.0135	-0.0082	0.0006	-0.0003
Middle Frontal Gyrus	4	393	0%	10%	0%	6%	87%	13%	74%	3%	21%	2%	0.0095	-0.0089	0.0005	-0.0004
Inferior Frontal Gyrus, pars triangularis	5	337	0%	3%	0%	4%	87%	13%	71%	5%	20%	3%	0.0086	-0.0092	0.0006	-0.0004
Inferior Frontal Gyrus, pars opercularis	6	121	1%	5%	1%	9%	82%	18%	76%	2%	16%	6%	0.0113	-0.0104	0.0005	-0.0004
Precentral Gyrus	7	330	1%	17%	0%	15%	83%	18%	72%	3%	23%	3%	0.0137	-0.0089	0.0007	-0.0002
Temporal Pole	8	234	1%	8%	0%	9%	84%	16%	81%	2%	15%	2%	0.0117	-0.0090	0.0005	-0.0004
Superior Temporal Gyrus, anterior division	9	1073	3%	17%	1%	10%	83%	17%	66%	6%	25%	3%	0.0298	-0.0102	0.0008	-0.0004
Superior Temporal Gyrus, posterior division	10	437	1%	9%	0%	5%	78%	22%	71%	5%	19%	5%	0.0180	-0.0053	0.0008	-0.0004
Middle Temporal Gyrus, anterior division	11	298	3%	10%	2%	7%	89%	11%	69%	7%	23%	1%	0.0189	-0.0100	0.0008	-0.0005
Middle Temporal Gyrus, posterior division	12	427	0%	0%	0%	0%	83%	17%	72%	5%	21%	2%	0.0042	-0.0111	0.0003	-0.0005
Middle Temporal Gyrus, temporooccipital part	13	397	1%	7%	1%	6%	88%	12%	67%	7%	24%	2%	0.0163	-0.0081	0.0008	-0.0004
Inferior Temporal Gyrus, anterior division	14	396	0%	4%	0%	3%	82%	18%	68%	6%	20%	5%	0.0107	-0.0078	0.0005	-0.0004
Inferior Temporal Gyrus, posterior division	15	1340	0%	6%	0%	6%	78%	22%	72%	5%	19%	4%	0.0113	-0.0114	0.0006	-0.0005
Inferior Temporal Gyrus, temporooccipital part	16	642	0%	4%	0%	3%	83%	17%	72%	5%	18%	5%	0.0099	-0.0120	0.0005	-0.0006
Postcentral Gyrus	17	238	0%	0%	0%	0%	72%	28%	74%	4%	18%	4%	0.0024	-0.0098	0.0001	-0.0005
Superior Parietal Lobule	18	159	7%	48%	2%	21%	87%	13%	74%	2%	23%	0%	0.0173	-0.0067	0.0005	-0.0003
Supramarginal Gyrus, anterior division	19	203	0%	6%	1%	6%	87%	13%	62%	10%	24%	3%	0.0109	-0.0074	0.0005	-0.0003
Supramarginal Gyrus, posterior division	20	173	6%	32%	1%	13%	86%	14%	75%	3%	22%	1%	0.0155	-0.0070	0.0005	-0.0004
Angular Gyrus	21	469	0%	3%	0%	1%	82%	18%	76%	5%	14%	5%	0.0087	-0.0107	0.0003	-0.0004
Lateral Occipital Cortex, superoir division	22	397	0%	0%	0%	0%	86%	14%	75%	5%	17%	3%	0.0055	-0.0107	0.0002	-0.0005
Lateral Occipital Cortex, inferior division	23	788	4%	20%	3%	14%	80%	20%	61%	9%	24%	6%	0.0378	-0.0080	0.0010	-0.0004
Intracalcarine Cortex	24	387	0%	1%	0%	1%	74%	26%	74%	6%	16%	4%	0.0073	-0.0117	0.0004	-0.0007
Frontal Medial Cortex	25	799	1%	4%	0%	1%	78%	22%	71%	6%	18%	6%	0.0207	-0.0174	0.0009	-0.0009
Juxtapositional Lobule Cortex	26	211	0%	1%	0%	1%	72%	28%	77%	3%	15%	4%	0.0110	-0.0088	0.0003	-0.0004
Subcallosal Cortex	27	476	2%	12%	1%	11%	90%	10%	74%	4%	20%	2%	0.0156	-0.0125	0.0006	-0.0006
Paracingulate Gyrus	28	222	2%	6%	0%	9%	80%	20%	76%	3%	15%	6%	0.0113	-0.0127	0.0006	-0.0005
Cingulate Gyrus, anterior division	29	146	0%	0%	0%	0%	64%	36%	72%	2%	17%	8%	0.0033	-0.0098	0.0002	-0.0005
Cingulate Gyrus, posterior division	30	543	0%	0%	0%	0%	65%	35%	72%	5%	16%	7%	0.0084	-0.0128	0.0004	-0.0006
Precuneous Cortex	31	115	3%	24%	3%	25%	68%	32%	79%	3%	11%	6%	0.0116	-0.0082	0.0007	-0.0004
Cuneal Cortex	32	269	4%	17%	3%	20%	77%	23%	76%	3%	16%	5%	0.0147	-0.0092	0.0008	-0.0003
Frontal Orbital Cortex	33	225	0%	5%	0%	4%	70%	30%	69%	5%	19%	7%	0.0140	-0.0095	0.0006	-0.0004
Parahippocampal Gyrus, anterior division	34	822	3%	15%	2%	11%	82%	18%	62%	9%	24%	5%	0.0312	-0.0099	0.0010	-0.0004
Parahippocampal Gyrus, posterior division	35	320	0%	1%	0%	0%	73%	27%	69%	8%	15%	8%	0.0066	-0.0109	0.0002	-0.0004
Lingual Gyrus	36	146	0%	1%	0%	1%	86%	14%	79%	5%	14%	2%	0.0061	-0.0069	0.0003	-0.0004
Temporal Fusiform Cortex, anterior division	37	318	1%	5%	0%	3%	83%	17%	66%	8%	23%	3%	0.0126	-0.0085	0.0004	-0.0004
Temporal Fusiform Cortex, posterior division	38	164	1%	1%	1%	1%	86%	14%	69%	6%	24%	1%	0.0250	-0.0067	0.0011	-0.0004
Temporal Occipital Fusiform Cortex	39	150	0%	2%	0%	1%	89%	11%	74%	4%	20%	2%	0.0097	-0.0085	0.0003	-0.0004
Occipital Fusiform Gyrus	40	110	0%	1%	0%	0%	89%	11%	77%	5%	17%	1%	0.0071	-0.0051	0.0002	-0.0003
Frontal Operculum Cortex	41	180	1%	4%	1%	4%	89%	11%	69%	7%	21%	2%	0.0111	-0.0065	0.0006	-0.0004
Central Opercular Cortex	42	63	0%	0%	0%	0%	59%	41%	76%	3%	15%	6%	0.0018	-0.0054	0.0000	-0.0003
Parietal Operculum Cortex	43	804	1%	5%	0%	5%	78%	22%	72%	5%	19%	4%	0.0158	-0.0110	0.0006	-0.0005
Planum Polare	44	193	7%	22%	7%	24%	89%	11%	70%	6%	20%	4%	0.0187	-0.0074	0.0010	-0.0002
Heschl's Gyrus (includes H1 and H2)	45	243	2%	7%	2%	7%	90%	10%	66%	8%	23%	2%	0.0139	-0.0069	0.0008	-0.0003
Planum Temporale	46	1316	1%	13%	1%	7%	86%	14%	71%	5%	21%	3%	0.0175	-0.0244	0.0008	-0.0005
Supracalcarine Cortex	47	731	1%	8%	1%	7%	84%	16%	72%	4%	20%	4%	0.0197	-0.0127	0.0010	-0.0006
Occipital Pole	48	110	2%	10%	0%	4%	89%	11%	66%	9%	22%	3%	0.0136	-0.0087	0.0004	-0.0005

Figure 5.12: Description and important statistics for each of the anatomical regions.

parameters across the brain. Columns of the table are labeled A to O, each containing a different key statistic for the region. By visualizing the columns against each other as scatter plots, it is possible to determine trends about the data. A hypothesis tested using scatter plots shown in Figure 5.13 was that the number of voxels in the region may affect model selection. All three plots showed no correlation between the two as the R^2 value was close to 0.

Tests to determine correspondence between parameters did not find any results that were deemed significant. A hypothesis tested using scatter plots shown in Figure 5.14 was that the percentage of activated voxels in the region may affect model selection. Again, all three plots showed no correlation between the two (R^2 value was close to 0).

Because of the sheer number of combinations of scatter-plots that could be produced, a more compact representation of correlation between the columns is necessary to allow understanding of trends in data. The Pearson's Regression (R) can be seen in Figure 5.15 and the R^2 values seen in Figure 5.16. From the two tables, it is possible to visually determine whether there are correlations in data. For example, a correlation between the percentage of voxels with block input as the best DT (Column F) and the percentage of voxels with 0th-order dynamics as the best DM (Column H) shows in Figure 5.16 having R^2 value of 0.037 between the two columns, meaning minimal correlation.

From analysis of the results seen in Figures 5.13 to 5.16, there was no obvious trend to model estimation performance being influenced by factors such as the number of voxels in the region, the percentage of activated voxels in the region, nor by the maximum/minimum values of parameters estimates within the region. It seems that 0th-order dynamics and block input are the best overall DM and DT respectively. Neither higher-order dynamics, nor the addition of a ramping input add to the performance of estimation both on a whole brain level as well as at a regional level and there does not seem to be any evidence to show that higher models perform better in activated regions or in inactive regions. Put simply, the data favors the use of the simplest model of activation and the principle of parsimony is very much alive in modelling this particular CBF dataset.

5.5 Chapter Summary

This chapter expands upon results of Chapter 4, using a analysis framework for investigation into experimental data to understand effectiveness of fitting CBF data using the proposed ASL-fMRI models. Evidence presented in this chapter suggests that higher-order dynamics and additional features such as ramping do not add significant under-

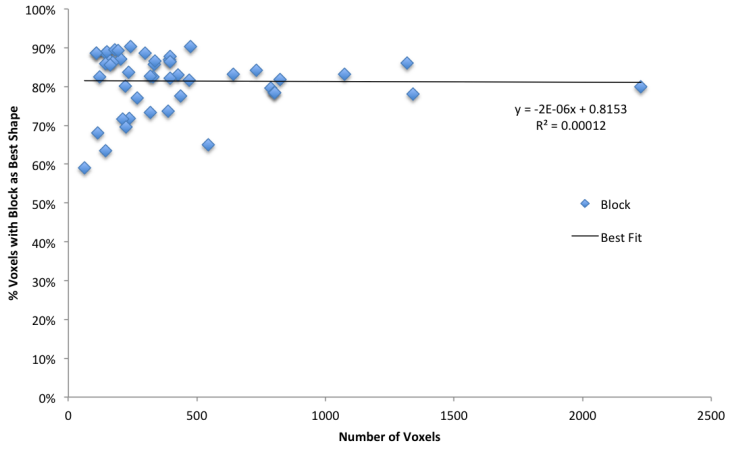

(a)

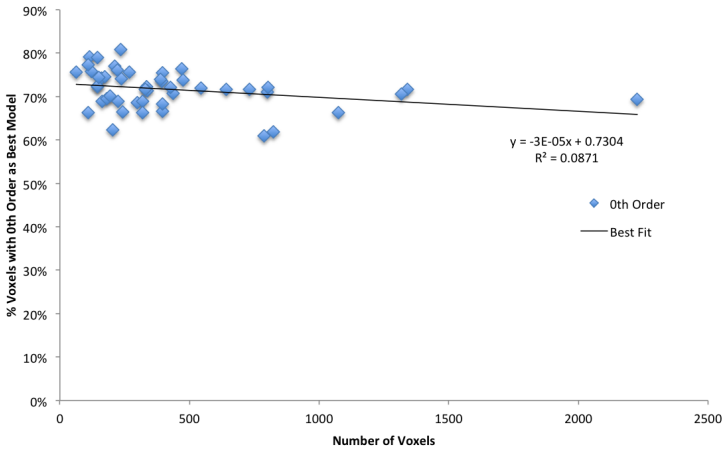

(b)

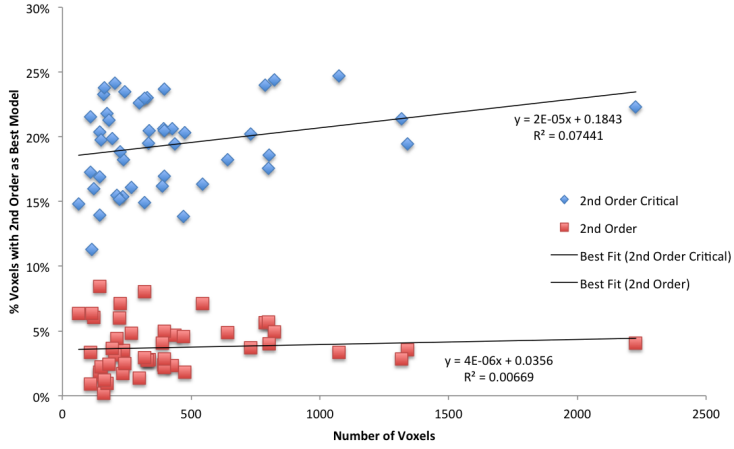

(c)

Figure 5.13: Correlations between columns of Figure 5.12. a) Correlation between Number of Voxels (Column A) and Number of Voxels with block input as the best driving term (Column F). b) Correlation between Number of Voxels (Column A) and Number of Voxels with 0th-order model as best dynamic model (Column H) c) Two correlations - Number of Voxels (Column A) and Number of Voxels with 2nd-order critical model as best dynamic model (Column J) in blue as well as Number of Voxels (Column A) and Number of Voxels 2nd-order model as best dynamic model (Column K) in red.

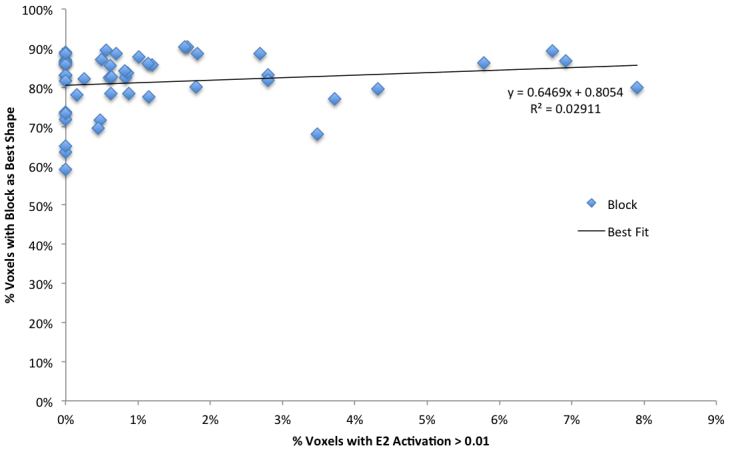

(a)

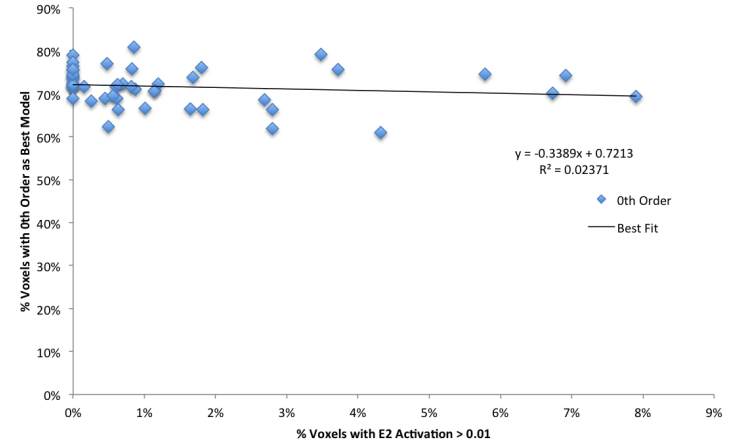

(b)

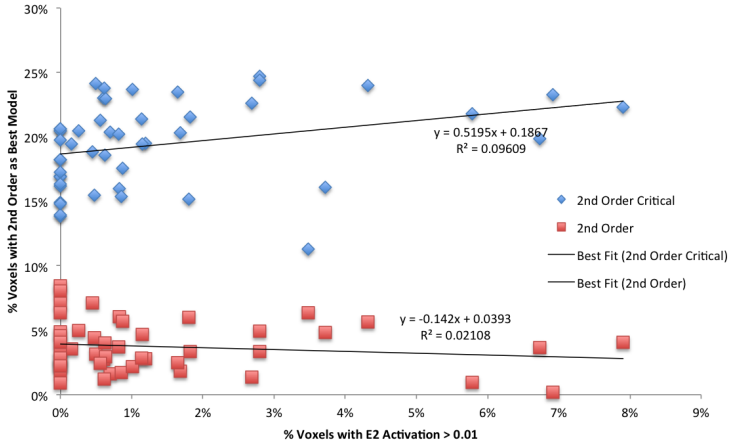

(c)

Figure 5.14: Correlations between columns of Figure 5.12. a) Correlation between Percentage of Voxels with $\epsilon_2 > 0.01$ (Column B) and Percentage of Voxels with block input as the best driving term (Column F). b) Correlation between Percentage of Voxels with $\epsilon_2 > 0.01$ (Column B) and Percentage of Voxels with 0th-order model as best dynamic model (Column H) c) Two correlations - Percentage of Voxels with $\epsilon_2 > 0.01$ (Column B) and Percentage of Voxels with 2nd-order critical model as best dynamic model (Column J) in blue as well as Percentage of Voxels with $\epsilon_2 > 0.01$ (Column B) and Percentage of Voxels 2nd-order model as best dynamic model (Column K) in red.

	O	N	M	L	K	J	I	H	G	F	E	D	C	B
A	-0.45	0.71	-0.60	0.74	0.08	0.27	0.11	-0.30	0.01	-0.01	0.28	0.43	0.23	0.29
B	0.16	0.62	0.06	0.63	-0.15	0.31	-0.04	-0.15	-0.17	0.17	0.87	0.82	0.90	
C	0.23	0.46	0.05	0.45	-0.24	0.35	-0.15	-0.09	-0.20	0.20	0.86	0.60		
D	0.10	0.78	-0.06	0.75	0.01	0.17	0.04	-0.15	-0.10	0.10	0.83			
E	0.24	0.61	0.02	0.54	-0.07	0.19	-0.16	-0.04	-0.13	0.13				
F	0.24	0.17	0.06	0.08	-0.78	0.54	0.28	-0.19	-1.00					
G	-0.24	-0.17	-0.06	-0.08	0.78	-0.54	-0.28	0.19						
H	0.10	0.78	-0.06	0.75	0.01	0.17	0.04							
I	0.00	0.10	0.07	0.08	-0.03	0.49								
J	0.18	0.39	0.07	0.34	-0.47									
K	-0.28	-0.06	-0.21	-0.02										
L	-0.14	0.94	-0.20											
M	0.67	-0.25												
N	-0.16													

Figure 5.15: Pearson's regression (R) done for each column of Figure 5.12, showing relevant correlations between the columns.

	O	N	M	L	K	J	I	H	G	F	E	D	C	B
A	0.201	0.501	0.363	0.542	0.007	0.074	0.012	0.087	0.000	0.000	0.081	0.187	0.055	0.085
B	0.027	0.388	0.003	0.392	0.021	0.096	0.001	0.024	0.029	0.029	0.760	0.673	0.806	
C	0.054	0.215	0.003	0.205	0.057	0.123	0.023	0.008	0.040	0.040	0.747	0.363		
D	0.009	0.612	0.003	0.568	0.000	0.029	0.002	0.024	0.010	0.010	0.681			
E	0.058	0.372	0.000	0.297	0.004	0.035	0.026	0.001	0.016	0.016				
F	0.057	0.030	0.004	0.006	0.616	0.291	0.080	0.037	1.000					
G	0.057	0.030	0.004	0.006	0.616	0.291	0.080	0.037						
H	0.009	0.612	0.003	0.568	0.000	0.029	0.002							
I	0.000	0.011	0.004	0.006	0.001	0.236								
J	0.034	0.154	0.005	0.114	0.225									
K	0.076	0.003	0.043	0.000										
L	0.020	0.884	0.040											
M	0.452	0.060												
N	0.024													

Figure 5.16: R^2 for each column of Figure 5.12.

standing to CBF data collected using ASL-fMRI. Much of the model comparison analysis done incorporating penalty terms for higher-order models consistently showed one thing: the tried and true model worked better than any additional elaborations added to the original model.

The results presented in this thesis has shown that the currently available methods are not only just good enough - they actual surpass newer proposed methods and models (at the very least for the current CBF dataset under investigation). The techniques that have been developed can be used to investigate other such datasets and could even be implemented as a prefilter for determining the eligibility of datasets to be modelled using higher-order models. The key finding, whether a model with more complex dynamics would better model CBF data over a standard GLM analysis, was determined to be a definite no.

Chapter 6

Conclusions and Future Work

Data collection in fMRI is a trade-off between signal accuracy, physiological accuracy, temporal resolution and spatial resolution. Attempts to increase any one of the four factors may sacrifice accuracy of the other three. Therefore analysis becomes a balancing act where all four factors are optimized so that the best decision can be made using the collected information. As was previously mentioned, the ultimate goal of fMRI is to be able to quantify neuronal activation correlates across the brain. This yearning has brought about a tremendous amount of research in signal analysis and measurement techniques, constructing equations and tools that attempt to make sense of the complex relationship between psychology and physiology.

The key to any measurement application is in being able to find a marker that can be correlated to the phenomenon to be measured. For fMRI research, the phenomenon is neuronal activity and the marker most commonly used is the BOLD-fMRI signal. However, the BOLD-fMRI signal is a downstream effect, produced through various changes in physiology (CBF, CBV and $CMRO_2$) that were first initiated through neuronal activation. Many groups have attempted to recover the 'true' neuronal activation through modelling of the behaviour of the BOLD-fMRI signal through upstream interactions of physiological changes in CBF, CBV and $CMRO_2$. Although the BOLD-fMRI signal is key to understanding brain activation, being a secondary effect of neuronal activation, it is still not considered an accurate indication of neuronal activation. There are two main branches of research in fMRI signal modelling, one inspired by Buxton et al. (1998) and the other by Davis et al. (1998). The two branches have dissected the problem in different ways.

The first branch of research focuses on providing deterministic modelling of components of the BOLD-fMRI signal. Buxton et al. (1998) proposed the currently best accepted hemodynamic model - the balloon model. The model has been presented in Chapter 2

and is a highly complex set of mathematical equations governing how BOLD-fMRI is produced from neuronal activation. Recent groups such as Bennett et al. (2008b) have expanded the Buxton et al. (1998) model to include more complexity resulting from biochemical and cell-to-cell interactions within the capillaries. It seems that there are a multitude of physiological precursors and effects resulting in the BOLD-fMRI signal and modelling of all such phenomena would result in a very complex model indeed.

The second branch of research focuses upon multi-modal aquisition for the better estimation of $CMRO_2$, which has traditionally been suggested as the best marker for neuronal activity. Researchers have searched for a more direct measurement of neuronal activation. This branch of research has been very active with expansions by Lu et al. (2003) to original Davis et al. (1998) paper to include CBV measurements in addition to CBF and BOLD signals so that $CMRO_2$ can be estimated with more accuracy. Physiologically grounded measurements such as ASL-fMRI for CBF and VASO-fMRI for CBV have recently attracted a lot of interest within the research community. Although not as fast as BOLD-fMRI, the two measurements and in particular ASL-fMRI have been used to 'calibrate' the BOLD-fMRI data so that indirect measurements of $CMRO_2$ can be found.

It is commonly accepted that the CBF response is one of the many causes of change in the measured BOLD-fMRI signal. Therefore, the ASL-fMRI signal, which measures CBF, can be considered to be closer in physiology to neuronal activation. As such, we have taken the view that a better indication for neuronal activity may be found by directly modelling the CBF response and as such, the work done cannot be directly classified as belonging to any of the two main branches of fMRI-signal research. However, it provides an additional perspective to an already vibrant field.

Findings of Simulated and Experimental CBF Data Novel analysis paradigms were developed and used for analysis of both simulated and experimental data. The framework was developed after noticing that the accurate signal estimation was highly dependent upon the sampling rate and the signal error. As such, the simulations focused upon creating visualizations of how estimation of various types of models became affected at different values of sampling frequency and signal error.

The analysis in Chapter 4 showed that transient features such as spiking (estimation of ϵ_1 and ϵ_4) requires at least 2 data points within the time period of the spike in order to accurately determine the feature. Ideally, a spike lasting 1.0 seconds would require a sampling time of 0.5 seconds to be robust enough for proper estimation with noise. Figure 3.1 shows transient features between 2.0 to 4.0 seconds. Effective modelling of

features require sampling time (or TR) to be at least 2.0 seconds or shorter and ideally less than 1.0 seconds in order to have an effective estimation of transients. The results were shown in Section 4.4. Estimation of coefficients governing transient dynamics was found to be not needed (Section 4.5). This was important as it simplified estimation from a nonlinear problem to that of a strictly linear problem. The models were simplified greatly so as arbitrary dynamic models were not needed to be included in estimation. Section 4.6 showed that at sufficiently long TRs (longer than 2.0 seconds), a first-order model was able to be used in place of all higher order models.

The analysis of experimental data in Chapter 5 extended upon the simulations in Chapter 4. The original twenty-eight models were shortlisted to twelve and each model was used for analysis of real CBF data. Further comparison of the models using both AIC and BIC showed that 0th-order dynamics without any ramping or spiking responses outperformed all models across all voxels within the brain as well as in all anatomical regions of the brain. Evidence that higher-order models were a more effective estimators of CBF data was not found within the experimental dataset.

Implications of Findings Although there were a combination of twenty-eight possible models constructed for analysis of the CBF signal, choosing the best performing model for a dataset becomes very important. The analysis of both simulated data (Chapter 4) and real CBF data (Chapter 5) provided surprising yet compelling evidence to suggest that the simplest model may in fact be the best performing model overall. This simple observation raises questions regarding the current approach to modelling BOLD-fMRI data, the most obvious being: how verifiable are the current models of neuronal activation?

The findings of this thesis suggests that work pioneered by Buxton et al. (2004); Friston et al. (2000) modelling the CBF response to first and second order differential equations may not be able to be seen in data measured using ASL-fMRI. A simple coupling relationship defined using a zero-order differential equation would be sufficient and even more accurate than using any model containing differential dynamics. Even if the sampling-time or TR was decreased from 6.0 seconds to 2.0 seconds (a 66% reduction), the zero-order system would still appear the best model for correlation with data. As such, it puts into question the effectiveness of using a biochemical model of neuronal activation to predict the BOLD-fMRI reponse as done by Bennett et al. (2008a,b). Even if the model was correct, it would not be possible to verify the model at this current stage of fMRI technology and using such a model for estimation would be highly impractical.

Furthermore, the result that signal estimation is very much affected by the temporal

resolution places a tighter restriction on the limits of multi-modal signal acquisition. As Kida et al. (2007) and Leontiev et al. (2007) have shown, indirect measurement of $CMRO_2$ is very much prone to error. It has been found in this thesis that small errors will severely impact estimation of signals at long temporal resolutions. The findings suggest that in order to improve upon measurement, temporal resolution and signal error are required to be in a delicate balance. The notion that 'the more signals acquired the better' must have an additional condition that accuracy does not suffer as a consequence of additional sequence acquisitions. Studies attempting to use the Lu et al. (2003) model should be aware of the limits demonstrated in this thesis concerning the relationship between temporal resolution, noise and model estimation accuracy.

Although being at risk of taking a defeatist stand on the issue of fMRI modelling, we believe that as signal acquisition methods improve, the models of fMRI signal change to hemodynamic responses will thus become verifiable and become a practical means of signal estimation. However, the implications of our simulations suggest that models may not benefit from the addition of more complex dynamics and researchers should avoid over-engineering a model without having the data to support it.

Future Work This thesis has shown that although higher-order models of CBF can be constructed, they may not offer any greater insight into ASL-fMRI data than a simple model and in fact, may be less accurate. It is a warning to researchers to recognize the limits of how the data can be interpreted as opposed to becoming attached to models that introduce greater complexities without them being in the data. The comparison framework used this thesis can provide a practical tool for researchers to quickly determine whether modelling their data using higher order equations is suitable based upon the sampling time as well as the included within the data. Although the tools were developed for CBF data, they can be easily modified for BOLD-fMRI data. Future work will consider the application of the framework to other experimental CBF datasets in order to expand the results contained in this thesis.

Bibliography

Akaike, H., 1974. A new look at the statistical model identification. Automatic Control, IEEE Transactions on 19 (6), 716–723.

Akaike, H., 1979. A Bayesian extension of the minimum AIC procedure of autoregressive model fitting. Biometrika.

Alsop, D. C., Detre, J. A., Nov 1996. Reduced transit-time sensitivity in noninvasive magnetic resonance imaging of human cerebral blood flow. J Cereb Blood Flow Metab 16 (6), 1236–49.

Ames, A., Nov 2000. CNS energy metabolism as related to function. Brain Res 34 (1-2), 42–68.

Ances, B. M., Leontiev, O., Perthen, J. E., Liang, C., Lansing, A. E., Buxton, R. B., Feb 2008. Regional differences in the coupling of cerebral blood flow and oxygen metabolism changes in response to activation: implications for BOLD-fMRI. NeuroImage 39 (4), 1510–21.

Ances, B. M., Liang, C. L., Leontiev, O., Perthen, J. E., Fleisher, A. S., Lansing, A. E., Buxton, R. B., Apr 2009. Effects of aging on cerebral blood flow, oxygen metabolism, and blood oxygenation level dependent responses to visual stimulation. Hum Brain Map 30 (4), 1120–32.

Attwell, D., Iadecola, C., Dec 2002. The neural basis of functional brain imaging signals. Trends Neurosci 25 (12), 621–5.

Attwell, D., Laughlin, S. B., Oct 2001. An energy budget for signaling in the grey matter of the brain. J Cereb Blood Flow Metab 21 (10), 1133–45.

Aubert, A., Costalat, R., Nov 2005. Interaction between astrocytes and neurons studied using a mathematical model of compartmentalized energy metabolism. Journal of cerebral blood flow and metabolism : official journal of the International Society of Cerebral Blood Flow and Metabolism 25 (11), 1476–90.

Aubert, A., Pellerin, L., Magistretti, P. J., Costalat, R., Mar 2007. A coherent neurobiological framework for functional neuroimaging provided by a model integrating compartmentalized energy metabolism. Proc Natl Acad Sci USA 104 (10), 4188–93.

Bandettini, P., Feb 2007. Functional MRI today. Int J Psychophysiology 63 (2), 138–45.

Baron, J. C., Rougemont, D., Soussaline, F., Bustany, P., Crouzel, C., Bousser, M. G., Comar, D., Jun 1984. Local interrelationships of cerebral oxygen consumption and glucose utilization in normal subjects and in ischemic stroke patients: a positron tomography study. J Cereb Blood Flow Metab 4 (2), 140–9.

Bennett, M. R., Farnell, L., Gibson, W. G., Jan 2008a. Origins of blood volume change due to glutamatergic synaptic activity at astrocytes abutting on arteriolar smooth muscle cells. J Theor Biol 250 (1), 172–85.

Bennett, M. R., Farnell, L., Gibson, W. G., May 2008b. Origins of the BOLD changes due to synaptic activity at astrocytes abutting arteriolar smooth muscle. J Theor Biol 252 (1), 123–30.

Bloch, F., Hansen, W., Packard, M., Jan 1946. Nuclear induction. Phys Rev 70 (7-8), 460–474.

Boxerman, J. L., Hamberg, L. M., Rosen, B. R., Weisskoff, R. M., Oct 1995. MR contrast due to intravascular magnetic susceptibility perturbations. Magn Reson Med 34 (4), 555–66.

Brooks, R. A., Chiro, G. D., Jan 1987. Magnetic resonance imaging of stationary blood: a review. Med Physics 14 (6), 903–13.

Buxton, R. B., Uludağ, K., Dubowitz, D. J., Liu, T. T., Jan 2004. Modeling the hemodynamic response to brain activation. NeuroImage 23, S220–233.

Buxton, R. B., Wong, E. C., Frank, L. R., Jun 1998. Dynamics of blood flow and oxygenation changes during brain activation: the balloon model. Magn Reson Med 39 (6), 855–64.

Caesar, K., Thomsen, K., Lauritzen, M., Dec 2003. Dissociation of spikes, synaptic activity, and activity-dependent increments in rat cerebellar blood flow by tonic synaptic inhibition. Proc Natl Acad Sci USA 100 (26), 16000–5.

Casanova, R., Ryali, S., Serences, J., Yang, L., Kraft, R., Laurienti, P. J., Maldjian, J. A., May 2008. The impact of temporal regularization on estimates of the bold hemodynamic response function: a comparative analysis. Neuroimage 40 (4), 1606–18.

Chen-Bee, C. H., Agoncillo, T., Xiong, Y., Frostig, R. D., Apr 2007. The triphasic intrinsic signal: implications for functional imaging. J Neurosci 27 (17), 4572–86.

Chiarelli, P. A., Bulte, D. P., Piechnik, S., Jezzard, P., Jan 2007. Sources of systematic bias in hypercapnia-calibrated functional MRI estimation of oxygen metabolism. NeuroImage 34 (1), 35–43.

Christmann, C., Koeppe, C., Braus, D. F., Ruf, M., Flor, H., Feb 2007. A simultaneous EEG-fMRI study of painful electric stimulation. NeuroImage 34 (4), 1428–37.

Davis, T. L., Kwong, K. K., Weisskoff, R. M., Rosen, B. R., Feb 1998. Calibrated functional MRI: mapping the dynamics of oxidative metabolism. Proc Natl Acad Sci USA 95 (4), 1834–9.

Deneux, T., Faugeras, O., Oct 2006. Using nonlinear models in fMRI data analysis: model selection and activation detection. NeuroImage 32 (4), 1669–89.

Detre, J. A., Leigh, J. S., Williams, D. S., Koretsky, A. P., Jan 1992. Perfusion imaging. Magn Reson Med 23 (1), 37–45.

Diekhoff, S., Uludağ, K., Sparing, R., 2011. Functional localization in the human brain: GradientâĂŘecho, spinâĂŘecho, and arterial spinâĂŘlabeling fMRI compared with neuronavigated TMS. Human brain ....

Dixon, W. T., Du, L. N., Faul, D. D., Gado, M., Rossnick, S., Jun 1986. Projection angiograms of blood labeled by adiabatic fast passage. Magn Reson Med 3 (3), 454–62.

Duff, E., Xiong, J., Wang, B., Cunnington, R., Fox, P., Egan, G., Jan 2007. Complex spatio-temporal dynamics of fMRI BOLD: A study of motor learning. NeuroImage 34 (1), 156–68.

Duong, T. Q., Yacoub, E., Adriany, G., Hu, X., Ugurbil, K., Kim, S.-G., Jun 2003. Microvascular BOLD contribution at 4 and 7 T in the human brain: gradient-echo and spin-echo fMRI with suppression of blood effects. Magn Reson Med 49 (6), 1019–27.

Erecińska, M., Silver, I. A., Feb 1989. ATP and brain function. J Cereb Blood Flow Metab 9 (1), 2–19.

Ernst, T., Hennig, J., Jul 1994. Observation of a fast response in functional mr. Magn Reson Med 32 (1), 146–9.

Fox, P. T., Raichle, M. E., Feb 1986. Focal physiological uncoupling of cerebral blood flow and oxidative metabolism during somatosensory stimulation in human subjects. Proc Natl Acad Sci USA 83 (4), 1140–4.

Fox, P. T., Raichle, M. E., Mintun, M. A., Dence, C., Jul 1988. Nonoxidative glucose consumption during focal physiologic neural activity. Science 241 (4864), 462–4.

Friston, K., Holmes, A., Worsley, K., Poline, J., Jan 1994. Statistical parametric maps in functional imaging: a general linear approach. Hum Brain Map 2 (4), 189.

Friston, K. J., Josephs, O., Rees, G., Turner, R., Jan 1998. Nonlinear event-related responses in fMRI. Magn Reson Med 39 (1), 41–52.

Friston, K. J., Mechelli, A., Turner, R., Price, C. J., Oct 2000. Nonlinear responses in fMRI: the Balloon model, Volterra kernels, and other hemodynamics. NeuroImage 12 (4), 466–77.

Fujita, N., Oct 2001. Extravascular contribution of blood oxygenation level-dependent signal changes: a numerical analysis based on a vascular network model. Magn Reson Med 46 (4), 723–34.

Glover, G. H., Apr 1999. Deconvolution of impulse response in event-related BOLD fMRI. NeuroImage 9 (4), 416–29.

Goense, J. B. M., Logothetis, N. K., May 2008. Neurophysiology of the BOLD fMRI signal in awake monkeys. Curr Biol 18 (9), 631–40.

Grubb, R. L., Raichle, M. E., Eichling, J. O., Ter-Pogossian, M. M., Jan 1974. The effects of changes in PaCO2 on cerebral blood volume, blood flow, and vascular mean transit time. Stroke 5 (5), 630–9.

Harms, M. P., Melcher, J. R., Nov 2003. Detection and quantification of a wide range of fMRI temporal responses using a physiologically-motivated basis set. Hum Brain Map 20 (3), 168–83.

Hoge, R. D., Atkinson, J., Gill, B., Crelier, G. R., Marrett, S., Pike, G. B., Nov 1999a. Investigation of BOLD signal dependence on cerebral blood flow and oxygen consumption: the deoxyhemoglobin dilution model. Magn Reson Med 42 (5), 849–63.

Hoge, R. D., Atkinson, J., Gill, B., Crelier, G. R., Marrett, S., Pike, G. B., Aug 1999b. Linear coupling between cerebral blood flow and oxygen consumption in activated human cortex. Proc Natl Acad Sci USA 96 (16), 9403–8.

Huettel, S. A., McCarthy, G., Nov 2001. Regional differences in the refractory period of the hemodynamic response: an event-related fmri study. Neuroimage 14 (5), 967–76.

Jahng, G.-H., Weiner, M. W., Schuff, N., Nov 2007. Improved arterial spin labeling method: applications for measurements of cerebral blood flow in human brain at high magnetic field MRI. Med Physics 34 (11), 4519–25.

Johnston, L. A., Duff, E., Mareels, I., Egan, G. F., Apr 2008. Nonlinear estimation of the BOLD signal. NeuroImage 40 (2), 504–14.

Jolivet, R., Allaman, I., Pellerin, L., Magistretti, P. J., Weber, B., Aug 2010. Comment on recent modeling studies of astrocyte-neuron metabolic interactions. Journal of cerebral blood flow and metabolism : official journal of the International Society of Cerebral Blood Flow and Metabolism.

Jones, M., Berwick, J., Johnston, D., Mayhew, J., Jun 2001. Concurrent optical imaging spectroscopy and laser-doppler flowmetry: the relationship between blood flow, oxygenation, and volume in rodent barrel cortex. NeuroImage 13 (6 Pt 1), 1002–15.

Kastrup, A., Krüger, G., Neumann-Haefelin, T., Glover, G. H., Moseley, M. E., Jan 2002. Changes of cerebral blood flow, oxygenation, and oxidative metabolism during graded motor activation. NeuroImage 15 (1), 74–82.

Kennerley, A. J., Berwick, J., Martindale, J., Johnston, D., Papadakis, N., Mayhew, J. E., Aug 2005. Concurrent fmri and optical measures for the investigation of the hemodynamic response function. Magnetic resonance in medicine : official journal of the Society of Magnetic Resonance in Medicine / Society of Magnetic Resonance in Medicine 54 (2), 354–65.

Kida, I., Rothman, D. L., Hyder, F., Apr 2007. Dynamics of changes in blood flow, volume, and oxygenation: implications for dynamic functional magnetic resonance imaging calibration. J Cereb Blood Flow Metab 27 (4), 690–6.

Kraus, R. H., Volegov, P., Matlachov, A., Espy, M., Jan 2008. Toward direct neural current imaging by resonant mechanisms at ultra-low field. NeuroImage 39 (1), 310–7.

Kuwabara, H., Ohta, S., Brust, P., Meyer, E., Gjedde, A., Jan 1992. Density of perfused capillaries in living human brain during functional activation. Prog Brain Res 91, 209–15.

Larmor, J., 1896. The influence of a magnetic field on radiation frequency. Proceedings of the Royal Society of London 60, 513–515.

Lauterbur, P., Jan 1973. Image formation by induced local interactions: examples employing nuclear magnetic resonance. Nature.

Leontiev, O., Buxton, R. B., Mar 2007. Reproducibility of BOLD, perfusion, and CMRO2 measurements with calibrated-BOLD fMRI. NeuroImage 35 (1), 175–84.

Leontiev, O., Dubowitz, D. J., Buxton, R. B., Jul 2007. CBF/CMRO2 coupling measured with calibrated BOLD fMRI: sources of bias. NeuroImage 36 (4), 1110–22.

Li, D., Wang, Y., Waight, D. J., May 1998. Blood oxygen saturation assessment in vivo using T2* estimation. Magn Reson Med 39 (5), 685–90.

Liau, J., Liu, T. T., Apr 2009. Inter-subject variability in hypercapnic normalization of the BOLD fMRI response. NeuroImage 45 (2), 420–30.

Lin, A.-L., Fox, P. T., Yang, Y., Lu, H., Tan, L.-H., Gao, J.-H., Aug 2008. Evaluation of MRI models in the measurement of CMRO2 and its relationship with CBF. Magn Reson Med 60 (2), 380–9.

Logothetis, N. K., Aug 2002. The neural basis of the blood-oxygen-level-dependent functional magnetic resonance imaging signal. Philos Trans R Soc Lond, B, Biol Sci 357 (1424), 1003–37.

Logothetis, N. K., May 2003. The underpinnings of the BOLD functional magnetic resonance imaging signal. J Neurosci 23 (10), 3963–71.

Logothetis, N. K., Jun 2008. What we can do and what we cannot do with fMRI. Nature 453 (7197), 869–78.

Logothetis, N. K., Pauls, J., Augath, M., Trinath, T., Oeltermann, A., Jul 2001. Neurophysiological investigation of the basis of the fMRI signal. Nature 412 (6843), 150–7.

Lu, H., Golay, X., Pekar, J. J., Zijl, P. C. M. V., Aug 2003. Functional magnetic resonance imaging based on changes in vascular space occupancy. Magn Reson Med 50 (2), 263–74.

Lu, H., Golay, X., Pekar, J. J., Zijl, P. C. M. V., Jul 2004. Sustained poststimulus elevation in cerebral oxygen utilization after vascular recovery. J Cereb Blood Flow Metab 24 (7), 764–70.

Luo, F., Schmidt, K. F., Fox, G. B., Ferris, C. F., Aug 2009. Differential responses in CBF and CBV to cocaine as measured by fMRI: implications for pharmacological MRI signals derived oxygen metabolism assessment. J Psychia Res 43 (12), 1018–24.

Malonek, D., Grinvald, A., Apr 1996. Interactions between electrical activity and cortical microcirculation revealed by imaging spectroscopy: implications for functional brain mapping. Science 272 (5261), 551–4.

Mandeville, J. B., Marota, J. J., Ayata, C., Zaharchuk, G., Moskowitz, M. A., Rosen, B. R., Weisskoff, R. M., Jun 1999. Evidence of a cerebrovascular postarteriole windkessel with delayed compliance. J Cereb Blood Flow Metab 19 (6), 679–89.

Marrett, S., Gjedde, A., Jan 1997. Changes of blood flow and oxygen consumption in visual cortex of living humans. Adv Exp Med Biol 413, 205–8.

Miller, K. L., Luh, W. M., Liu, T. T., Martinez, A., Obata, T., Wong, E. C., Frank, L. R., Buxton, R. B., May 2001. Nonlinear temporal dynamics of the cerebral blood flow response. Hum Brain Map 13 (1), 1–12.

Mosso, A., 1884. La Paura. Milan.

Obata, T., Liu, T. T., Miller, K. L., Luh, W. M., Wong, E. C., Frank, L. R., Buxton, R. B., Jan 2004. Discrepancies between BOLD and flow dynamics in primary and supplementary motor areas: application of the balloon model to the interpretation of BOLD transients. NeuroImage 21 (1), 144–53.

Oeltermann, A., Augath, M. A., Logothetis, N. K., Jul 2007. Simultaneous recording of neuronal signals and functional NMR imaging. Magn Reson Img 25 (6), 760–74.

Offenhauser, N., Thomsen, K., Caesar, K., Lauritzen, M., May 2005. Activity-induced tissue oxygenation changes in rat cerebellar cortex: interplay of postsynaptic activation and blood flow. J Physiol 565 (Pt 1), 279–94.

Ogawa, S., Lee, T., Kay, A., Tank, D., Jan 1990. Brain magnetic resonance imaging with contrast dependent on blood oxygenation. Proc Natl Acad Sci USA 87 (24), 9868–9872.

Ogawa, S., Lee, T. M., Oct 1990. Magnetic resonance imaging of blood vessels at high fields: in vivo and in vitro measurements and image simulation. Magn Reson Med 16 (1), 9–18.

Ogawa, S., Menon, R. S., Tank, D. W., Kim, S. G., Merkle, H., Ellermann, J. M., Ugurbil, K., Mar 1993. Functional brain mapping by blood oxygenation level-dependent contrast magnetic resonance imaging. A comparison of signal characteristics with a biophysical model. BioPhy J 64 (3), 803–12.

Pauling, L., Coryell, C. D., Apr 1936. The Magnetic Properties and Structure of Hemoglobin, Oxyhemoglobin and Carbonmonoxyhemoglobin. Proc Natl Acad Sci USA 22 (4), 210–6.

Pellerin, L., Bouzier-Sore, A.-K., Aubert, A., Serres, S., Merle, M., Costalat, R., Magistretti, P. J., Sep 2007. Activity-dependent regulation of energy metabolism by astrocytes: an update. Glia 55 (12), 1251–62.

Perthen, J. E., Lansing, A. E., Liau, J., Liu, T. T., Buxton, R. B., Mar 2008. Caffeine-induced uncoupling of cerebral blood flow and oxygen metabolism: a calibrated BOLD fMRI study. NeuroImage 40 (1), 237–47.

Phelps, M. E., Hoffman, E. J., Mullani, N. A., Ter-Pogossian, M. M., Mar 1975. Application of annihilation coincidence detection to transaxial reconstruction tomography. J Nucl Med 16 (3), 210–24.

Purcell, E., Torrey, H., Pound, R., Jan 1946. Resonance absorption by nuclear magnetic moments in a solid. Physical Review 69 (1), 37.

Raichle, M. E., Feb 1998. Behind the scenes of functional brain imaging: a historical and physiological perspective. Proc Natl Acad Sci USA 95 (3), 765–72.

Raichle, M. E., Grubb, R. L., Gado, M. H., Eichling, J. O., Ter-Pogossian, M. M., Aug 1976. Correlation between regional cerebral blood flow and oxidative metabolism. In vivo studies in man. Arch Neurol 33 (8), 523–6.

Raichle, M. E., Mintun, M. A., Jan 2006. Brain work and brain imaging. Annu Rev Neurosci 29, 449–76.

Rauch, A., Rainer, G., Augath, M., Oeltermann, A., Logothetis, N. K., Apr 2008a. Pharmacological MRI combined with electrophysiology in non-human primates: effects of Lidocaine on primary visual cortex. NeuroImage 40 (2), 590–600.

Rauch, A., Rainer, G., Logothetis, N. K., May 2008b. The effect of a serotonin-induced dissociation between spiking and perisynaptic activity on BOLD functional MRI. Proc Natl Acad Sci USA 105 (18), 6759–64.

Riera, J. J., Wan, X., Jimenez, J. C., Kawashima, R., Nov 2006. Nonlinear local electrovascular coupling. i: A theoretical model. Hum Brain Mapp 27 (11), 896–914.

Riera, J. J., Watanabe, J., Kazuki, I., Naoki, M., Aubert, E., Ozaki, T., Kawashima, R., Feb 2004. A state-space model of the hemodynamic approach: nonlinear filtering of BOLD signals. NeuroImage 21 (2), 547–67.

Roland, P. E., Eriksson, L., Stone-Elander, S., Widen, L., Aug 1987. Does mental activity change the oxidative metabolism of the brain? J Neurosci 7 (8), 2373–89.

Roy, C. S., Sherrington, C. S., Jan 1890. On the Regulation of the Blood-supply of the Brain. J Physiol 11 (1-2), 85–158.17.

S Vulliemoz, R Thornton, R. R. D. W. C. M. G. S. L. A. W. M. L. S. C. M. M. J. S. D., Lemieux, L., Jul 2009. The spatio-temporal mapping of epileptic networks: combination of eeg-fmri and eeg source imaging. Neuroimage 46 (3), 834–843.

Shmuel, A., Yacoub, E., Pfeuffer, J., de Moortele, P. F. V., Adriany, G., Hu, X., Ugurbil, K., Dec 2002. Sustained negative BOLD, blood flow and oxygen consumption response and its coupling to the positive response in the human brain. Neuron 36 (6), 1195–210.

Siesjö, B. K., Jan 1978. Brain energy metabolismâĂŐ, 607.

Simpson, I. A., Carruthers, A., Vannucci, S. J., Nov 2007. Supply and demand in cerebral energy metabolism: the role of nutrient transporters. Journal of cerebral blood flow and metabolism : official journal of the International Society of Cerebral Blood Flow and Metabolism 27 (11), 1766–91.

Stefanovic, B., Pike, G. B., Feb 2005. Venous refocusing for volume estimation: VERVE functional magnetic resonance imaging. Magn Reson Med 53 (2), 339–47.

Stefanovic, B., Warnking, J. M., Pike, G. B., Jun 2004. Hemodynamic and metabolic responses to neuronal inhibition. NeuroImage 22 (2), 771–8.

Ter-Pogossian, M. M., Phelps, M. E., Hoffman, E. J., Mullani, N. A., Jan 1975. A positron-emission transaxial tomograph for nuclear imaging (pett). Radiology 114 (1), 89–98.

Toga, A. W., Mazziotta, J. C., Jan 2002. Brain mapping: the methodsâĂŐ, 877.

Uludağ, K., Dubowitz, D. J., Yoder, E. J., Restom, K., Liu, T. T., Buxton, R. B., Sep 2004. Coupling of cerebral blood flow and oxygen consumption during physiological activation and deactivation measured with fMRI. NeuroImage 23 (1), 148–55.

Vakorin, V. A., Krakovska, O. O., Borowsky, R., Sarty, G. E., Nov 2007. Inferring neural activity from bold signals through nonlinear optimization. Neuroimage 38 (2), 248–60.

Vazquez, A. L., Noll, D. C., Feb 1998. Nonlinear aspects of the BOLD response in functional MRI. NeuroImage 7 (2), 108–18.

Vulliemoz, S., Thornton, R., Rodionov, R., Carmichael, D. W., Guye, M., Lhatoo, S., McEvoy, A. W., Spinelli, L., Michel, C. M., Duncan, J. S., Lemieux, L., Jul 2009. The spatio-temporal mapping of epileptic networks: combination of EEG-fMRI and EEG source imaging. NeuroImage 46 (3), 834–43.

Wang, J., Alsop, D. C., Li, L., Listerud, J., Gonzalez-At, J. B., Schnall, M. D., Detre, J. A., Aug 2002. Comparison of quantitative perfusion imaging using arterial spin labeling at 1.5 and 4.0 tesla. Magnetic resonance in medicine : official journal of the Society of Magnetic Resonance in Medicine / Society of Magnetic Resonance in Medicine 48 (2), 242–54.

Williams, D. S., Detre, J. A., Leigh, J. S., Koretsky, A. P., Jan 1992. Magnetic resonance imaging of perfusion using spin inversion of arterial water. Proc Natl Acad Sci USA 89 (1), 212–6.

Wong, E. C., Buxton, R. B., Frank, L. R., Jan 1997. Implementation of quantitative perfusion imaging techniques for functional brain mapping using pulsed arterial spin labeling. NMR in Biomedicine 10 (4-5), 237–49.

Yablonskiy, D. A., Haacke, E. M., Dec 1994. Theory of NMR signal behavior in magnetically inhomogeneous tissues: the static dephasing regime. Magn Reson Med 32 (6), 749–63.

Yacoub, E., Shmuel, A., Pfeuffer, J., Moortele, P. F. V. D., Adriany, G., Ugurbil, K., Hu, X., Jan 2001. Investigation of the initial dip in fMRI at 7 Tesla. NMR in Biomedicine 14 (7-8), 408–12.

Yang, S. P., Bergö, G. W., Krasney, E., Krasney, J. A., Jan 1994. Cerebral pressure-flow and metabolic responses to sustained hypoxia: effect of CO2. J Appl Physiol 76 (1), 303–13.

Yarowsky, P. J., Ingvar, D. H., Jul 1981. Symposium summary. Neuronal activity and energy metabolism. Fed Proc 40 (9), 2353–62.

Yeşilyurt, B., Uğurbil, K., Uludağ, K., Sep 2008. Dynamics and nonlinearities of the BOLD response at very short stimulus durations. Magn Reson Img 26 (7), 853–62.

Zheng, Y., Johnston, D., Berwick, J., Chen, D., ..., S. B., Jan 2005. A three-compartment model of the hemodynamic response and oxygen delivery to brain. NeuroImage.

Zheng, Y., Martindale, J., Johnston, D., Jones, M., Berwick, J., Mayhew, J., Jul 2002. A model of the hemodynamic response and oxygen delivery to brain. NeuroImage 16 (3 Pt 1), 617–37.

Zheng, Y., Mayhew, J., Oct 2009. A time-invariant visco-elastic windkessel model relating blood flow and blood volume. NeuroImage 47 (4), 1371–80.

Zheng, Y., Pan, Y., Harris, S., Billings, S., Coca, D., Berwick, J., Jones, M., Kennerley, A., Johnston, D., Martin, C., Devonshire, I. M., Mayhew, J., Sep 2010. A dynamic model of neurovascular coupling: implications for blood vessel dilation and constriction. NeuroImage 52 (3), 1135–47.